Ignition Delay of Non-Premixed Methane-Air Mixtures using Conditional Moment Closure (CMC)

by

Ahmad El Sayed

A thesis
presented to the University of Waterloo
in fulfillment of the
thesis requirement for the degree of
Master of Applied Science
in
Mechanical Engineering

Waterloo, Ontario, Canada, 2007

I hereby declare that I am the sole author of this thesis. This is a true copy of the thesis, including any required final revisions, as accepted by my examiners.

I understand that my thesis may be made electronically available to the public.

Ahmad El Sayed

Abstract

Autoignition of non-premixed methane-air mixtures is investigated using first-order Conditional Moment closure (CMC). In CMC, scalar quantities are conditionally averaged with respect to a conserved scalar, usually the mixture fraction [8]. The conditional fluctuations are often of small order, allowing the chemical source term to be modeled as a function of the conditional species concentrations and the conditional enthalpy (temperature). The first-order CMC derivation leaves many terms unclosed such as the conditional scalar dissipation rate, velocity and turbulent fluxes, and the probability density function. Submodels for these quantities are discussed and validated against Direct Numerical Simulations (DNS). The CMC and the turbulent velocity and mixing fields calculations are decoupled based on the frozen mixing assumption, and the CMC equations are cross-stream averaged across the flow following the shear flow approximation [63]. Finite differences are used to discretize the equations, and a two-step fractional method is implemented to treat separately the stiff chemical source term. The stiff ODE solver LSODE [45] is used to solve the resulting system of equations. The recently developed detailed chemical kinetics mechanism UBC-Mech 1.0 [49] is employed throughout this study, and preexisting mechanisms are visited. Several ignition criteria are also investigated. Homogeneous and inhomogeneous CMC calculations are performed in order to investigate the role of physical transport in autoignition. Furthermore, the results of the perfectly homogeneous reactor calculations are presented and the critical value of the scalar dissipation rate for ignition is determined. The results are compared to the shock tube experimental data of Sullivan et al. [113].

The current results show good agreement with the experiments in terms of both ignition delay and ignition kernel location, and the trends obtained in the experiments are successfully reproduced. The results were shown to be sensitive to the scalar dissipation model, the chemical kinetics, and the ignition criterion.

Acknowledgements

I would like to thank my supervisor Professor Cécile Devaud for her guidance and support. The knowledge I have gained over the last two years in the field of turbulent combustion and its numerical modeling is attributed to her.

I would also like to extend my thanks to Professor Alan Plumtree for his encouragement, and to Professor Roydon Fraser and Professor George Davidson for reviewing this thesis.

The financial support of AUTO 21 (Project NO. D203-DLB) and the University of Waterloo is gratefully acknowledged. This work would not have been possible without their funding.

Special thanks go to my friends and colleagues Samer Abdallah, Willian Chung, Pedram Hassanzade, Azad Qazi Zade, and Nada Zamel.

I would also like to thank my friend Lori Janbazian for the unforgettable time in Montreal.

I must also thank Dr. Claude Cizravi for his support and encouragement. His unique character was a source of inspiration.

Finally, I would like express my deepest thanks to my mother Rihab and to my sisters Rola and Nina for their love, care and support. This thesis is dedicated to them.

To my mother

"A mon passé qu'il soit vivant: J'aime qu'à tout moment, en tout lieu, occuper mon temps afin de ne pas revivre le passé. Mais les larmes s'entêtent et coulent... sucrées, elles sont parfois... amères, elles le sont aussi..."

R.E.

Contents

List of Tables

List of Figures

Nomenclature

List of Symbols

Latin

A_0	Frequency factor
b	Reaction exponent
c_p	Specific heat at constant pressure
D	Molecular diffusivity
D_t	Turbulent diffusivity
E_a	Activation energy
h	Specific enthalpy
J	Molecular diffusive flux
k	Turbulent kinetic energy, specific reaction rate
l	Turbulence length scale
m	Mass
N_η	Number of grid points in mixture fraction space
N_x	Number of grid points in physical space
N_s	Number of species in the mixture
p	Pressure

P	Probability density function
q	Rate of progress of a reaction
$\dot{q}$	Radiation source term
Q_α	Conditional concentration of species α
Q_h	Conditional enthalpy
Q_T	Conditional temperature
r	Radial coordinate
R_u	Universal gas constant
t	Time
T	Temperature
T_a	Activation temperature
u_i	Velocity in the i^{th} direction
u_x	Axial velocity component
W	Molecular weight
x	Axial Cartezian coordinate
x_i	Cartezian coordinate in the i^{th} direction
Y	Mass fraction
Z	Penetration length

Greek

α	A species in the mixture
β	Mixture fraction coupling function
Δt	Time step
Δx	Grid spacing
ε	Turbulence eddy dissipation

Γ	Gamma function
δ	Kronecker's delta
η	Sample variable of the mixture fraction
λ	Thermal conductivity
μ	Dynamic viscosity
μ_t	Turbulent viscosity
ν	Kinematic viscosity, stoichiometric coefficient
ρ	Density
τ_{ij}	Shear stress
τ_c	Chemical time scale
τ_t	Turbulent time scale
ξ	Mixture fraction
χ	Scalar dissipation rate
ψ	A conserved scalar
$\dot{\omega}$	Chemical source term

Dimensionless Numbers

Da	τ_t/τ_c	Damköhler number
Le	$\mathrm{Sc}/\mathrm{Pr} = \lambda/(\rho c_p D)$	Lewis Number
Pr	$\mu c_p/\lambda$	Prandtl Number
Sc	$\mu/(\rho D)$	Schmidt Number
Re	$\rho U L/\mu$	Reynolds Number

Superscripts

ϕ'	Unconditional fluctuation of ϕ

ϕ''	Conditional fluctuation of ϕ
$\bar{\phi}$	Reynolds average of ϕ
$\tilde{\phi}$	Favre average of ϕ
$\widetilde{\phi''^2}$	Favre variance of ϕ

Subscripts

1	Value in the oxidant stream
2	Value in the fuel stream
f	fuel
ign	Ignition
t	Turbulent

Miscellaneous

$\langle F \rangle$	Unconditional average of F
$\langle F \vert \eta \rangle$	Conditional average of F with respect to η
$\{F\}_R$	Area-weighted average of F
$\{F\}_{R^+}$	Cross-stream average of F

Acronyms

AMC	Amplitude Mapping Closure
CFD	Computational Fluid Dynamics
DNS	Direct Numerical Simulations
EBU	Eddy Break-Up
EDM	Eddy Dissipation Model
DCMC	Doubly-Conditioned Moment Closure

CMC	Conditional Moment Closure
CSE	Conditional Source Estimation with Laminar Flamelet Decomposition
ILDM	Intrinsic Low-Dimensional Manifolds
LEM	Linear Eddy Model
LES	Large Eddy Simulation
LFD	Laminar Flamelet Decomposition
LHS	Left Hand Side
ODE	Ordinary Differential Equation
PDE	Partial Differential Equation
PDF	Probability Density Function
RHS	Right Hand Side
RSM	Reynolds Stress Models
TGLDM	Trajectory Generated Low-Dimensional Manifold

Chapter 1

Introduction

1.1 Overview

Over the past few years methane has been seen as a good alternative fuel for direct-injection compression-ignition engines. This is mainly due to two reasons:

1. lower emissions compared to traditional fuels such as octane and diesel, which meets the recent environmental regulations and,

2. its abundance and availability world-wide.

In order to maintain high engine efficiency, the characteristics of autoignition need to be investigated and its mechanism needs to be well understood. However, due to the difficulties and high costs associated with the experimental measurements of a reacting mixture inside an running engine, it is crucial to develop reliable chemical kinetics mechanisms and turbulent combustion models that are able to accurately predict autoignition in conditions relevant to engine operation. This opens the door to new challenges: the degree of detail of the chemical kinetics, and the accuracy and complexity of the model. The two combined determine the efficiency of the calculations and the reliability of the predictions. Extensive research has been conducted in both areas and tremendous improvements have been made so far. Computationally, autoignition of non-premixed transient fuel jets in direct-injection systems remains a complicated problem due to the unsteady and turbulent nature of the

ignition phenomenon, and due to the stiff and non-linear chemical kinetics involved in the oxidization of the fuel. Thus, many simplifications are required while simulating practical engineering applications. Another difficulty encountered in ignition problems is the lack of a universal ignition criterion that is well correlated with experimental observations.

1.2 Objectives

In this study, auto-ignition of non-premixed methane-air mixtures is investigated using first-order Conditional Moment closure (CMC). For this purpose, a recently developed detailed chemical kinetics mechanism suitable for the prediction of ignition delay of high-pressure methane-air mixtures for air temperatures below 1400 K is used. Such conditions are relevant for engine applications. However, they have not been extensively investigated by many researchers. This study is motivated by the fact that the mechanism described above has never been used with CMC before. Other important aspects to explore are the effect of physical transport on autoignition in terms of both ignition delay and ignition kernel location, the sensitivity of CMC to micro-mixing models, and the ignition limit.

1.3 Outline

Chapter 2 presents the governing balance equations and the different averaging techniques used in turbulence modeling. A review of turbulence models and their applicability to reactive flows is given. The statistical properties of turbulent reacting flows, the non-linearity of the chemical source term, and the turbulence-chemistry interactions are also discussed. Finally, the commonly used non-premixed turbulent combustion models are reviewed.

The CMC model is explained in Chapter 3. The conditional species and temperature transport equations equations are derived using the decomposition approach. The primary closure hypothesis is discussed, and submodels for the unclosed terms in the CMC equations are presented and validated against direct numerical simulations and experiments.

Chapter 4 describes the shock tube autoignition experiments of non-premixed methane-air mixtures. The geometry of the facility is described and the experimental conditions

are provided. The frozen mixing assumption is introduced, and decoupling between the turbulent flow field calculations and CMC is explained. This chapter also discusses the adjustments made to the k-ε turbulence model and concludes with a quantitative and qualitative description of the simulation results.

The numerical solution of the CMC equations is presented in Chapter 5. The cross-stream averaging and the enthalpy-mixture fraction linear coupling techniques are explained. Numerical details such as the fractional step method, the discretization schemes, and the initial and boundary conditions are provided in detail. Also included are the description and mode of operation of the packages used in the simulations (a gas phase chemical kinetics package, a stiff ordinary differential equation solver, and an adaptive integrator). Finally, the chemical kinetics mechanism used in this study is described, in addition to a brief overview on other mechanisms.

Chapter 6 presents the results of this study. First, grid and time step sensitivity analyses are conducted. Homogeneous and inhomogeneous CMC calculations are then performed using different mixing models. In the inhomogeneous case, various chemical kinetics mechanisms and ignition criteria are tested, and the balance (budget) in the CMC equations is analyzed. Ignition limit calculations and perfectly homogeneous reactor calculations are also performed. The results are compared to experiments and other numerical simulations.

Finally, a summary is given in Chapter 7. Further developments are proposed.

Chapter 2

Background

Prior to the discussion of the CMC method, it is essential to present the tools used throughout this study, and to review some of the computational methods available in the literature. First, the conservation equations that govern the flow field are described. Then, the differences between Reynolds and Favre averaging techniques are explained, and the Favre-averaged conservation equations are provided. The most widely used turbulence models are also reviewed and briefly discussed. The statistical properties of turbulent reacting flows are then presented and the concept of the probability density function is introduced. Issues related to the non-linearity of the chemical source term and turbulence-chemistry interactions are addressed. The non-premixed turbulent combustion mode is emphasized in this chapter. The flame structure and characteristics of this combustion mode are described, and the usage of the mixture fraction variable and its variance are discussed. Finally, common turbulent combustion models from the literature are reviewed.

2.1 Overview

Autoignition, sometimes called self-ignition or spontaneous ignition, can be defined as the process in which a fuel-oxidizer mixture reacts in a self-heating fashion, leading to the ignition of the mixture. The autoignition mechanism involves a series of chain reactions and a large number of species that emerge during the oxidization of the fuel. From a thermodynamic point of view, the mixture ignites when the rate of thermal energy release is

greater than the rate of thermal energy dissipation [40], i.e. when a sufficient degree of self-heating is reached. This is achieved via the complicated and strongly coupled interactions between chemistry and turbulence, which manifest through exothermic chemical reactions, turbulent mixing and turbulent transport. However, distinction should be made between chemical and turbulent time scales, as they play a determistic role in the description of the chemistry-turbulence interactions. This issue is discussed in Section 2.5.3. Autoignition is accompanied by a sudden pressure increase and an abrupt heat release (temperature increase), and followed by the development of a flame. Physically, autoignition can be described in terms of two quantities: the location of the ignition kernel and ignition delay. The location of the ignition kernel is simply the location in the mixture where ignition occurs. On the other hand, ignition delay in injection stystems is defined as the period of time between the start of injection of the fuel and the appearance of the first ignition kernel [117]. Two autoignition regimes can be distinguished:

1. premixed when the fuel and the oxidizer are initially mixed. The mixing process should take place at sufficiently low temperatures in order to inhibit the chain-branching reactions that are responsible for the oxidization of the fuel, and consequently, achieve an non-reactive homogeneous mixture [40, 89], and

2. non-premixed when the fuel and the oxidizer are not initially mixed. They separately enter into the combustion chamber where they mix and react [40, 66, 89]. Usually the temperature of the fuel is much lower than that oxidizer.

This study focuses on the autoignition of non-premixed methane-air mixtures at high pressures and over a wide range of air temperatures. Very few experimental studies were conducted in this area. Most research focused on the autoignition of premixed mixtures with dilutants [31, 73, 91]. Sullivan et al. [113] and Fraser et al.[102] performed non-premixed autoignition studies under engine relevant conditions. In their experiments, low-temperature pure methane was injected into high-temperature high-pressure air in order to simulate diesel environments. Further details on these experiments are provided in Sections 4.1 and 6.6, respectively. Computationally, autoignition has been studied using DNS. Some examples include the work of Mastorakos et al. [78, 80], Im et al. [50] and Sreedhara et al. [110]. However, DNS have many limitations and require special considerations (see

Section 2.4.3). The first-order CMC method implemented in this study was successfully applied to various autoignition problems. For example, Kim et al. [57, 58] used it for the prediction of the ignition delay in turbulent methane jets, and Markides et al. [76] for the autoignition of n-heptane plumes. First-order CMC was also applied for the prediction of spray autoignition by Wright et al. [123] and by Kim et al. [60]. Extensions to this method include the second-order CMC introduced by Mastorakos et al. [79] and the Doubly Conditioned Moment Closure (DCMC) method first applied by Cha et al. [17]. The second-order CMC was applied to autoignition [79], and to extinction and reignition problems [56]. DCMC was also applied to to extinction and reignition problems [17, 65]. It is also important to mention that the first order CMC has been widely used in the simulation of turbulent non-premixed flames. For example, Roomina et al. [104, 105] implemented this method for the prediction of turbulent methane-air and methanol jet flames, and Devaud et al. [21, 23] for lifted turbulent hydrogen-air flames. Many other studies are available in the CMC literature [63]. The derivation of the first-order CMC equations is given in Chapter 3.

2.2 Governing Equations

This section presents the different conservation equations. The equations of mass, linear momentum, species, and specific enthalpy are written in cartesian coordinates using tensorial notation for simplicity.

2.2.1 Mass

The conservation of mass equation is given by

$$\frac{\partial \rho}{\partial t} + \frac{\partial \left(\rho u_i\right)}{\partial x_i} = 0. \tag{2.1}$$

The first term on the left hand side (LHS) of Eq.(2.1) is local rate of change of Y_α and the second term represents convective transport.

2.2.2 Linear Momentum

The linear momentum equation is written as

$$\frac{\partial\left(\rho u_i\right)}{\partial t}+\frac{\partial\left(\rho u_i u_j\right)}{\partial x_j}=-\frac{\partial p}{\partial x_i}+\frac{\partial \tau_{ij}}{\partial x_j}+B_i. \tag{2.2}$$

The first term on the LHS of Eq.(2.2) is local rate of change of Y_α while the second accounts for convective transport. The first term on the right hand side (RHS) is the pressure gradient and the second represents transport via viscous forces. Here τ_{ij} is the shear stress tensor. This quantity is expressed using the Stokes hypothesis as

$$\tau_{ij}=-\mu\frac{2}{3}\frac{\partial u_k}{\partial x_k}\delta_{ij}+\mu\left(\frac{\partial u_i}{\partial x_j}+\frac{\partial u_j}{\partial x_i}\right), \tag{2.3}$$

where μ is the dynamic viscosity and δ_{ij} is the Kronecker delta. The last term on the RHS of Eq.(2.2), B_i, accounts for body forces in the direction of the i^{th} cartesian coordinate.

2.2.3 Species

The transport equation of a species α is

$$\frac{\partial\left(\rho Y_\alpha\right)}{\partial t}+\frac{\partial\left(\rho u_i Y_\alpha\right)}{\partial x_i}=-\frac{\partial J_i^\alpha}{\partial x_i}+\dot{\omega}_\alpha \qquad \alpha=1,2,\cdots,N_s, \tag{2.4}$$

where N_s is the total number of species in the mixture. The first term on the LHS of Eq.(2.4) is local rate of change of Y_α, while the second represents convective transport. On the RHS, the first term accounts for mass transfer by molecular diffusion. The notation J_i^α represents the molecular diffusive flux of the species. This term is modeled using Fick's first law of diffusion as

$$J_i^\alpha=-\rho D_\alpha\frac{\partial Y_\alpha}{\partial x_i}, \tag{2.5}$$

where D_α is the diffusion coefficient or diffusivity of species α. The last term on the RHS of Eq.(2.4), $\dot{\omega}_\alpha$, is the chemical source. This quantity accounts for the creation or destruction of species α via chemical reactions. Given a set of I elementary reversible reactions in a mixture consisting of N_s species, the general chemical reaction is written as [66]:

$$\sum_{\alpha=1}^{N_s}\nu'_{\alpha i}S_\alpha \underset{k_{bi}}{\overset{k_{fi}}{\leftrightarrows}} \sum_{\alpha=1}^{N_s}\nu''_{\alpha i}S_\alpha \qquad i=1,2,\ldots,I, \tag{2.6}$$

where S_α is the chemical symbol of species α and $\nu_{\alpha i}$ denotes the stoichiometric coefficient of species α in reaction i. A single prime superscript ($'$) is used with $\nu_{\alpha i}$ if S_α is a reactant while a double prime ($''$) is used if S_α is a product. k_{fi} and k_{bi} are the forward and backward specific reaction constants, respectively. The chemical source term of species α is written as the sum of the reaction rates corresponding to all the chemical reactions involving this species as

$$\dot{\omega}_\alpha = W_\alpha \sum_{i=1}^{I} \left(\nu''_{\alpha i} - \nu'_{\alpha i}\right) q_i \qquad \alpha = 1, 2, \ldots, N_s, \tag{2.7}$$

where the rate of progress for the i^{th} reaction, q_i, is computed as the difference of the forward and backward reaction rates:

$$\begin{aligned} q_i &= k_{fi} \prod_{k=1}^{N_s} \left(C_k\right)^{\nu'_{ki}} - k_{bi} \prod_{k=1}^{N_s} \left(C_k\right)^{\nu''_{ki}} \\ &= k_{fi} \prod_{k=1}^{N_s} \left(\frac{\rho Y_k}{W_k}\right)^{\nu'_{ki}} - k_{bi} \prod_{k=1}^{N_s} \left(\frac{\rho Y_k}{W_k}\right)^{\nu''_{ki}}, \end{aligned} \tag{2.8}$$

where C_k is the molar concentration of the k^{th} species. The forward specific reaction constant appearing in Eqs.(2.6) and (2.8) is written in an Arrhenius temperature-dependent form. For instance, in a reaction i, k_{fi} is expressed as

$$k_{fi} = A_{0_i} T^{b_i} \exp\left(-\frac{T_{a_i}}{T}\right) = A_{0_i} T^{b_i} \exp\left(-\frac{E_{a_i}}{R_u T}\right), \tag{2.9}$$

where A_{0_i} is the frequency factor, b_i is the reaction exponent (the Boltzmann factor), R_u is the universal gas constant, $T_{a,i}$ and $E_{a,i}$ are the activation temperature and energy, respectively.

2.2.4 Specific Enthalpy

The specific enthalpy (h) equation is written as

$$\frac{\partial\left(\rho h\right)}{\partial t} + \frac{\partial\left(\rho u_i h\right)}{\partial x_i} = \frac{\partial p}{\partial t} + \frac{\partial\left(u_i p\right)}{\partial x_i} + \frac{\partial\left(u_j \tau_{ij}\right)}{\partial x_j} + \dot{q}_{rad} + u_i B_i - \frac{\partial \Im_i^\alpha}{\partial x_i}. \tag{2.10}$$

The first two terms on the LHS and RHS of Eq.(2.10) represent the local rate of change and the convective transport of enthalpy and pressure, respectively. The third term on the

RHS accounts for dissipation by viscous stresses (frictional heating), $\dot{q}_{rad}$ is the radiation heat transfer and $u_i B_i$ is the work done by body forces. The last term on the RHS is the spatial change of the heat flux, $\Im_i^\alpha$. This term accounts for both conduction heat transfer and enthalpy transport by molecular diffusive fluxes ($\wp_i^\alpha$ defined in Eq.(2.5)). $\Im_i^\alpha$ is thus written as the sum of those two quantities,

$$\begin{aligned}\Im_i^\alpha &= -\frac{\lambda}{c_p}\frac{\partial h}{\partial x_i} + \sum_{\alpha=1}^{n}\left[h_\alpha\left(\frac{\lambda}{c_p} - \rho D_\alpha\right)\frac{\partial Y_\alpha}{\partial x_i}\right] \\ &= -\frac{\mu}{\mathrm{Pr}}\frac{\partial h}{\partial x_i} + \sum_{\alpha=1}^{n}\left[h_\alpha\left(\frac{\mu}{\mathrm{Pr}} - \frac{\mu}{\mathrm{Sc}_\alpha}\right)\frac{\partial Y_\alpha}{\partial x_i}\right] \\ &= -\frac{\mu}{\mathrm{Pr}}\left\{\frac{\partial h}{\partial x_i} + \sum_{\alpha=1}^{n}\left[h_\alpha\left(\frac{1}{\mathrm{Le}_\alpha} - 1\right)\frac{\partial Y_\alpha}{\partial x_i}\right]\right\},\end{aligned} \tag{2.11}$$

where h_α is the enthalpy of species α per unit mass, c_p is the specific heat at constant pressure and λ is the thermal conductivity. $\mathrm{Pr} = \mu c_p/\lambda$ is the Prandtl number, $\mathrm{Sc}_\alpha = \mu/(\rho D_\alpha)$ is the Schmidt number and $\mathrm{Le}_\alpha = \mathrm{Sc}_\alpha/\mathrm{Pr} = \lambda/(\rho c_p D_\alpha)$ is the Lewis number.

2.3 Averaging Techniques in Turbulent Flows

Two steps are required in order to compute the mean of the conservation equations. In the first step, the instantaneous quantity of interest is written as the sum of its mean and a fluctuation about this mean. This process is called decomposition. In the second step, the decomposed quantity is substituted into the corresponding transport equation, and finally the mean of the resulting expression is taken. This section includes two averaging techniques: Reynolds and Favre averaging.

2.3.1 Reynolds Averaging

Given an unsteady random process, any physical quantity can be written as the sum of an ensemble-average (mean) value and a fluctuation about that value [99]. Thus, a quantity $\psi(x_i, t)$ is expressed as

$$\psi(x_i, t) = \bar{\psi}(x_i, t) + \psi'(x_i, t), \tag{2.12}$$

such that $\bar{\psi}'(x_i,t)=0$. If N elements are available in the ensemble, the ensemble-average of $\psi(x_i,t)$ is calculated using

$$\bar{\psi}(x_i,t)=\lim_{N\to\infty}\frac{1}{N}\sum_{n=1}^{N}\psi(x_i,t), \tag{2.13}$$

where N must be large enough in order to eliminate the effects of the fluctuations $\psi'(x_i,t)$.

2.3.2 Favre Averaging

In the case of flows with considerable density variations, a density-weighted average is used to find the mean the different physical quantities. This type of averaging is referred to as Favre averaging [28]. The decomposition of a quantity ψ in this case is the similar to the Reynolds decomposition. $\psi(x_i,t)$ is written as the sum of a Favre-average value and a fluctuation about that value:

$$\psi(x_i,t)=\tilde{\psi}(x_i,t)+\psi''(x_i,t), \tag{2.14}$$

where the double prime superscript is used to distinguish the Favre fluctuations from the Reynolds fluctuations. The difference between the two decomposition methods lies in treatment of the mean fluctuations. In Reynolds decomposition, it is required that $\bar{\psi}'(x_i,t)=0$, while in Favre decomposition, the mean of the density-fluctuation product must vanish, that is

$$\overline{\rho\psi''(x_i,t)}=0. \tag{2.15}$$

Accordingly,

$$\begin{aligned}\overline{\rho\psi(x_i,t)}&=\overline{\rho\big[\tilde{\psi}(x_i,t)+\psi''(x_i,t)\big]}\\&=\overline{\rho\tilde{\psi}(x_i,t)}+\overline{\rho\psi''(x_i,t)}\\&=\bar{\rho}\tilde{\psi}(x_i,t).\end{aligned} \tag{2.16}$$

Hence, $\tilde{\psi}(x_i,t)$ can be written as

$$\tilde{\psi}(x_i,t)=\frac{\overline{\rho\psi(x_i,t)}}{\bar{\rho}}. \tag{2.17}$$

2.3.3 Favre-Averaged Balance Equations

Since reactive flows involve large density variations, Favre-averaging is usually used in turbulent combustion calculations. Decomposing the different quantities in the balance equation presented in section 2.2 using Eq.(2.14), then taking the mean of the resulting expressions, the Favre-averaged conservation equations are:

• Mass:

$$\frac{\partial \bar{\rho}}{\partial t} + \frac{\partial \left(\bar{\rho}\tilde{u}_i\right)}{\partial x_i} = 0. \tag{2.18}$$

• Linear momentum:

$$\frac{\partial \left(\bar{\rho}\tilde{u}_i\right)}{\partial t} + \frac{\partial \left(\bar{\rho}\tilde{u}_i\tilde{u}_j\right)}{\partial x_i} = -\frac{\partial \bar{p}}{\partial x_i} + \frac{\partial \bar{\tau}_{ij}}{\partial x_j} - \frac{\partial \widetilde{\left(\bar{\rho}u_i''u_j''\right)}}{\partial x_j} + \bar{B}_i. \tag{2.19}$$

• Species:

$$\frac{\partial(\bar{\rho}\tilde{Y}_\alpha)}{\partial t} + \frac{\partial(\bar{\rho}\tilde{u}_i\tilde{Y}_\alpha)}{\partial x_i} = \frac{\partial}{\partial x_i}\left(\overline{\rho D_\alpha \frac{\partial Y_\alpha}{\partial x_i}} - \widetilde{\bar{\rho}u_i''Y_\alpha''}\right) + \bar{\dot{\omega}}_\alpha. \tag{2.20}$$

• Specific Enthalpy:

$$\frac{\partial(\bar{\rho}\tilde{h})}{\partial t} + \frac{\partial(\bar{\rho}u_i\tilde{h})}{\partial x_i} = -\frac{\partial \bar{\Im}_i^\alpha}{\partial x_i} + \frac{\partial \bar{p}}{\partial t} + \frac{\partial \overline{u_i p}}{\partial x_i} - \frac{\partial \widetilde{\left(\bar{\rho}u_i''h''\right)}}{\partial x_i} + \frac{\partial \overline{u_j \tau_{ij}}}{\partial x_j} + \overline{u_i B_i} + \bar{\dot{q}}_{rad}. \tag{2.21}$$

The Reynolds stresses $\widetilde{\bar{\rho}u_i''u_j''}$ (Eq.(2.19)) and the turbulent fluxes $\widetilde{\bar{\rho}u_i''Y_\alpha''}$ (Eq.(2.20)) and $\widetilde{\bar{\rho}u_i''h''}$ (Eq.(2.21)) are in unclosed form. These issues are addressed in the next section.

2.4 Turbulence Modeling

Turbulence modeling is the process in which closure for the unknown turbulence correlations, such as the Reynolds stresses and the turbulent fluxes, is sought in order to close the system of the governing equations. This section reviews the Reynolds averaged Navier-Stokes (RANS) models in addition to the state of the art Large Eddy Simulations (LES) and Direct Numerical Simulations (DNS).

2.4.1 RANS Models

RANS models involve solving the averaged instantaneous balance equations. In RANS, the Reynolds stresses are obtained from a turbulence viscosity model or by direct modeling [99]. The order of a model is defined as the number of additional equations that need to be solved in order to determine the unknown turbulence correlations. This section reviews zero, one and two-equation models, the Reynolds stress model, and the applicability of RANS models to turbulent reacting flows.

Zero-Equation Models

Zero-equation models are the simplest among turbulence models since the closure of the shear stress term is algebraic and does not introduce any new partial differential equations (PDE). Two models were proposed: the uniform turbulent viscosity model introduced by Bousinesq and the mixing-length model suggested by Prandtl [99, 69, 46]. Bousinesq proposed [69]:

$$\overline{\rho}\widetilde{u_1'u_2'} = -\varepsilon_m \frac{\partial \tilde{u}_1}{\partial x_2}, \tag{2.22}$$

where ε_m is a constant from which the name of the model originates. Prandtl suggested the mixing-length model given by [69]:

$$\overline{\rho}\widetilde{u_1'u_2'} = -\mu_t \frac{\partial \tilde{u}_1}{\partial x_2}, \tag{2.23}$$

where μ_t is the turbulent viscosity. μ_t is given by:

$$\mu_t = l_m^2 \left| \frac{\partial \tilde{u}_1}{\partial x_2} \right|, \tag{2.24}$$

where l_m is the mixing length, a constant dependent on the nature of the problem. This model yields good predictions in free shear and boundary layer flows [99]. Although cheap and easy to implement, the mixing length model is incomplete since the mixing length l_m needs to be specified, which is a very hard task in complex flows [99]. Furthermore, it is incapable of capturing many flow details such as separation and recirculation.

One-Equation Models

An additional PDE for the turbulent kinetic energy, $\tilde{k} = \widetilde{u_i''^2}/2$, is solved [51, 89]:

$$\overline{\rho}\frac{\partial \tilde{k}}{\partial t} + \overline{\rho}u_k\frac{\partial \tilde{k}}{\partial x_k} = \frac{\partial}{\partial x_k}\left[\left(\frac{\mu_t}{\sigma_k} + \mu\right)\frac{\partial \tilde{k}}{\partial x_k}\right] + \overline{\rho}\mathcal{P} - \overline{\rho}\tilde{\varepsilon}, \tag{2.25}$$

where $\mu_t = \overline{\rho}C\tilde{k}^{1/2}/l_m$ is the turbulent viscosity, $\tilde{\varepsilon} = C_D\tilde{k}^{3/2}/l_m$ is the turbulent eddy dissipation, σ_k is the turbulent Prandtl number, l is a length scale, and C and C_D are empirical constants. C depends on the type of the flow and C_D is usually set equal to 0.09. $\mathcal{P} = -\widetilde{u_i''u_j''}(\partial\tilde{u}_j/\partial x_i)$ is the production rate in which $\widetilde{u_i''u_j''}$ is modeled as

$$\widetilde{u_i''u_j''} = \frac{2}{3}\delta_{ij}\left(\tilde{k} - \frac{\mu_t}{\overline{\rho}}\frac{\partial \tilde{u}_k}{\partial x_k}\right) - \frac{\mu_t}{\overline{\rho}}\left(\frac{\partial \tilde{u}_i}{\partial x_j} + \frac{\partial \tilde{u}_j}{\partial x_i}\right). \tag{2.26}$$

This model is slightly more accurate than the mixing model presented in the previous section and still requires the specification of the length scale [99]. Generally, one-equation models are not successful except when applied to flows with constant production to dissipation ratio (i.e. strong shear flows). The only advantage they have over the zero-equation models is that the turbulent kinetic energy is calculated.

Two-Equation Models

As discussed in the previous section, when using one-equation models, a length scale must be provided in order to close the turbulent kinetic energy equation, Eq.(2.25). Two-equation models overcome this difficulty by introducing besides the $\tilde{k}$-equation, an additional PDE that is related to the turbulence length scale. Many variables were proposed for this equation: ω by Kolmogorov [64], ω^2 by Saffman [106], ε by Jones et al. [51] and τ by Speziale et al. [109]. The k-ε model is one the most widely used models due to its simplicity, completeness and wide range of applicability. It consists of an equation for $\tilde{k}$ (Eq.(2.25)), another for $\tilde{\varepsilon}$ and a set of model constants. The $\tilde{\varepsilon}$-equation is given by [51, 89]:

$$\overline{\rho}\frac{\partial \tilde{\varepsilon}}{\partial t} + \overline{\rho}u_k\frac{\partial \tilde{\varepsilon}}{\partial x_k} = \frac{\partial}{\partial x_k}\left[\left(\frac{\mu_t}{\sigma_\varepsilon} + \mu\right)\frac{\partial \tilde{\varepsilon}}{\partial x_k}\right] + C_{\varepsilon 1}\frac{\overline{\rho}\mathcal{P}\tilde{\varepsilon}}{\tilde{k}} - C_{\varepsilon 2}\frac{\overline{\rho}\tilde{\varepsilon}^2}{\tilde{k}}, \tag{2.27}$$

with

$$\mu_t = C_\mu\bar{\rho}\frac{\tilde{k}^2}{\tilde{\varepsilon}} \tag{2.28}$$

in both Eqs.(2.25) and (2.27). The standard model constants are:

$$C_\mu = 0.09,\ C_{\varepsilon 1} = 1.44,\ C_{\varepsilon 2} = 1.92,\ \sigma_k = 1.0,\ \text{and}\ \sigma_\varepsilon = 1.3. \tag{2.29}$$

The turbulence length and time scales are determined from $\tilde{k}$ and $\tilde{\varepsilon}$ as

$$l = \frac{\tilde{k}^{3/2}}{\tilde{\varepsilon}} \tag{2.30}$$

and

$$\tau = \frac{\tilde{k}}{\tilde{\varepsilon}}, \tag{2.31}$$

respectively. The k-ε model is applicable to a wide variety of turbulent flows. When applied to a round jet, it is known to overpredict the spreading rate [99], which results in an underpredicted penetration length. A possible way to solve this problem is to adjust the values of $C_{\varepsilon 1}$ and $C_{\varepsilon 2}$. Details on this technique are provided in Chapter 4. Other solution options include the addition of a source term to the $\tilde{\varepsilon}$-equation, but generally, this modification results in an poor performance when compared to the standard model [99].

Reynolds-Stress Models

The main advantage of the Reynolds-Stress Models (RSM) over the models presented so far is that the turbulent viscosity hypothesis is not needed to model the shear stresses [99]. Transport equations derived directly from the momentum equations are solved for the individual stresses $\widetilde{u_i'' u_j''}$ in addition to an equation providing a turbulence length or time scale such as the $\tilde{\varepsilon}$-equation. The detailed equations can be found in [99, 69]. This model is applicable to any turbulent flow [99] and overall, it is more accurate than the two-equation models. However, two major drawbacks of this model are its complexity and relatively high computational cost. For instance, seven equations need to be solved (six for $\widetilde{u_i'' u_j''}$ and one for $\tilde{\varepsilon}$) compared to two in the case of two-equation models [99].

RANS models have been extensively used in in turbulent combustion simulations. Peters [89] notes that the usage of RANS in such flows tends to suppress large scale instabilities in steady state situations, a frequently occurring phenomenon in combustion. He explains this by the fact that RANS uses an effective turbulent viscosity that is much

larger in magnitude than the molecular viscosity. However, modeling reacting flows with RANS remains attractive due to the relatively low computational cost compared to other techniques LES and DNS.

2.4.2 LES

LES are three-dimensional time-dependent simulations in which large scale geometry-dependent motions are resolved and smaller scale self-similar motions are modeled [29, 30, 99]. The idea behind LES originates from the fact that the transport of the conserved flow properties is mainly achieved by the energetic large eddies, while the smaller and weaker eddies contribute less to the transport of those properties [29]. LES involves four major operations [99]:

1. Filtering process in which the velocity is decomposed into a filtered component which describes the motion of the large eddies (resolved scale component) and a residual component (subgrid scale component). Filtering requires the usage of a filter function,

2. Derivation of the equation of the filtered velocity field from the Navier-Stokes equations,

3. Modeling of the residual stress tensor in the momentum equation,

4. Numerical solution of the filtered equations.

LES is more accurate than the two-equation models and the RSM since most of the energy spectrum is resolved, while modeling is only performed at small scales. Regarding computational cost, LES falls between the RSM and DNS. LES is generally applicable to any turbulent flow. However, special considerations are needed when solving high-speed compressible flows and and reacting flows [99]. Further details on LES can be found in references [99, 29].

For the case of reacting flows, Cook et al. [19] suggested a methodology based on a presumed form for the subgrid scale probability density function of a conserved scalar. Colucci et al. [18] proposed the Filtered Density Function (FDF) approach wherein a

transport equation for the FDF is solved and the effects of scalar mixing and convection within the subgrid are modeled.

2.4.3 DNS

In DNS all the scales of motion are resolved by solving directly the instantaneous three-dimensional Navier-Stokes equations, without performing any averaging or modeling [29, 99]. For this reason, DNS is considered to be the most accurate approach in Computational Fluid Dynamics (CFD). However, the computational cost in such simulations is very high. Usually the computational domain is chosen to be a box of side $\mathcal{L}$, such that $\mathcal{L}$ is large enough to represent the different eddy sizes. In order to resolve all the scales of motion, the grid spacing Δx must be set to fractions of the smallest length-scale, the Kolmogorov scale denoted by η. Thus the number of grid points in each dimension must be at least $\mathcal{L}/\eta$, which is proportional to $\mathrm{Re}_{\mathcal{L}}^{3/4}$. Thus, the overall cost in three-dimensions is of the order of $\mathrm{Re}_{\mathcal{L}}^{9/4}$ [29, 99]. This is why DNS is restricted to small Reynolds numbers. Another important consideration is the time step Δt. The choice of Δt depends on the desired degree of accuracy. Due to the limitations discussed above, DNS is restricted to very simple flows. Still, it is a valuable benchmarking tool in the process of developing reliable turbulence models, as it provides the most accurate solution for a given problem.

In the case of reacting flows, in addition to the aforementioned limitations, the requirement of solving an additional set of transport equations (one for each species in the mixture) increases the computational cost further. For this reason the chemical kinetics mechanisms used in the calculations are usually reduced and one-step irreversible chemical reactions are assumed. Many DNS studies have been conducted in this area. For instance, the work done by Swaminathan et al. [116], Eswaran et al. [27], Mell et al. [81], Baum et al. [4], Trouvé et al. [118], Brethouwer et al. [13].

2.5 Turbulent Reacting Flows

This section describes the stochastic behavior of turbulent reacting flows, and discusses the non-linearity of the chemical source and the turbulence-chemistry interactions. The structure and the characteristics of the non-premixed combustion mode are briefly presented,

and the mixture fraction variable and its variance are introduced.

2.5.1 Stochastic Description of Turbulent Reacting Flows

Turbulent combustion is a stochastic process in which the velocity components and scalars quantities such as the temperature, the pressure and the species concentrations are fluctuating variables. One way to quantify these variables is to characterize them by their probability density function (PDF) [63]. Given a stochastic variable Ψ and a sample space variable, say ψ, the cumulative probability $C(\Psi < \psi)$ is defined as the probability of occurrence of Ψ such that $\Psi < \psi$. With this definition in mind, C is an increasing function bounded by 0 and 1 since $C(\Psi < \psi) \to 0$ as $\psi \to -\infty$ and $C(\Psi < \psi) \to 1$ as $\psi \to +\infty$. This behavior is illustrated in Figure 2.1. In a similar fashion, given the sample variables ψ_1 and ψ_2, $C(\psi_1 < \Psi < \psi_2) = C(\Psi < \psi_2) - C(\Psi < \psi_1)$.
Referring to Figure 2.2, the PDF, P, is related to C by:

$$P(\psi) = \lim_{\Delta\psi \to 0} \frac{C(\Psi < \psi + \Delta\psi) - C(\Psi < \psi)}{\Delta\psi} = \frac{dC(\Psi < \psi)}{d\psi}, \tag{2.32}$$

such that

$$\int_{-\infty}^{+\infty} P(\psi) d\psi = 1. \tag{2.33}$$

The expectation of Ψ is found using

$$\langle \Psi \rangle = \int_{-\infty}^{+\infty} \psi P(\psi) d\psi. \tag{2.34}$$

This definition can be extended to any function $F(\Psi)$:

$$\langle F(\Psi) \rangle = \int_{-\infty}^{+\infty} F(\psi) P(\psi) d\psi. \tag{2.35}$$

The joint PDF of two events ψ_1 and ψ_2 is expressed using Bayes' theorem as

$$P(\psi_1, \psi_2) = P(\psi_1 | \Psi_2 = \psi_2) P(\psi_2). \tag{2.36}$$

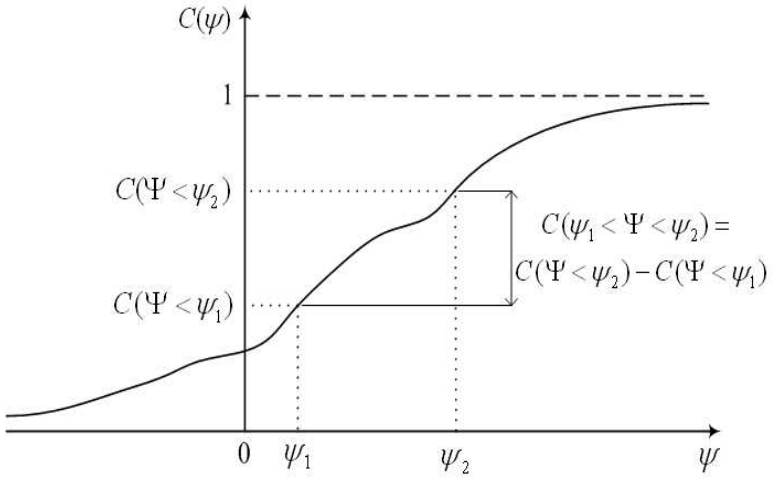

Figure 2.1: Cumulative distribution function (reproduced from reference [63]).

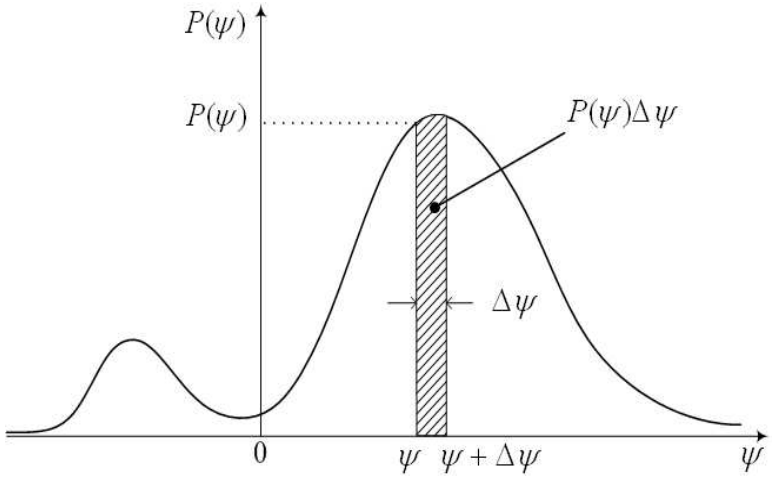

Figure 2.2: Probability of the event $\psi < \Psi < \psi + \Delta\psi$ (reproduced from reference [63]).

The conditional expectation of Ψ_1 such that $\Psi_2 = \psi_2$ is therefore

$$\begin{aligned}\langle \Psi_1 | \Psi_2 = \psi_2 \rangle &= \int_{-\infty}^{+\infty} \psi_1 P(\psi_1 | \Psi_2 = \psi_2) d\psi_1 \\ &= \frac{\int_{-\infty}^{+\infty} \psi_1 P(\psi_1, \psi_2) d\psi_1}{P(\psi_2)}.\end{aligned} \tag{2.37}$$

Similarly, this definition can be extended to the conditional expectation of any function $F(\Psi_1)$ conditioned at $\Psi_2 = \psi_2$:

$$\begin{aligned}\langle F(\Psi_1) | \Psi_2 = \psi_2 \rangle &= \int_{-\infty}^{+\infty} F(\psi_1) P(\psi_1 | \Psi_2 = \psi_2) d\psi_1 \\ &= \frac{\int_{-\infty}^{+\infty} F(\psi_1) P(\psi_1, \psi_2) d\psi_1}{P(\psi_2)}.\end{aligned} \tag{2.38}$$

Moreover, the unconditional expectation of $F(\Psi_1)$ can be retrieved from $\langle F(\Psi_1) | \Psi_2 = \psi_2 \rangle$ using

$$\langle F(\Psi_1) \rangle = \int_{-\infty}^{+\infty} \langle F(\Psi_1) | \Psi_2 = \psi_2 \rangle P(\psi_2) d\psi_2. \tag{2.39}$$

The relations above will be extensively used in the subsequent chapters.

2.5.2 Non-Linearity of the Chemical Source Term

In reacting flows, the mean of the chemical source term, $\bar{\dot{\omega}}_\alpha$ (with $\alpha = 1, 2, \ldots, N_s$), is required in order to close the governing balance equations. However, $\dot{\omega}_\alpha$ is a highly non-linear function of the density ρ, the temperature T and the species concentrations Y_α. Thus $\bar{\dot{\omega}}_\alpha$ cannot be easily expressed in terms of the means of these quantities. That is,

$$\bar{\dot{\omega}}_\alpha(\rho, T, Y_\alpha) \neq \dot{\omega}_\alpha(\bar{\rho}, \widetilde{T}, \tilde{Y}_\alpha). \tag{2.40}$$

A thorough overview on the non-linear nature of $\dot{\omega}_\alpha$ is provided by Veynante et al. [121] and Poinsot et al. [93]. Using a Taylor series expansion for $\bar{\dot{\omega}}_\alpha$ (expressed using the Arrhenius equation), they show that in the simplest case of an irreversible chemical reaction,

algebraic expressions and transport equations are required to close the resulting fluctuations. Furthermore, they note that $\bar{\dot{\omega}}_\alpha$ is poorly calculated if only few terms of the series are considered (large truncation errors). This means that $\bar{\dot{\omega}}_\alpha$ is strongly affected by the fluctuations in the flow field. Therefore, this quantity should be carefully modeled. Several strategies are discussed in Section 2.6.

2.5.3 Turbulence-Chemistry Interactions

The interactions between turbulence and chemistry can be described in terms of the Damköhler number, Da. This number is defined as the ratio of the turbulent time scale (τ_t) to the chemical time scale (τ_c):

$$D_a = \frac{\tau_t}{\tau_c}. \tag{2.41}$$

If $D_a > 1$, then τ_c is smaller than τ_t, meaning that the reaction time is shorter than the mixing time. In the case where $D_a \gg 1$, the chemical reactions can be assumed to be infinitely fast (local chemical equilibrium assumption). This corresponds to a thin reaction zone that is convected by the turbulent flow field [121]. On the other hand, if $D_a < 1$, then the reaction time is longer than the mixing time and the chemistry is considered to be slow. In this case, the species are mixed by the flow field before reactions start to take place [121].

2.5.4 Non-Premixed Combustion

In non-premixed combustion the fuel and the oxidizer are not initially mixed. They separately enter into the combustion chamber where they mix and burn [40, 66, 89]. The resulting flame is called a diffusion flame because the molecular diffusion (mixing) rate is slower than the chemical reaction rate (or in other words, the mixing time scale is longer than the chemical reaction time scale ($D_a \gg 1$)), which makes mixing the controlling agent of the burning process [89, 121, 66, 40]. For this reason, the assumption of infinitely fast chemistry (local chemical equilibrium) is reasonable in many situations. However, this assumption becomes invalid when the mixing time scale is not too large. In this case,

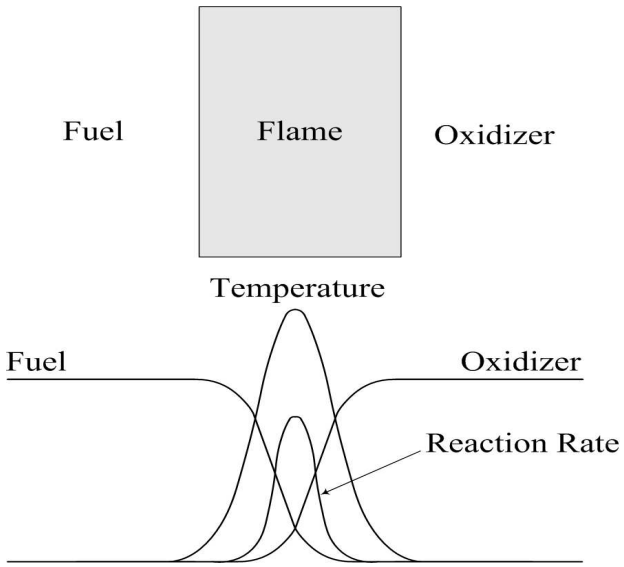

Figure 2.3: Structure of a laminar non-premixed flame (reproduced from reference [121]).

nonequilibrium effects should be taken into consideration [89]. The structure of a non-premixed (diffusion) flame is shown in Figure 2.3. The fuel and the oxidizer are located on both sides of the reaction zone where chemical reactions take place. This zone is wide due to continuous interdiffusion of reactants and products [40, 89]. As for the rate of burning, it is controlled by the molecular diffusion of the reactants towards the reaction zone [121]. As displayed in Figure 2.3, the concentration of the reactants decrease in this zone, while the temperature and the overall reaction rate increase, accompanied by heat release. Non-premixed flames are very sensitive to turbulence. For instance, they are incapable of propagating and mainly controlled by mixing [121]. In addition, they are sensitive to stretch and prone to quenching by turbulent fluctuations [93]. This combustion mode is not discussed further since this study is confined to the autoignition of a non-premixed methane-air jet, and flames are beyond the scope of this work. Further details on non-premixed laminar and turbulent flames can be found in references [66, 40, 93], and [11, 89, 93, 121], respectively.

2.5.5 The Mixture Fraction Variable and its Variance

The Favre-averaged mixture fraction $\tilde{\xi}$ and its variance $\widetilde{\xi''^2}$ are two important quantities in the modeling of turbulent non-premixed combustion. The interest in conserved scalar quantities such as $\tilde{\xi}$ is motivated by the fact that simple presumed PDFs based on $\tilde{\xi}$ and $\widetilde{\xi''^2}$ can be used in order to describe the stochastic behavior of the different reacting scalars [30]. For instance, two widely used presumed forms are the Gaussian distribution and the β-PDF (Section 3.3.2).

Considering a two-feed system where fuel and oxidizer are supplied through different inlets, ξ is defined as [89]:

$$\xi = \frac{\dot{m}_1}{\dot{m}_1 + \dot{m}_2}, \tag{2.42}$$

where $\dot{m}_1$ and $\dot{m}_2$ denote the mass flow rates of the fuel and oxidizer streams, respectively. Bilger [6, 7] formulated another definition based on the elemental mass fraction of the reacting species. He suggested:

$$\xi = \frac{\beta - \beta_2}{\beta_1 - \beta_2}, \tag{2.43}$$

where β is a coupling function that vanishes at stoichiometry and the subscripts 1 and 2 denote the fuel and oxidizer streams, respectively. The details on the construction of β can be found in references [6, 7, 89]. ξ in Eqs.(2.42) and (2.43) varies between 0 and 1. Assuming that the species' diffusivities are all equal to D, the mixture fraction transport equation is written as [89]:

$$\frac{\partial(\rho\xi)}{\partial t} + \frac{\partial(\rho u_i \xi)}{\partial x_i} = \frac{\partial}{\partial x_i}\left(\rho D \frac{\partial \xi}{\partial x_i}\right). \tag{2.44}$$

The LHS terms represent the local rate of change and convection of ξ. The term on the RHS accounts for ξ transport by means of molecular diffusion. Taking the Favre-average of Eq.(2.44), one obtains:

$$\frac{\partial(\bar{\rho}\tilde{\xi})}{\partial t} + \frac{\partial(\bar{\rho}\tilde{u}_i\tilde{\xi})}{\partial x_i} = \frac{\partial}{\partial x_i}\left(\overline{\rho D \frac{\partial \xi}{\partial x_i}} - \bar{\rho}\widetilde{u_j''\xi''}\right). \tag{2.45}$$

The turbulent flux $\widetilde{u_i''\xi''}$ appearing on the RHS of Eq.(2.45) is usually modeled using the gradient diffusion hypothesis, which introduces the turbulent diffusivity, D_t (Section 3.3.1).

Since the magnitude of D_t is much larger than the magnitude of the molecular diffusivity D, the mean of the term corresponding to transport by molecular diffusion (first term inside the parentheses in Eq.(2.45)) is neglected and Eq.(2.46) reduces to:

$$\frac{\partial(\bar{\rho}\tilde{\xi})}{\partial t} + \frac{\partial(\bar{\rho}\tilde{u}_i\tilde{\xi})}{\partial x_i} = -\frac{\partial(\bar{\rho}\widetilde{u_j''\xi''})}{\partial x_i}. \tag{2.46}$$

Another equation is needed to compute the variance of the mixture fraction. The Favre-averaged transport equation of $\widetilde{\xi''^2}$ is given by [89]:

$$\frac{\partial(\bar{\rho}\widetilde{\xi''^2})}{\partial t} + \frac{\partial(\bar{\rho}\tilde{u}_i\widetilde{\xi''^2})}{\partial x_i} = -\frac{\partial(\bar{\rho}\widetilde{u_j''\xi''^2})}{\partial x_i} - 2\bar{\rho}\widetilde{u_i''\xi''}\frac{\partial\tilde{\xi}}{\partial x_i} - 2\bar{\rho}D\widetilde{\left(\frac{\partial\xi''}{\partial x_i}\right)^2}. \tag{2.47}$$

Once Eqs.(2.45) and (2.47) are solved, $\tilde{\xi}$ and $\widetilde{\xi''^2}$ are used as input parameters in the presumed PDF.

2.6 Turbulent Combustion Modeling

Before proceeding to the formulation of the CMC method, it is important at this stage to review the turbulent combustion models that are available in the literature. Models for non-premixed combustion with infinitely fast and finite-rate chemistry are emphasized.

2.6.1 Eddy Break-Up and Eddy Dissipation Models

The Eddy Break-Up (EBU) model was suggested by Spalding [108] for premixed flames exhibiting infinitely fast chemical reactions. In such flames, since the mixing time-scale is much larger than the chemical time-scale, mixing is the rate-determining process. The idea behind the EBU model is to replace the chemical time-scale by the larger turbulence time scale, k/ε . Accordingly, Spalding suggested the following closure for the chemical source term [108]:

$$\overline{\dot{\omega}}_P = \rho C\frac{\varepsilon}{k}\left(\overline{Y_P''^2}\right)^{\frac{1}{2}}, \tag{2.48}$$

where C is the EBU constant and $\overline{Y_P''^2}$ is the variance of the products mass fraction. Magnussen et al. [75] proposed a modification to Eq.(2.48) by substituting $\overline{Y_P''^2}$ for the

mean mass fraction of the deficient species in the mixture [89]. This model is called the Eddy Dissipation Model (EDM). In EDM, the chemical source term is modeled as the minimum of three rates:

$$\overline{\dot{\omega}} = \overline{\rho} A \frac{\varepsilon}{k} \min\left(\overline{Y}_F, \frac{1}{\nu}\overline{Y}_O, \frac{B}{1+\nu}\overline{Y}_P\right), \tag{2.49}$$

where $\overline{Y}_F$, $\overline{Y}_O$ and $\overline{Y}_P$ are the mean mass fractions of fuel, oxidizer and products, respectively. A and B are model constants, and ν is the stoichiometric oxidizer to fuel mass ratio.

The above models are attractive due to their simplicity and ease of implementation. However, their performance is generally poor. This is due to the fact that they use the turbulence time-scale instead of the chemical time scale, thus entirely neglecting the effect of chemical kinetics. Another drawback is that the model constants are not universal and need to be adjusted in most problems [89]. The EBU model is extendable to non-premixed combustion by incorporating the mixture fraction variable [6].

2.6.2 Linear Eddy Model

The Linear Eddy Model (LEM) was initially introduced for non-reactive flows by Kerstein [53], who later extended the model to reactive flows [54, 55]. In LEM, transport and mixing of a reactive scalar $\phi_i(\mathbf{x}, t)$ in a turbulent flow field are computed along transverse lines that move with the mean fluid velocity. Two steps are required to perform the calculations. The first step considers the time evolution of ϕ_i in one dimension by means of diffusion and chemistry. This requires the numerical solution of the parabolic equation

$$\frac{\partial(\rho\phi_i)}{\partial t} = \frac{\partial}{\partial x}\left(\rho D_i \frac{\partial \phi_i}{\partial x}\right) + \dot{\omega}_i. \tag{2.50}$$

The second step accounts for the effect of convective transport. This step involves a sequence of random processes along the transverse line called "block inversions" [53]. Each inversion may be viewed as a representation of the effect of an individual eddy on the scalar field [89]. LEM is applicable to both premixed and non-premixed combustion. However, this method is computationally expensive because the calculations are performed using the smallest turbulence length-scale of the flow field (to represent all the eddies).

2.6.3 Laminar Flamelet Model

The Laminar Flamelet (LF) concept was initially introduced by Williams [122]. Peters [89] defines flamelets as thin reactive-diffusive layers embedded within a non-reactive turbulent flow field. This description is only valid when the chemical time-scale (specifically the time-scale of the rate-determining chemical reaction) is very small compared to the convection and diffusion time-scales ($D_a \gg 1$). In such a situation, chemical activity is highest within a very thin layer. If the thickness of this layer is smaller than the Kolmogorov length-scale, turbulence does not affect the local structure of the flame and the flame is therefore considered to be locally laminar [89]. Peters [90] and Kuznetsov [67] independently derived the LF equations for non-premixed combustion. In order to couple turbulence and chemistry, two quantities are used: the conserved mixture fraction and the instantaneous scalar dissipation rate. The mixture fraction transport equation is given by Eq.(2.44). The flame (stoichiometric) surface is determined by setting $\xi(x_i, t) = \xi_{st}$, ξ_{st} being the stoichiometric mixture fraction. For a reactive scalar ψ_i, the laminar flamelet equation near the stoichiometric surface is given by [87]:

$$\rho \frac{\partial \psi_i}{\partial t} = \frac{\rho}{Le_i} \frac{\chi}{2} \frac{\partial^2 \psi_i}{\partial \xi^2} + \dot{\omega}_i, \tag{2.51}$$

where χ is the scalar dissipation rate defined as

$$\chi = 2D \left(\frac{\partial \xi}{\partial x_i} \right)^2. \tag{2.52}$$

The steady flamelet model is described here. Closure of the chemical source term is achieved in a two-step process. The first step involves solving the steady state laminar flamelet equations numerically. The solution is then tabulated in a two-dimensional flamelet library. The entries of this library consist of the mass fractions of the species and the temperature, all functions of ξ and χ. In the second step, the means of the quantities of interest are computed, which requires the knowledge of the joint PDF $\tilde{P}(\xi, \chi)$. If $\tilde{P}(\xi, \chi)$ is known, the Favre-average of ψ_i, $\tilde{\psi}_i$, is computed using the integral

$$\tilde{\psi}_i = \int_0^1 \int_0^\infty \psi_i(\xi, \chi) \tilde{P}(\xi, \chi) d\chi_{st} d\xi. \tag{2.53}$$

The steady flamelet model is only valid in the case of infinitely fast chemistry. If the chemical time scale is of the order of or greater than the turbulence time scale (i.e. slow chemistry with $D_a \sim 1$ or $D_a > 1$), the transient term in Eq.(2.51) is retained and a Lagrangian approach is adopted. This model is known as the Lagrangian or unsteady laminar flamelet model [89]. This case is not discussed further. Additional details on the laminar flamelet model can be found in Peters [87, 88, 89] and Bray et al. [12].

2.6.4 Joint Probability Density Function Model

In this method, the joint PDF transport equation of the velocity and the reactive scalars is solved. Pope [96] derived this equation by coupling the momentum and species transport equations through an arbitrary one-point scalar function of the random velocity and composition fields $\mathbf{u}$ and $\mathbf{Q}$, $R(\mathbf{u}, \mathbf{Q})$. The end result is given by:

$$\begin{aligned} \rho\frac{\partial P}{\partial t} + \rho u_i \frac{\partial P}{\partial x_i} + \left(\rho g_i - \frac{\partial \langle p\rangle}{\partial x_i}\right)\frac{\partial P}{\partial u_i} + \sum_{\alpha=1}^{N_s}\frac{\partial}{\partial Q_\alpha}\left(\dot{\omega}_\alpha P\right) = \\ \frac{\partial}{\partial u_i}\left(\left\langle -\frac{\partial \tau_{ij}}{\partial x_i} + \frac{\partial p'}{\partial x_i}\middle| \mathbf{u}, \mathbf{Q}\right\rangle P\right) + \sum_{\alpha=1}^{N_s}\frac{\partial}{\partial Q_\alpha}\left(\left\langle \frac{\partial \wp_i^\alpha}{\partial x_i}\middle| \mathbf{u}, \mathbf{Q}\right\rangle P\right), \end{aligned} \tag{2.54}$$

where $P = P(\mathbf{u}, \mathbf{Q}; \mathbf{x}, t)$ is the joint PDF, τ_{ij} is the shear stress (see Eq.(2.3)), $p' = p - \langle p\rangle$ is the unconditional pressure fluctuation , $\langle p\rangle$ is the unconditional average of the pressure, N_s is the total number of scalars, and $\wp_i^\alpha$ is the molecular diffusive flux (see Eq.(2.5)). The first term on the LHS of Eq.(2.54) is the rate of change of the PDF, the second represents convection in physical space, the third accounts for transport by gravity and the mean pressure gradient in velocity space, while the last term represents transport in composition space by means of chemical reactions. On the RHS, the first term is the PDF transport via viscous stresses and fluctuating pressure gradient in velocity space while the second represents transport by molecular diffusive fluxes. The LHS terms are all in closed form, hence, no approximations are needed. However, the RHS terms are problematic since they involve conditional averages of gradients with respect to both velocity and composition fields. Those two terms remain unclosed if the gradients are not included in the calculations as sample space variables [89]. Thus, in order to solve Eq.(2.54), adequate closures are required for the RHS terms. Various modeling strategies are suggested by Pope

[96]. The main advantages of the PDF approach are that the chemical source term does not require modeling and detailed finite-rate chemical kinetics can be included. Furthermore, this approach is valid for both premixed and non-premixed combustion modes. Further details on this method can be found in references [24, 30, 89, 96, 98].

2.6.5 Additional Techniques

The usage of detailed chemical kinetics in turbulent combustion simulations is computationally very expensive. Maas et al. [74] proposed the Intrinsic Low-Dimensional Manifolds (ILDM) technique in an attempt to introduce an automatic mechanism that controls the reduction of the detailed chemical kinetics used in the calculations. Rather than using directly a reduced chemical mechanism, which requires the knowledge of the reactions that are in partial equilibrium and which species are in steady state, the ILDM technique starts from a detailed chemical kinetics mechanism and performs the reduction operations based on a local time scale analysis. This technique is complimentary to the chosen combustion model. More details on ILDM can be found in references [30, 74, 89].

2.7 Conclusions

This chapter presented the conservation equations employed in this study. The differences between Reynolds and Favre averaging were discussed and the Favre-averaged conservation equations were provided. Different turbulence models were presented and briefly evaluated, with emphasis on the k-ε model. The stochastic nature of turbulent reacting flows and the probability density function approach were presented. The difficulties arising from the averaging of the chemical source term and the turbulence-chemistry interactions were visited. The non-premixed combustion mode was briefly described and the roles of the conserved mixture fraction variable and its variance were demonstrated. These two quantities will be extensively used in the CMC calculations (Chapter 3). Commonly used non-premixed turbulent combustion models were also reviewed. In particular, the eddy break-up, the linear eddy, the laminar flamelet, and the joint PDF models were presented.

The next chapter discusses the first-order Conditional Moment Closure model for non-premixed combustion. Similar to the turbulent combustion models discussed earlier, this

model provides a special treatment for the non-linear chemical source term. However, the conditional means of scalar quantities are considered rather than the unconditional ones.

Chapter 3

Conditional Moment Closure

3.1 Background

Conditional Moment Closure (CMC) is a new turbulent combustion model first derived for non-premixed combustion. In CMC, scalar quantities such as the species mass fractions and the enthalpy (or temperature) are conditionally averaged on a given value of mixture fraction. This method was independently derived by Klimenko [61] and Bilger [8]. The final results of the two formulations are mathematically identical, but each has a different starting point. Klimenko [61] suggested the joint-PDF approach in which the derivation is based on the PDF transport equation under high-Reynolds number regime. Bilger [8] introduced the decomposition approach where a scalar quantity is written as the sum of the conditional mean of the scalar and a fluctuation about the mean, the conditional fluctuation. Using this sum in the transport equation of the scalar, then taking the conditional average of the resulting expression yield the desired CMC equation. Both formulations leave some conditional terms unclosed such as the velocity, the scalar dissipation rate, the turbulent fluxes and the chemical source term. Furthermore, if the PDF transport equation is not solved, the PDF must be modeled (presumed) in order to fully close the CMC transport equations.

In the following sections, the derivation of the conditional species, enthalpy and temperature transport equation is performed using the decomposition approach. Submodels for the unclosed conditional terms are then presented and validated against Direct Numerical

Simulations (DNS). Finally, the first-order closure for the chemical source in shear flows is discussed.

3.2 CMC Equations

3.2.1 Conditional Species Transport Equation

The conditional average of the mass fraction of a species α is defined as

$$Q_\alpha(\eta, x_i, t) = \langle Y_\alpha(x_i, t)|\xi(x_i, t) = \eta\rangle, \tag{3.1}$$

where Y_α is the mass fraction of the species, $\langle|\rangle$ denotes the ensemble average of the quantity to the left of the vertical bar conditioned to the quantity to its right, ξ is the mixture fraction and η is a sample variable in mixture fraction space, such that $0 \leq \eta \leq 1$. Following the decomposition method [8, 63], Y_α is written as the sum of its conditional average Q_α and a conditional fluctuation y''_α:

$$Y_\alpha(x_i, t) = Q_\alpha(\xi(x_i, t), x_i, t) + y''_\alpha(x_i, t), \tag{3.2}$$

such that

$$\langle y''_\alpha(x_i, t)|\xi(x_i, t) = \eta\rangle = \langle Y_\alpha(x_i, t)|\xi(x_i, t) = \eta\rangle - \langle Q_\alpha(\xi, x_i, t)|\xi(x_i, t) = \eta\rangle = 0 \tag{3.3}$$

The starting point in the derivation is the species transport equation

$$\rho\frac{\partial Y_\alpha}{\partial t} + \rho u_i\frac{\partial Y_\alpha}{\partial x_i} = \frac{\partial}{\partial x_i}\left(\rho D_\alpha\frac{\partial Y_\alpha}{\partial x_i}\right) + \dot{\omega}_\alpha. \tag{3.4}$$

First, Y_α in Eq.(3.4) is substituted by Eq.(3.2). Then the resulting expression is conditionally averaged with respect to η. The final result is given by:

$$\langle\rho|\eta\rangle\frac{\partial Q_\alpha}{\partial t} + \langle\rho|\eta\rangle\langle u_i|\eta\rangle\frac{\partial Q_\alpha}{\partial x_i} = \langle\rho|\eta\rangle\frac{\langle\chi|\eta\rangle}{2}\frac{\partial^2 Q_\alpha}{\partial\eta^2} + e_Q + e_y + \langle\dot{\omega}_\alpha|\eta\rangle, \tag{3.5}$$

where

$$e_Q = \left\langle\left[\frac{\partial}{\partial x_i}\left(\rho D_\alpha\frac{\partial Q_\alpha}{\partial x_i}\right) + \rho D_\alpha\frac{\partial\xi}{\partial x_i}\frac{\partial}{\partial\xi}\left(\frac{\partial Q_\alpha}{\partial x_i}\right) + \frac{\partial Q_\alpha}{\partial\xi}\frac{\partial}{\partial x_i}\left(\rho(D_\alpha - D)\frac{\partial\xi}{\partial x_i}\right)\right]\middle|\eta\right\rangle, \tag{3.6}$$

$$e_y = -\left\langle \left[\rho \frac{\partial y''_\alpha}{\partial t} + \rho u_i \frac{\partial y''_\alpha}{\partial x_i} - \frac{\partial}{\partial x_i}\left(\rho D_\alpha \frac{\partial y''_\alpha}{\partial x_i} \right) \right] \middle| \eta \right\rangle, \tag{3.7}$$

and

$$\chi = 2D_\alpha \left(\frac{\partial \xi}{\partial x_i} \right)^2 \tag{3.8}$$

is the scalar dissipation rate. To be noted that in the equations above, the notation $\langle\, | \xi(x_i, t) = \eta \rangle$ is substituted by $\langle\, | \eta \rangle$ for simplicity. The complete derivation of Eq.(3.5) is available in Appendix A. The terms e_Q (Eq.(3.6)) and e_y (Eq.(3.7)) are in unclosed form. The process of finding adequate closures for those two terms is known as the primary closure hypothesis [8, 63]. Bilger [8] and Klimenko et al. [63] suggest that, given finite Schmidt numbers, all the terms of e_Q (Eq.(3.6)) scale as the inverse of the Reynolds number (Re). Thus, for high Re, these terms can neglected. Consequently,

$$e_Q \approx 0. \tag{3.9}$$

By considering the unconditional form of e_y, it can be shown that the first and third term of Eq.(3.7) are negligible and that e_y may be written as [8, 61, 63]:

$$e_y = -\frac{1}{P(\eta)} \frac{\partial}{\partial x_i} \big(\langle u''_j y''_\alpha | \eta \rangle \langle \rho | \eta \rangle P(\eta) \big). \tag{3.10}$$

The details of the primary closure hypothesis Appendix A. Assuming that the species diffusivities are equal to the molecular diffusivity as in [8], that is $D_\alpha = D$, and introducing the Favre-averaged PDF, $\tilde{P}(\eta)$, which is related to $P(\eta)$ by

$$\langle \rho \rangle \, \tilde{P}(\eta) = \langle \rho |\, \eta \rangle \, P(\eta), \tag{3.11}$$

where $\langle\, \rangle$ denotes the unconditional average, Eq.(3.5) takes the form

$$\frac{\partial Q_\alpha}{\partial t} + \langle u_i | \eta \rangle \frac{\partial Q_\alpha}{\partial x_i} = -\frac{1}{\langle \rho \rangle \tilde{P}(\eta)} \frac{\partial}{\partial x_i} \Big(\langle \rho \rangle \, \langle u''_i y''_\alpha | \eta \rangle \, \tilde{P}(\eta) \Big) + \frac{1}{2} \langle \chi | \eta \rangle \frac{\partial^2 Q_\alpha}{\partial \eta^2} + \frac{\langle \dot{\omega}_\alpha | \eta \rangle}{\langle \rho | \eta \rangle}. \tag{3.12}$$

The first term on the LHS of Eq.(3.12) is the local rate of change of the conditional species mass fraction and the second represents the conditional convective transport. The first term on the RHS is the conditional turbulent flux, the second accounts for micro-mixing and the third is the chemical source.

3.2.2 Conditional Enthalpy and Temperature Equations

The conditional enthalpy equation can be obtained from the enthalpy equation in a similar fashion. If all Lewis numbers are assumed to be equal to unity, and the convective pressure term and dissipation by viscous stress are neglected, Eq.(2.10) takes the form

$$\rho\frac{\partial h}{\partial t}+\rho u_i\frac{\partial h}{\partial x_i}=\frac{\partial}{\partial x_i}\left(\rho D\frac{\partial h}{\partial x_i}\right)+\frac{\partial p}{\partial t}+\dot{q}_{rad}. \tag{3.13}$$

Similar to Eq.(3.2), h is decomposed as

$$h(x_i,t)=Q_h(\xi(x_i,t),x_i,t)+h''(x_i,t), \tag{3.14}$$

such that

$$Q_h(\eta,x_i,t)=\langle h(x_i,t)|\eta\rangle \qquad \text{and} \qquad \langle h''(x_i,t)|\eta\rangle=0. \tag{3.15}$$

Substituting of Eq.(3.14) in Eq.(3.13) and conditionally averaging with respect to η yield:

$$\begin{aligned}\frac{\partial Q_h}{\partial t}+\langle u_i|\,\eta\rangle\,\frac{\partial Q_h}{\partial x_i}=&-\frac{1}{\langle\rho\rangle\,\tilde{P}(\eta)}\frac{\partial}{\partial x_i}\left(\langle\rho\rangle\,\langle u_i''h''|\,\eta\rangle\,\tilde{P}(\eta)\right)+\frac{1}{2}\,\langle\chi|\,\eta\rangle\,\frac{\partial^2 Q_h}{\partial\eta^2}\\&+\frac{1}{\langle\rho|\eta\rangle}\left\langle\frac{\partial p}{\partial t}\middle|\,\eta\right\rangle+\frac{\langle\dot{q}_{rad}|\,\eta\rangle}{\langle\rho|\eta\rangle}.\end{aligned} \tag{3.16}$$

The conditional temperature equation is obtained from Eq.(3.16) by noting that

$$h=\sum_{\alpha=1}^{N_s}h_\alpha Y_\alpha, \tag{3.17}$$

or in conditional form

$$Q_h=\sum_{\alpha=1}^{N_s}\langle h_\alpha|\eta\rangle Q_\alpha, \tag{3.18}$$

where N_s is the total number of species in the mixture. The conditional temperature equation takes the form

$$\begin{aligned}\frac{\partial Q_T}{\partial t}+\langle u_i|\eta\rangle\frac{\partial Q_T}{\partial x_i}=&-\frac{1}{\langle\rho\rangle\tilde{P}(\eta)}\frac{\partial}{\partial x_i}\left(\langle\rho\rangle\langle u_i''T''|\eta\rangle\tilde{P}(\eta)\right)\\&+\frac{1}{2}\langle\chi|\eta\rangle\left\{\frac{\partial^2 Q_T}{\partial\eta^2}+\frac{1}{\langle c_p|\eta\rangle}\left[\frac{\partial\langle c_p|\eta\rangle}{\partial\eta}+\sum_{\alpha=1}^{N_s}\left(\langle c_{p,\alpha}|\eta\rangle\frac{\partial Q_\alpha}{\partial\eta}\right)\right]\frac{\partial Q_T}{\partial\eta}\right\}\\&+\frac{1}{\langle\rho|\eta\rangle\langle c_p|\eta\rangle}\left\langle\frac{\partial p}{\partial t}\middle|\,\eta\right\rangle-\frac{\langle\dot{\omega}_h|\eta\rangle}{\langle\rho|\eta\rangle\langle c_p|\eta\rangle}+\frac{\langle\dot{q}_{rad}|\,\eta\rangle}{\langle\rho|\eta\rangle\langle c_p|\eta\rangle},\end{aligned} \tag{3.19}$$

where

$$Q_T = \frac{Q_h}{\langle c_p|\eta\rangle}, \tag{3.20}$$

and

$$\langle \dot{\omega}_h|\eta\rangle = \sum_{\alpha=1}^{N_s} \langle h_\alpha|\eta\rangle\langle \dot{\omega}_\alpha|\eta\rangle. \tag{3.21}$$

The detailed derivation of Eqs. (3.16) and (3.19) is provided in Appendix A.

In the absence of soot, it is possible to neglect the radiation source term. This assumption applicable to autoignition problems, since the concentration of soot is negligible before ignition takes place. It is well known that the inclusion of this term in the calculations is computationally expensive, thus one advantage of making this assumption is the reduction in the computational cost. As for the pressure work term, although important in engine applications [89], it is neglected in accordance with the assumptions made in the flow field calculations (Chapter 4). Accordingly, Eqs.(3.16) and (3.19) reduce to:

$$\frac{\partial Q_h}{\partial t} + \langle u_i|\,\eta\rangle\,\frac{\partial Q_h}{\partial x_i} = -\frac{1}{\langle\rho\rangle\,\tilde{P}(\eta)}\frac{\partial}{\partial x_i}\left(\langle\rho\rangle\,\langle u_i'' h''|\,\eta\rangle\,\tilde{P}(\eta)\right) + \frac{1}{2}\,\langle\chi|\,\eta\rangle\,\frac{\partial^2 Q_h}{\partial\eta^2}, \tag{3.22}$$

and

$$\begin{aligned}\frac{\partial Q_T}{\partial t} + \langle u_i|\eta\rangle\frac{\partial Q_T}{\partial x_i} &= -\frac{1}{\langle\rho\rangle\tilde{P}(\eta)}\frac{\partial}{\partial x_i}\left(\langle\rho\rangle\langle u_i'' T''|\eta\rangle\tilde{P}(\eta)\right)\\ +\frac{1}{2}\langle\chi|\eta\rangle\Bigg\{\frac{\partial^2 Q_T}{\partial\eta^2} &+ \frac{1}{\langle c_p|\eta\rangle}\left[\frac{\partial\langle c_p|\eta\rangle}{\partial\eta} + \sum_{\alpha=1}^{N_s}\left(\langle c_{p,\alpha}|\eta\rangle\frac{\partial Q_\alpha}{\partial\eta}\right)\right]\frac{\partial Q_T}{\partial\eta}\Bigg\} - \frac{\langle\dot{\omega}_h|\eta\rangle}{\langle\rho|\eta\rangle\langle c_p|\eta\rangle},\end{aligned} \tag{3.23}$$

respectively.

3.3 Submodels for the Unclosed Terms

The terms $\langle u_i'' y_\alpha''|\eta\rangle$, $\langle u_i'' T''|\eta\rangle$, $\tilde{P}(\eta)$, $\langle\chi|\eta\rangle$, $\langle u_i|\eta\rangle$ and $\langle\dot{\omega}_\alpha|\eta\rangle$ need to be modeled in order to obtain full closure for Eqs. (3.12) and (3.23). The following sections address this issue and present possible closures for these terms.

3.3.1 Turbulent Scalar Flux

The turbulent flux terms $\langle u_i'' y_\alpha''|\,\eta\rangle$ and $\langle u_i'' T''|\,\eta\rangle$ are modeled using the gradient diffusion hypothesis. This hypothesis states that, given a conserved scalar ϕ, the scalar flux $\langle \mathbf{u}\phi''\rangle$ is down the mean scalar gradient i.e., in the direction of $-\nabla\langle\phi\rangle$ [99]. Accordingly, there exists a positive scalar D_t designated as the turbulent diffusivity, such that

$$\langle u_i''\phi''\rangle = -D_t \frac{\partial\langle\phi\rangle}{\partial x_i}, \tag{3.24}$$

where

$$D_t = \frac{C_\mu}{\mathrm{Sc}_t}\frac{\tilde{k}^2}{\tilde{\varepsilon}}. \tag{3.25}$$

In Eq.(3.25), $\tilde{k}$ is the turbulent kinetic energy, $\tilde{\varepsilon}$ is the turbulent eddy dissipation, $C_\mu = 0.09$ and Sc_t is the turbulent Schmidt number. In the current study $\mathrm{Sc}_t = 0.9$ is used. The conditional scalar flux is obtained by taking the conditional mean of Eq.(3.24),

$$\langle u_i''\phi''|\eta\rangle = -D_t \frac{\partial\langle\phi|\eta\rangle}{\partial x_i}. \tag{3.26}$$

Accordingly, the turbulent flux terms in Eqs.(3.12) and (3.23) are approximated as:

$$\langle\, u_i'' y_\alpha''|\,\eta\rangle = -D_t \frac{\partial Q_\alpha}{\partial x_i}, \tag{3.27}$$

and

$$\langle\, u_i'' T''|\,\eta\rangle = -D_t \frac{\partial Q_T}{\partial x_i}, \tag{3.28}$$

respectively. Substituting Eq.(3.27) in Eq.(3.12), and Eq.(3.28) in Eq.(3.23), the conditionally averaged species and temperature transport equations take the form:

$$\begin{aligned}\frac{\partial Q_\alpha}{\partial t} + \langle u_i|\eta\rangle\frac{\partial Q_\alpha}{\partial x_i} = \frac{D_t}{\langle\rho\rangle\tilde{P}(\eta)}\frac{\partial\big(\langle\rho\rangle\tilde{P}(\eta)\big)}{\partial x_i}\frac{\partial Q_\alpha}{\partial x_i} + \frac{\partial D_t}{\partial x_i}\frac{\partial Q_\alpha}{\partial x_i} + D_t\frac{\partial^2 Q_\alpha}{\partial x_i^2} \\ +\frac{1}{2}\langle\chi|\eta\rangle\frac{\partial^2 Q_\alpha}{\partial\eta^2} + \frac{\langle\dot{\omega}_\alpha|\eta\rangle}{\langle\rho|\eta\rangle},\end{aligned} \tag{3.29}$$

and

$$\begin{aligned}\frac{\partial Q_T}{\partial t} + \langle u_i|\eta\rangle\frac{\partial Q_T}{\partial x_i} = \frac{D_t}{\langle\rho\rangle\tilde{P}(\eta)}\frac{\partial\big(\langle\rho\rangle\tilde{P}(\eta)\big)}{\partial x_i}\frac{\partial Q_T}{\partial x_i} + \frac{\partial D_t}{\partial x_i}\frac{\partial Q_T}{\partial x_i} + D_t\frac{\partial^2 Q_T}{\partial x_i^2} \\ +\frac{1}{2}\langle\chi|\eta\rangle\left\{\frac{\partial^2 Q_T}{\partial\eta^2} + \frac{1}{\langle c_p|\eta\rangle}\left[\frac{\partial\langle c_p|\eta\rangle}{\partial\eta} + \sum_{\alpha=1}^{N_s}\left(\langle c_{p,\alpha}|\eta\rangle\frac{\partial Q_\alpha}{\partial\eta}\right)\right]\frac{\partial Q_T}{\partial\eta}\right\} - \frac{\langle\dot{\omega}_h|\eta\rangle}{\langle\rho|\eta\rangle\langle c_p|\eta\rangle}\end{aligned} \tag{3.30}$$

respectively.

3.3.2 Presumed Probability Density Function

As stated in section 2.6.4, the RHS terms of the PDF transport equation (Eq.(2.54)) are in unclosed form. Closures for these terms are usually complicated and computationally expensive. To avoid such difficulties, a functional form of the PDF is assumed and used in the calculations. This procedure is known as the presumed PDF approach. The most commonly used form is the β-PDF. Girimaji [37] showed that this form characterizes the evolution of the scalar PDF accurately. The DNS results of Givi et al. [39], Eswaran et al. [27] and Swaminathan et al. [116] support Girimaji's findings.

The Favre-averaged β-PDF is given by:

$$\tilde{P}(x_i, \eta, t) = \frac{\eta^{\beta_1 - 1}(1-\eta)^{\beta_2 - 1}}{B(\beta_1, \beta_2)}. \tag{3.31}$$

The parameters β_1 and β_2 in Eq.(3.31) are space and time dependent. They are related to the Favre-averaged mixture fraction $\tilde{\xi}$ and its variance $\widetilde{\xi''^2}$ by

$$\beta_1 = \tilde{\xi}\gamma, \tag{3.32}$$

and

$$\beta_2 = (1-\tilde{\xi})\gamma, \tag{3.33}$$

where

$$\gamma = \left[\frac{\tilde{\xi}(1-\tilde{\xi})}{\widetilde{\xi''^2}} - 1\right] \geq 0. \tag{3.34}$$

$B(\beta_1, \beta_2)$ in the denominator of Eq.(3.31) is the beta function defined by the integral

$$B(\beta_1, \beta_2) = \int_0^1 \eta^{\beta_1 - 1}(1-\eta)^{\beta_2 - 1} d\eta = \frac{\Gamma(\beta_1)\Gamma(\beta_2)}{\Gamma(\beta_1 + \beta_2)}, \tag{3.35}$$

where Γ is the gamma function. Figure 3.1 shows the evolution of the β-PDF for various combinations of $\tilde{\xi}$ and $\widetilde{\xi''^2}$. Singularities occur at $\eta = 0$ and $\eta = 1$ when $\beta_1 < 1$ and $\beta_2 < 1$, respectively. For example, when $\tilde{\xi} = 0.1$ and $\widetilde{\xi''^2} = 0.023$, $\beta_1 = 0.2913$ and a singularity occurs at $\eta = 0$. Another example is when $\tilde{\xi} = 0.4$ and $\widetilde{\xi''^2} = 0.160$. In this situation,

$\beta_1 = 0.2$ and $\beta_2 = 0.3$ and two singularity are obtained at $\eta = 0$ and $\eta = 1$. The β-PDF is compared to the homogeneous DNS data of Swaminathan et al. [116] in Figure 3.2 for $\tilde{\xi} = 0.5$. The variance is taken from the DNS data and used along with $\tilde{\xi}$ in Eq.(3.31) to construct the PDF as in [81, 97, 116]. The β-PDF shows an excellent agreement with DNS, which validates the choice of this presumed form. An interesting behavior is observed in the limit where $\beta_1 = \beta_2$ and $\beta_1 \to \infty$. Under these conditions, $\tilde{\xi} = 0.5$, $\widetilde{\xi''^2} \to 0$, and the β-PDF approaches a Gaussian (normal) distribution with the same mean and variance [30, 89]. This behavior is shown in Figure 3.3. $\tilde{\xi}$ is fixed at 0.5 and the value of $\widetilde{\xi''^2}$ is gradually decreased. By inspecting the trends in Fig.3.3 (a) to (d), it can be seen that the β-PDF tends to become Gaussian as $\widetilde{\xi''^2} \to 0$.

3.3.3 Conditional Scalar Dissipation Rate

The conditional scalar dissipation rate $\langle \chi | \eta \rangle$ is a quantity that measures the intensity of micro-mixing in mixture fraction space. $\langle \chi | \eta \rangle$ appears in both conditional species continuity and temperature equations (Eqs.(3.29) and (3.30), respectively). Accurate modeling of this quantity is of great importance, especially around stoichiometry where the contribution of the micro-mixing term to the CMC equations is considerable (Chapter 6). Two models are considered in this work: Girimaji's model [38] and the Amplitude Mapping Closure (AMC) [84]. Both models start from the homogeneous PDF transport equation with a double-delta initial distribution (initially unmixed scalars). But in each model the PDF evolves differently, as will be pointed out later. Hence Girimaji's model and the AMC model are only valid for an initially binary mixture in homogeneous turbulence. Nevertheless, they are used when inhomogeneities exist in order to avoid solving PDF transport equation. Devaud et al. [22] proposed a model that performs better in inhomogeneous turbulence.

Girimaji's Model:

The formulation of Girimaji's model [38] is based on the observation that a presumed β-PDF accurately characterizes the evolution of the scalar PDF over all stages of two-scalar, constant-density mixing in statistically stationary, isotropic turbulence [37]. Starting from

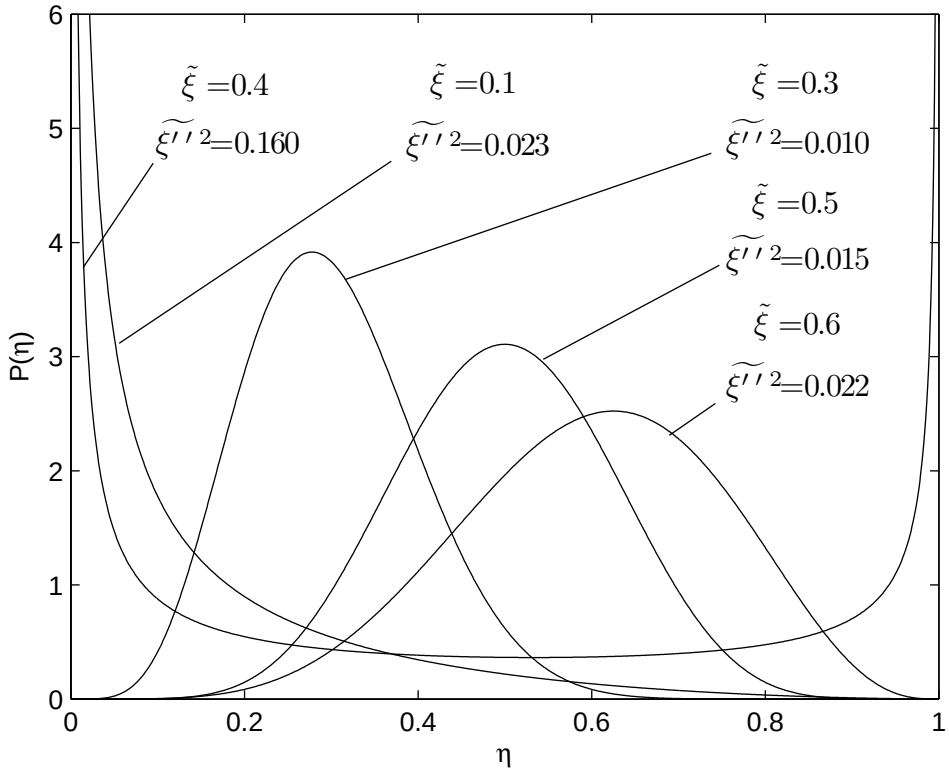

Figure 3.1: Evolution of the β-PDF for various $\tilde{\xi}$ and $\widetilde{\xi''^2}$ combinations.

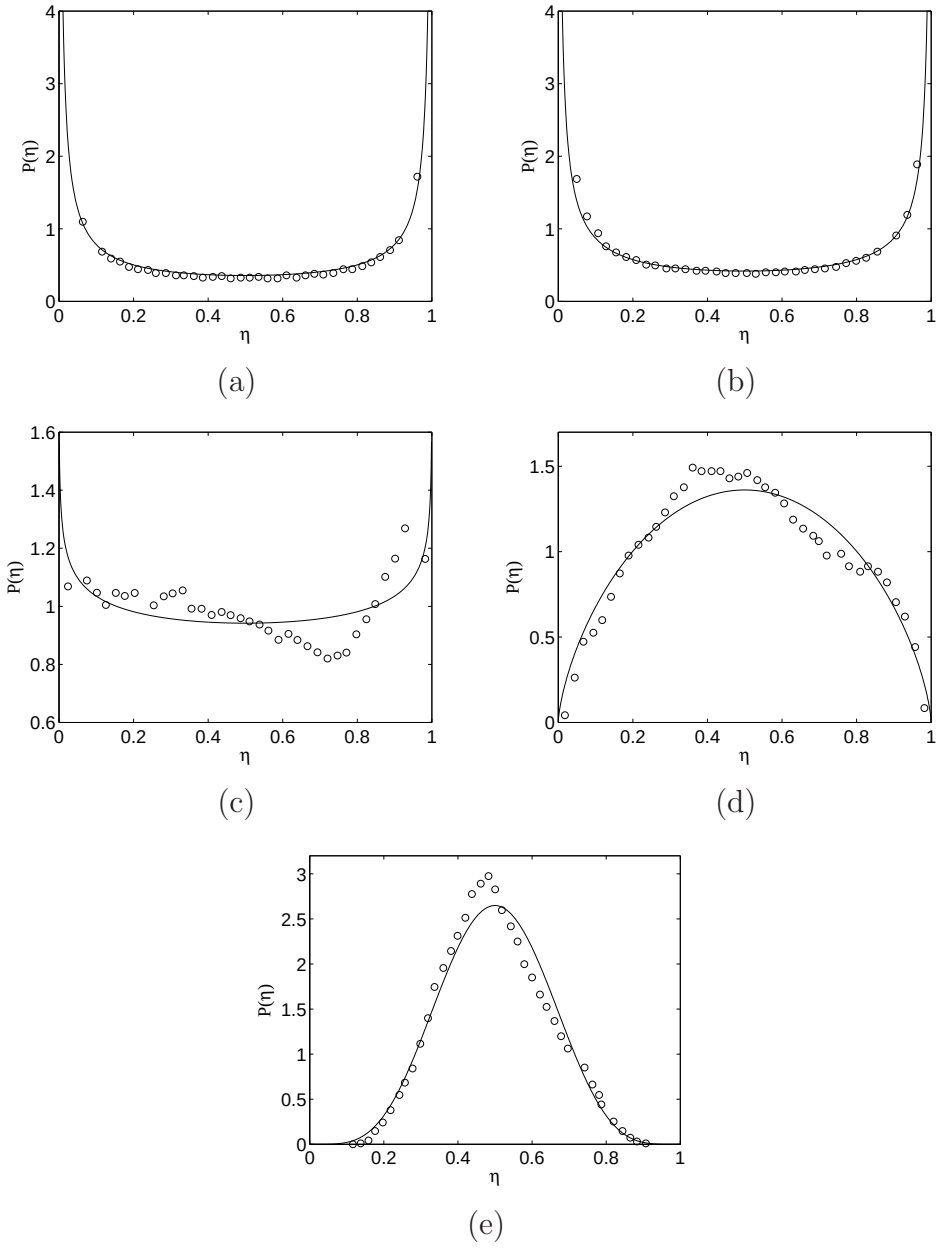

Figure 3.2: Comparison of the β-PDF with the DNS (Swaminathan et al. [116]) for $\tilde{\xi} = 0.5$: β-PDF (——) and DNS (○). (a) $\widetilde{\xi''^2} = 0.1714$, (b) $\widetilde{\xi''^2} = 0.1601$, (c) $\widetilde{\xi''^2} = 0.0888$, (d) $\widetilde{\xi''^2} = 0.0572$, and (e) $\widetilde{\xi''^2} = 0.0204$.

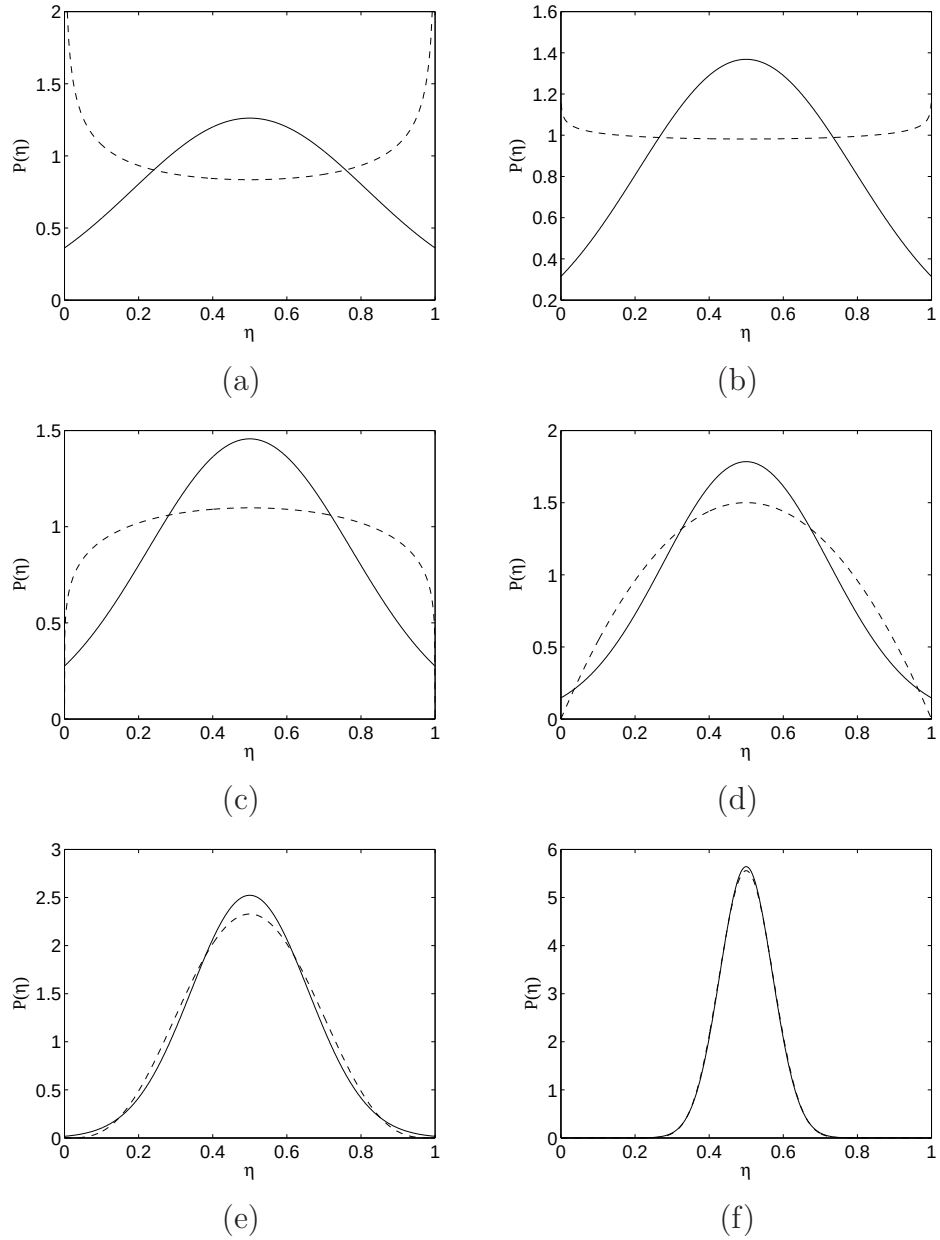

Figure 3.3: Comparison of the β-PDF with the Gaussian distribution for $\tilde{\xi} = 0.5$: Gaussian distribution (——) and β-PDF (- - - -). (a) $\widetilde{\xi''^2} = 0.100$, (b) $\widetilde{\xi''^2} = 0.085$, (c) $\widetilde{\xi''^2} = 0.075$, (d) $\widetilde{\xi''^2} = 0.050$, (e) $\widetilde{\xi''^2} = 0.025$ and (f) $\widetilde{\xi''^2} = 0.005$.

the homogeneous PDF transport equation and integrating over mixture fraction space using the double-delta PDF model as an initial condition, the following equation is obtained for the conditional scalar dissipation rate:

$$\langle \chi|\eta\rangle = -2\tilde{\chi}\frac{\tilde{\xi}(1-\tilde{\xi})}{\widetilde{\xi''^2}}\frac{I(\eta)}{\tilde{P}(\eta)}, \tag{3.36}$$

where $\tilde{\chi}$ is the unconditional (Favre-averaged) scalar dissipation rate given by

$$\tilde{\chi} = 2\frac{\tilde{\varepsilon}}{\tilde{k}}\widetilde{\xi''^2}, \tag{3.37}$$

and $I(\eta)$ is an integral expression given by

$$I(\eta) = \int_0^\eta \left\{\tilde{\xi}(\ln\eta' - I_1) + (1-\tilde{\xi})\left[\ln(1-\eta') - I_2\right]\right\}\tilde{P}(\eta')(\eta-\eta')\,d\eta', \tag{3.38}$$

in which

$$I_1 = \int_0^1 \ln\eta\,d\eta, \tag{3.39}$$

and

$$I_2 = \int_0^1 \ln(1-\eta)\,d\eta. \tag{3.40}$$

The integrand in Eqs.(3.39) and (3.40) have singularities at $\eta = 0$ and $\eta = 1$, respectively. The details on the numerical integration are provided in Chapter 5.

Amplitude Mapping Closure (AMC):

The AMC model was introduced by O'Brian et al. [84]. This model also starts from the homogeneous PDF transport equation and uses the mapping closure solution of Gao [36] for the scalar PDF in which the PDF initially has a double-delta distribution and relaxes to a Gaussian distribution. The conditional mean scalar dissipation rate takes the form

$$\langle \chi|\,\eta\rangle = \langle \chi|\xi = 0.5\rangle G(\eta), \tag{3.41}$$

where $G(\eta)$ is a function independent of $\tilde{\xi}$ and $\widetilde{\xi''^2}$. This function is given by:

$$G(\eta) = \exp\left\{-2\left[\mathrm{erf}^{-1}(2\eta-1)\right]^2\right\}, \tag{3.42}$$

Table 3.1: Values of $\widetilde{\xi''^2}$, $\langle\chi|\xi = 0.5\rangle$ and $\tilde{\chi}$ taken from the DNS of Swaminathan et al. [116]. $\xi = 0.5$ for all cases.

$\widetilde{\xi''^2}$	$\langle\chi\|\xi = 0.5\rangle$	$\tilde{\chi}$
0.0888	0.00687	0.00367
0.0572	0.00381	0.00286
0.0373	0.00178	0.00169
0.0163	0.00066	0.00067

where erf^{-1} is the inverse error function. $\mathrm{erf}^{-1}(2\eta - 1)$ is singular at $\eta = 0$ and $\eta = 1$ since $\lim_{x\to-1} \mathrm{erf}^{-1}(x) = -\infty$ and $\lim_{x\to1} \mathrm{erf}^{-1}(x) = +\infty$. However, in Eq.(3.42), those singularities are finally removed by the exponential function, giving $G(0) = G(-1) = 0$. Furthermore $G(\eta)$ has a global maximum at $\eta = 0.5$ where $G(0.5) = 1$.

Since the constant $\langle\chi|\xi = 0.5\rangle$ in Eq.(3.41) is not known unless a DNS database is available, further modeling is required in order to fully close $\langle\chi|\eta\rangle$. This quantity is obtained by integrating Eq.(3.41) weighted by $\tilde{P}(\eta)$ over the mixture fraction space [59]:

$$\langle\chi|\xi = 0.5\rangle = \frac{\int_0^1 \langle\chi|\eta\rangle\tilde{P}(\eta)d\eta}{\int_0^1 G(\eta)\tilde{P}(\eta)d\eta} = \frac{\tilde{\chi}}{\int_0^1 G(\eta)\tilde{P}(\eta)d\eta}, \tag{3.43}$$

where $\tilde{\chi}$ is given in Eq.(3.37). As pointed out in Section 3.3.2, $\tilde{P}(\eta)$ in Eq.(3.43) might be singular at $\eta = 0$ or $\eta = 1$ or both. This numerical issue will be also addressed in Chapter 5.

Validation of the Conditional Scalar Dissipation Rate Models:

The conditional scalar dissipation models are now validated against DNS data. The values of $\tilde{\xi}$, $\widetilde{\xi''^2}$, $\tilde{\chi}$ and $\langle\chi|\xi = 0.5\rangle$ are taken from the homogeneous DNS results of Swaminathan et al. [116] (see Table 3.1) and used in Eqs.(3.36) and (3.41) in order to construct the different $\langle\chi|\eta\rangle$ models as in [81, 38, 97, 116]. In all cases, $\tilde{\xi}$ is equal to 0.5. The results are displayed in Figure 3.4. Both models show very good agreement with the DNS data. Overall, it can be seen that the AMC model is slightly more accurate. However, this model

has some limitations. For instance, it always requires the presence of some unmixed fluid in the mixture. This restriction does not apply to Girimaji's model [63], which makes it more general.

3.3.4 Conditional Velocity

The conditional velocity is evaluated following the linear model developed by Kuznetsov et al. [68]. This model is given by:

$$\langle \tilde{u}_i | \, \eta \rangle = \tilde{u}_i + \frac{\widetilde{u_i'' \xi''}}{\widetilde{\xi''^2}} (\eta - \tilde{\xi}). \tag{3.44}$$

The gradient diffusion hypothesis is used to approximate the turbulent flux term $\widetilde{u_i'' \xi''}$:

$$\widetilde{u_i'' \xi''} = -D_t \frac{\partial \tilde{\xi}}{\partial x_i}, \tag{3.45}$$

Eq.(3.44) is supported by various sets of experimental data summarized by Kuznetsov et al. [68]. However, the measurements performed by Li et al. [72] question the validity of this model. In their experiment, two separated streams of air, one carrying nitric oxide (fuel) and the other having ozone (oxidizer), traverse a turbulence grid (in order to impose homogeneity) before entering a turbulent smog chamber where they mix. The experimental facility is shown in Figure 3.5. The origin of the frame of reference is located at turbulence grid along the centerline. As for the conditional velocity components, $\langle u|\eta \rangle$ is constant and equal to $\tilde{u}$ and $\langle w|\eta \rangle = 0$, while $\langle v|\eta \rangle$ is the only varying component. Further details can be found in [72]. Figure 3.6 shows the distribution of $\langle v|\eta \rangle - \tilde{v}$ plotted against $\eta - \tilde{\xi}$ at $x = 4.8$ m for three values of y/δ, δ being the distance from where $\tilde{\xi}$ is 0.1 to where it is 0.9. The locations y/δ and the corresponding values of $\tilde{\xi}$ and $\widetilde{v''\xi''}/\widetilde{\xi''^2}$ are given in Table 3.2. As reported in [72], the performance of the linear model is satisfactory when $|\eta - \tilde{\xi}|$ is small, and deviations from the linear relationship between $\langle v|\eta \rangle$ and η are observed as $|\eta - \tilde{\xi}|$ becomes large. As shown in Figure 3.6, best agreement is obtained when $|\eta - \tilde{\xi}|$ is in the neighborhood of zero. Furthermore, it is assumed in the derivation of the linear velocity model that the joint PDF between the velocity and ξ is Gaussian [68, 72]. The influence of this assumption is clearly seen in Figure 3.6(b) where $\xi = 0.559$ (recall from Section 3.3.2

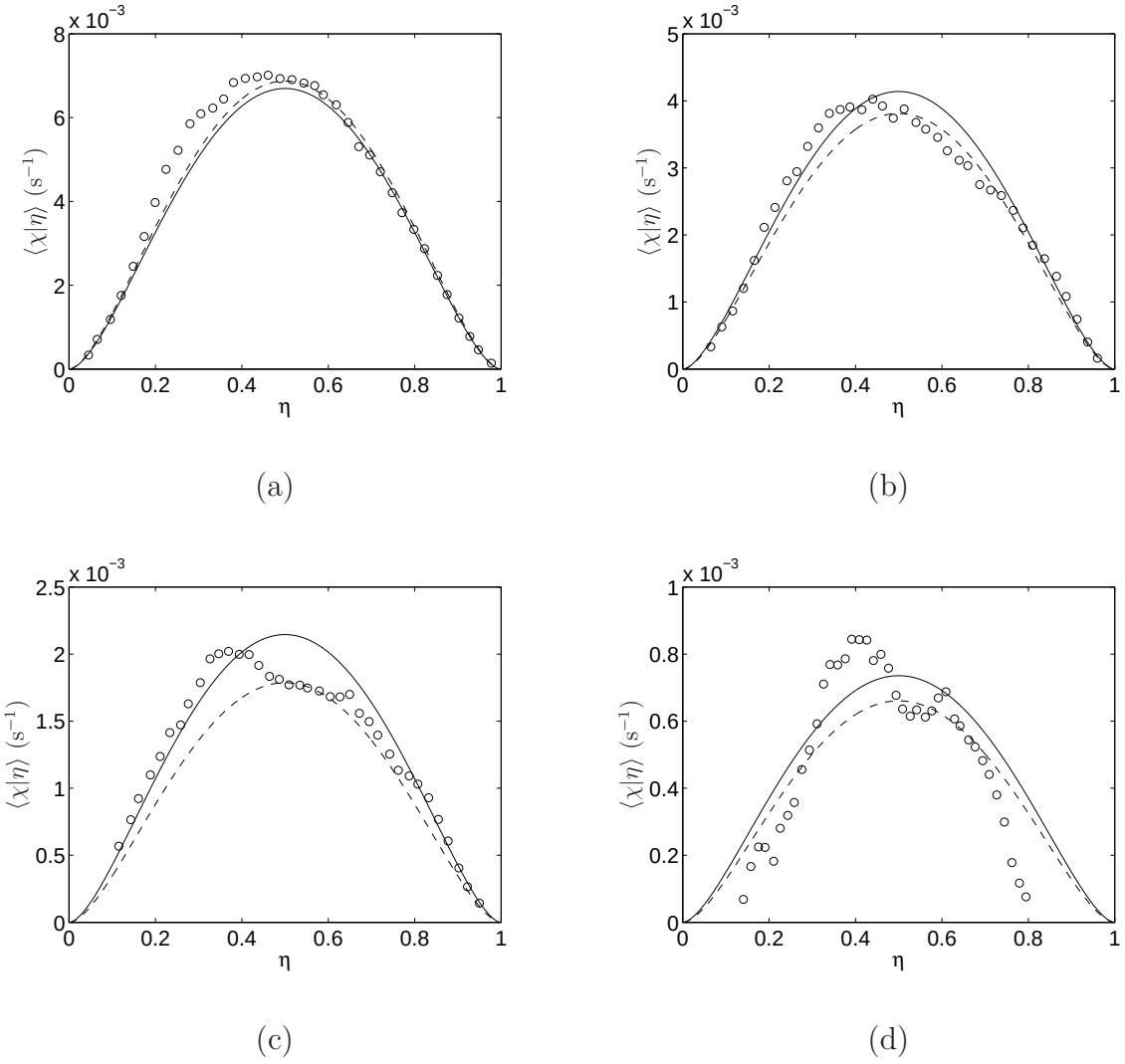

Figure 3.4: Comparison of the different conditional scalar dissipation rate models with the DNS (Swaminathan et al. [116]) for $\tilde{\xi} = 0.5$: Girimaji's model (——), AMC model (- - -), and DNS (∘). (a) $t = 0.75\,\mathrm{s}$, $\widetilde{\xi''^2} = 0.0888$, (b) $t = 1.00\,\mathrm{s}$, $\widetilde{\xi''^2} = 0.0572$, (c) $t = 1.25\,\mathrm{s}$, $\widetilde{\xi''^2} = 0.0373$, and (d) $t = 1.75\,\mathrm{s}$, $\widetilde{\xi''^2} = 0.0163$.

that the PDF tends to become Gaussian when $\xi = 0.5$, if $\widetilde{\xi''^2}$ is small). Good agreement is obtained in this case over a wide range of mixture fraction space. However, this is not always the case for the PDF. On the other hand, the analysis provided by Swaminathan et al. [114] using the DNS data of Baum et al. [4] show that this model performs better than many other models available in the literature such as the gradient models [18] and the PDF model [10]. Despite its weaknesses, this model is widely used due to its simplicity.

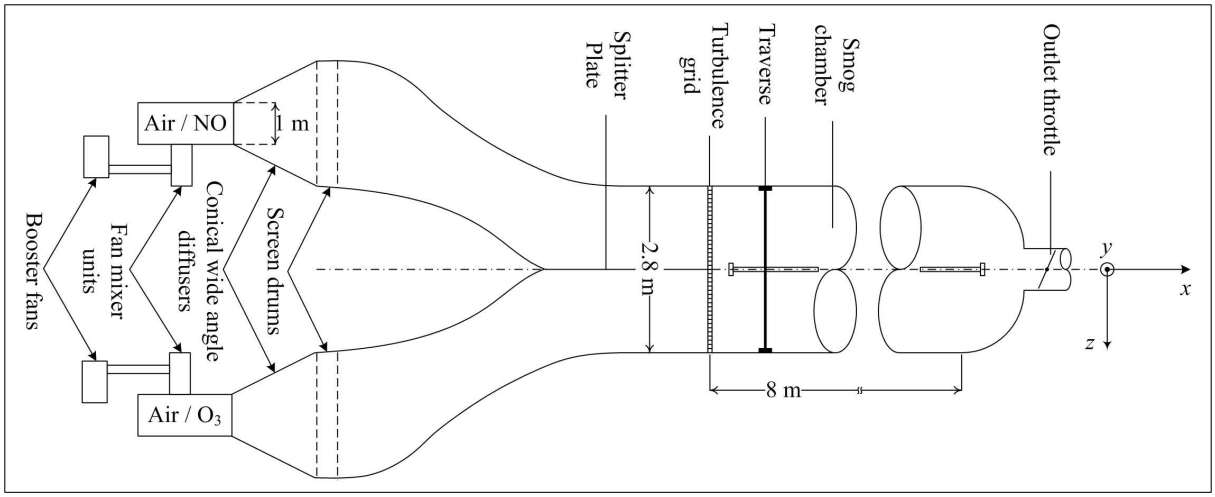

Figure 3.5: Experimental facility for the measurement of the transverse conditional velocity (reproduced from Li et al. [72]).

Table 3.2: y/δ, $\tilde{\xi}$ and $\widetilde{v''\xi''}/\widetilde{\xi''^2}$ at $x = 0.48$ m from the experiments of Li et al. [72].

y/δ	$\tilde{\xi}$	$\widetilde{v''\xi''}/\widetilde{\xi''^2}$
-0.5	0.103	-0.128
0.048	0.559	-0.075
0.41	0.868	-0.102

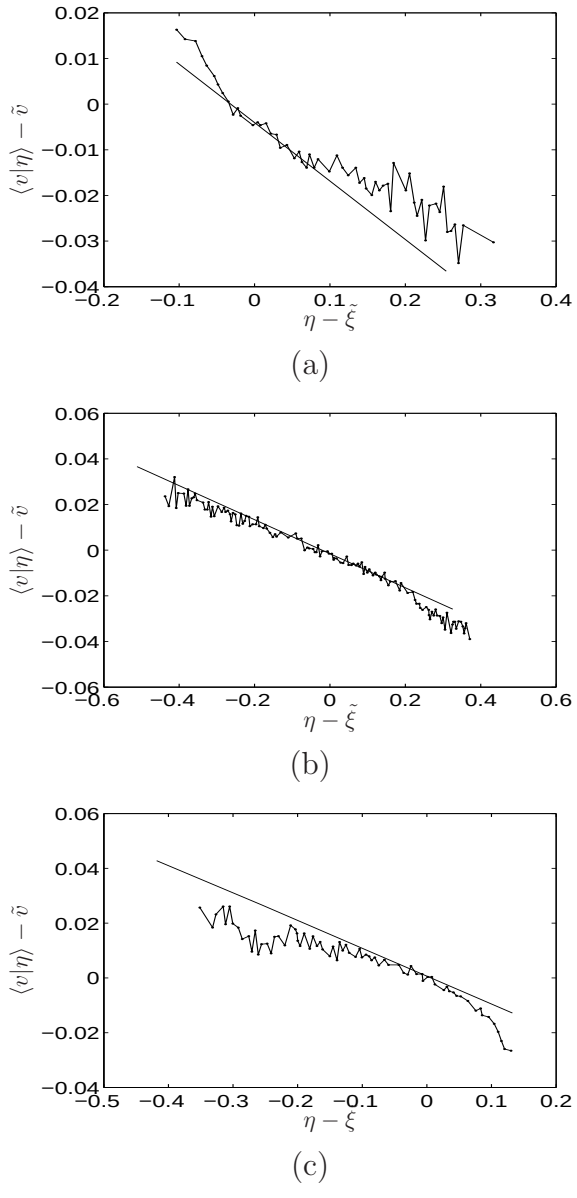

Figure 3.6: Comparison of the linear velocity model with the experimental results of Li et al. [72]: linear model (——) and experiments (-·-·-). (a) $y/\delta = -0.5$, (b) $y/\delta = 0.048$, and (c) $y/\delta = 0.41$

3.3.5 Chemical Source Term

As discussed in Section 2.5.2, the chemical source term is non-linear function of the density, the temperature and the species concentrations:

$$\dot{\omega} = \dot{\omega}\left(\rho, T, Y_1, Y_2, \ldots, Y_{N_s}\right) = \dot{\omega}\left(\rho, T, \mathbf{Y}\right), \tag{3.46}$$

where $\mathbf{Y} = Y_1, Y_2, \ldots, Y_{N_s}$. Consequently, the unconditional average of Eq.(3.46), $\langle\dot{\omega}\rangle$, cannot be expressed as a linear function of the unconditional averages $\langle\rho\rangle$, $\langle T\rangle$, and $\langle\mathbf{Y}\rangle$ [63], i.e.,

$$\langle\dot{\omega}\left(\rho, T, \mathbf{Y}\right)\rangle \neq \dot{\omega}\left(\langle\rho\rangle, \langle T\rangle, \langle\mathbf{Y}\rangle\right). \tag{3.47}$$

In CMC, the quantity of interest is the conditional average of the chemical source term, $\langle\dot{\omega}\left(\rho, T, \mathbf{Y}\right)|\eta\rangle$. Like the unconditional average, this quantity is still problematic. However, Klimenko et al. [63] state that conditional averages contain much more details on the scalar field than their unconditional counterparts. Furthermore, they note that conditional fluctuations are of smaller order than unconditional fluctuations in turbulent shear flows. This observation is also supported by the experimental findings of Masri et al. [77]. Thus, in such flows, the inequalities

$$\rho'' \ll \rho', \tag{3.48}$$

$$T'' \ll T', \tag{3.49}$$

and

$$\mathbf{y}'' \ll \mathbf{y}' \tag{3.50}$$

are valid. If the conditional fluctuations are considered to be negligible, it is possible to model $\langle\dot{\omega}\left(\rho, T, \mathbf{Y}\right)|\eta\rangle$ as a function of $\langle\rho|\eta\rangle$, $\langle T|\eta\rangle$ and $\langle\mathbf{Y}|\eta\rangle$ as shown in Eq.(3.51):

$$\begin{aligned}
\langle\dot{\omega}\left(\rho, T, \mathbf{Y}\right)|\eta\rangle &= \langle\dot{\omega}\left(\langle\rho|\eta\rangle + \rho'', \langle T|\eta\rangle + T'', \langle\mathbf{Y}|\eta\rangle + \mathbf{y}''\right)|\eta\rangle \\
&\approx \langle\dot{\omega}\left(\langle\rho|\eta\rangle, \langle T|\eta\rangle, \langle\mathbf{Y}|\eta\rangle\right)|\eta\rangle \\
&= \dot{\omega}\left(\langle\rho|\eta\rangle, \langle T|\eta\rangle, \langle\mathbf{Y}|\eta\rangle\right) \\
&= \dot{\omega}\left(\langle\rho|\eta\rangle, Q_T, \mathbf{Q}\right),
\end{aligned} \tag{3.51}$$

where $\mathbf{Q} = \langle\mathbf{Y}|\eta\rangle$. The closure provided in Eq.(3.51) is first order accurate. Klimenko et al. [63] considered the conditional average of the second-order taylor series expansion of

the reactions rate of a simple one-step irreversible chemical reaction of the form

$$\mathrm{A} + \mathrm{B} \rightarrow \mathrm{P}, \tag{3.52}$$

for which $\dot{\omega}$ is given by

$$\dot{\omega} = \rho k(T) Y_A Y_B \quad \text{with} \quad k(T) = A_0 T^b \exp\left(-\frac{T_a}{T}\right) \tag{3.53}$$

The resulting expression takes the form:

$$\begin{aligned}\langle \dot{\omega}|\eta\rangle =& \langle\rho|\eta\rangle k(Q_T) Q_A Q_B \left[1 + \frac{\langle y_A'' y_B''|\eta\rangle}{Q_A Q_B} + \left(b + \frac{T_a}{Q_T}\right)\left(\frac{\langle y_A'' T''|\eta\rangle}{Q_A Q_T} + \frac{\langle y_B'' T''|\eta\rangle}{Q_B Q_T}\right)\right. \\ &\left. + \frac{1}{2}\left(b(b-1) + \frac{2(b-1)T_a}{Q_T} + \frac{T_a^2}{Q_T^2}\right)\frac{\langle T''^2|\eta\rangle}{Q_T^2}\right]\end{aligned} \tag{3.54}$$

It can be seen from Eq.(3.54) that the error involved in the first-order closure is small if the conditional variances of the species mass fractions and temperature are small compared with the square of their conditional means. On the other hand, Mastorakos et al. [79] argue that temperature fluctuations drive the autoignition process, and thus should not be neglected. Furthermore, Swaminathan et al. [116] make an important observation regarding mixing models. Their DNS study suggests that the first order closure for the chemical source term predicts slower reaction rates when the mixing field is modeled using Girimaji's model [38]. Much better predictions are obtained when the AMC model [84] is employed.

3.4 Conclusions

This chapter presented the first-order CMC method. The decomposition approach and the primary closure hypothesis were used to derive the conditional species, enthalpy and temperature transport equations. Submodels for the unclosed conditional terms were discussed. The gradient diffusion hypothesis was used to close the turbulent flux terms. Based on DNS data, the presumed β-PDF was found to be an adequate alternative for solving the PDF transport equation. The behavior of the β-PDF was also studied by inspecting different combinations of its parameters. Two conditional scalar dissipation models were

presented: Girimaji's model and the AMC model. Both models show good agreement with DNS, with the AMC model being slightly more accurate. As for the conditional velocity, the linear model was discussed and its limitations were pointed out. Finally, the first-order closure for the chemical source term was discussed.

The next chapter describes the autoignition experiments and focuses on the turbulent velocity and mixing fields calculations.

Chapter 4

Frozen Mixing Calculations and Validation of the CFD Code

This chapter focuses on the turbulent flow field calculations. The frozen mixing assumption is adopted to perform the turbulent flow field and the CMC calculations separately. As a first step, the velocity and mixing fields computations are carried out in order to prepare transient libraries that contain all the information required for the CMC calculations. The transient injection of a low-temperature methane jet into a shock tube filled with high-pressure and high-temperature air is reproduced numerically. The experimental conditions and the computational details are provided in detail. The predicted jet penetration in the shock tube is compared to the penetration length correlation derived by Ouellette [86] for turbulent round jets. The k-ε model constant $C_{\varepsilon 1}$ is modified such that best agreement is achieved with this correlation. The test case where air temperature is equal to 1300 K is considered for demonstration.

4.1 Shock Tube Experiments

The current numerical study focuses on the experimental measurements conducted by Sullivan et al. [113]. In these experiments, a shock tube facility was used to investigate the autoignition delay of methane and methane-ethane mixtures under engine-relevant conditions and to monitor the variability of nitrogen oxides in the combustion products.

The facility is shown in Figure 4.1. The shock tube has a circular cross-section with an inner diameter of 5.9 cm. Its total length is 7.90 m, the driver and driven sections being 3.11 m and 4.79 m long, respectively. An electronically controlled injector is used to inject the gaseous fuel into the preheated and compressed air. The injector has one central hole of either 1.1 mm or 0.275 mm diameter and it is mounted at the center of the endplate of the shock tube in order to inject the fuel along the centerline, as shown Figure 4.1. To provide optical access to the experimental area, a stainless steel section equipped with three windows is attached to the end of the driven section. A high-speed digital camera (31000 frames per second) is used to capture the location of the initial ignition kernel. The location of this kernel is identified by the appearance of a non-contiguous flame region that is able to develop into a fully fledged jet flame. Accordingly, ignition delay is defined as the time from the start of the injection of the fuel to the appearance of the ignition kernel [47]. Further details on the experimental setup can be found in references [47, 112, 113].

In all test cases, the air pressure inside the test section and the injected fuel temperature were fixed at 30 bar and 300 K, respectively, while the air temperature and the injection pressure were varied over a wide range of values. The measurements of interest correspond

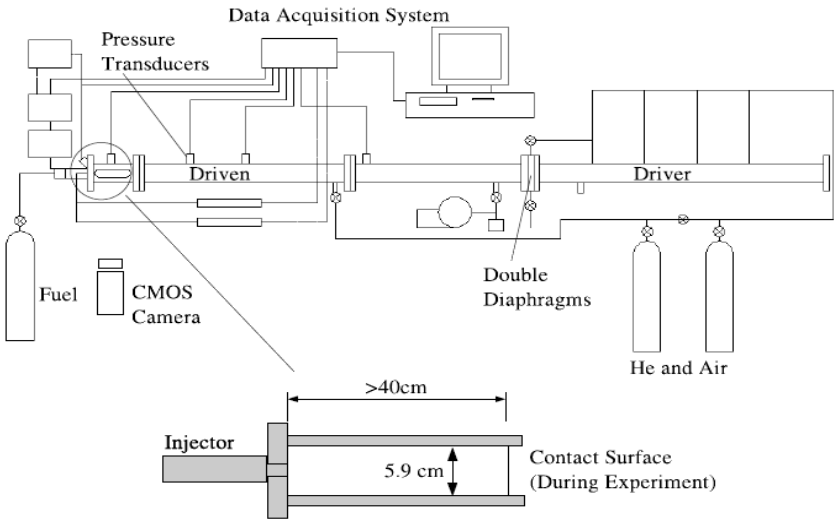

Figure 4.1: Shock tube facility (taken from Huang [47]).

to the test case where 99.97% pure methane was injected at a pressure of 75 bar through the 1.1 mm central hole for a duration of 1.5 ms, the initial air temperature inside the test section being varied between 1150 and 1400 K (series I in reference [113]). A total of 28 measurements were performed over this temperature range. The experimental conditions are summarized in Table 4.1.

Table 4.1: Experimental conditions (series I in reference [113]). d is the injector hole diameter, t_i is the injection duration, P_i is the injection pressure, P_{air} is the initial air pressure, T_f is the fuel temperature, and T_{air} is the initial air temperature.

Runs	d (mm)	t_i (ms)	P_i (bar)	P_{air} (bar)	T_f (K)	T_{air} (K)
28	1.1	1.5	75	30	300	1150-1400

4.2 Decoupling of the Turbulent Flow Field and the CMC Calculations

In this study, the turbulent flow field and the CMC calculations are decoupled, i.e. the turbulent flow field calculations are used as input to the CMC routines. This is a reasonable approximation since the reaction rates are slow before ignition takes place, which results in very small density and temperature variations. Consequently, it is possible to neglect these variations in the flow field by making the assumptions of frozen (cold) mixing, thus allowing decoupling between the flow field and the CMC calculations [76]. It should be noted that the density and temperature changes become larger in the vicinity of ignition and later when a flame starts to propagate. The decoupling technique is therefore inapplicable in presence of flames.

First, frozen mixing calculations are performed and two-dimensional transient libraries containing the quantities of interest such as $\tilde{\xi}$, $\widetilde{\xi''^2}$, $\partial\tilde{\xi}/\partial x$, $\tilde{u}_x$, $\tilde{k}$ and $\tilde{\varepsilon}$ are built at a specific time interval. This interval represents the time step used in the CMC calculations. These quantities are then used to compute the turbulent diffusivity, the probability density function, and the conditional axial velocity and scalar dissipation rate at every point in

both physical and mixture fraction spaces. This is followed by cross-stream averaging of the terms appearing inside $\{\}_{R^+}$ in the conditional species and temperature transport equations (Eqs.(5.4) and (5.5)). The cross-stream averaged quantities are then progressively passed to the CMC routines as the calculations advance in time. The process is shown in Figure 4.2. A similar procedure was successfully applied by Markides et al. [76] to the prediction of autoignition of n-heptane plumes and by Devaud et al. [23] to lifted turbulent hydrogen-air flames.

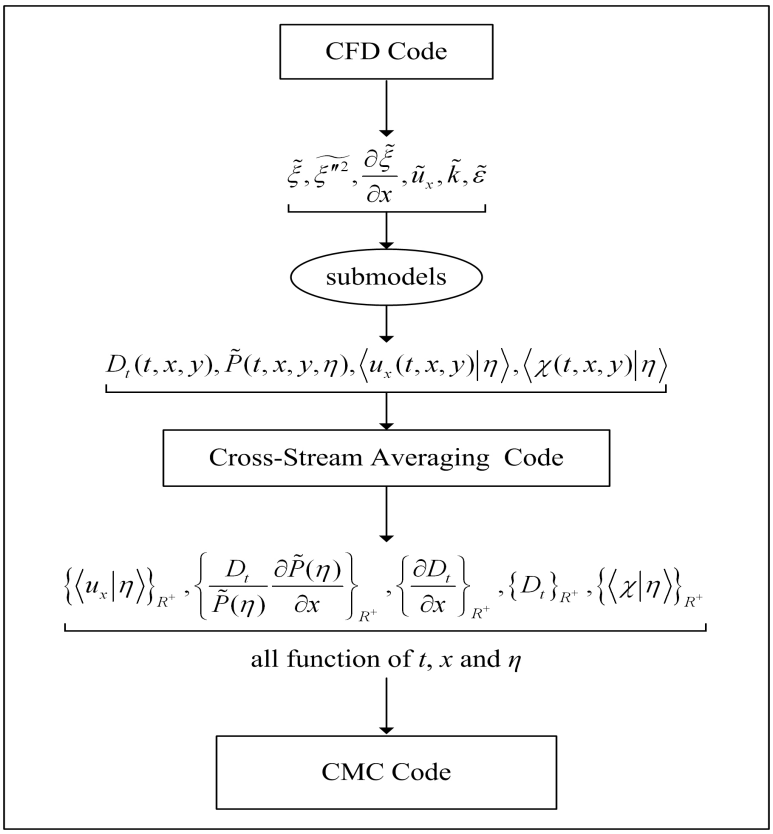

Figure 4.2: Computational domain of the shock tube.

4.3 Flow Field

The axisymmetric computational domain has dimensions of 15 cm (length) × 2.9 cm (radius) and represents one half of the experimental shock tube test section due to symmetry. ANSYS CFX 10.0 [2] is used to perform the turbulent velocity and mixing field calculations based on a pseudo-3D unstructured mesh (the terminology pseudo-3D corresponds to a 3D mesh having only one control volume in the θ-direction). For this purpose, a 5° wedge cutting through the centerline of the shock tube is chosen, as shown in Figure 4.3. The mesh is constructed using ANSYS ICEM CFD [3] and consists of 481 × 103 unevenly-spaced nodes in the axial and radial directions, respectively. This configuration results in a total of 48,960 control volumes. The methane inlet is resolved with 5 nodes (4 control volumes) and the mesh density is highest in the inlet area in order to accurately capture the sharp gradients. Away from this area, the mesh becomes progressively coarser, in both axial and radial directions. The maximum mesh spacing in the domain does not exceed the inlet radius.

Following the experimental conditions [113], a fixed mass flow rate of 4.875×10^{-3} kg/s

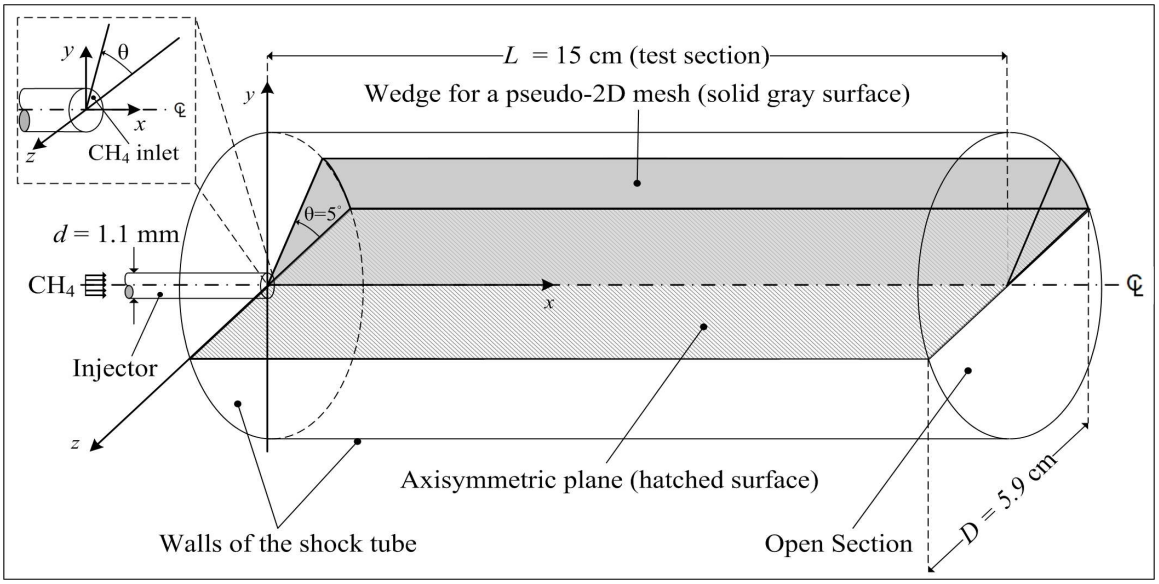

Figure 4.3: Computational domain of the shock tube.

(6.771^{-5} kg/s for the 5° wedge) and a temperature of 300 K are set at the inlet. Experiments also indicated that the flow entering the shock tube test section was subsonic implying that the methane jet should have a high static pressure based on a polytropic gas expansion [48]. In the present simulations, it was not possible to specify both the mass flow rate and the pressure simultaneously at the inlet. Thus, the methane inlet pressure is set to the initial air pressure in the shock tube. This approximation is reasonable for most parts of the flow field since large pressure gradients are expected to occur only very close to the fuel inlet. At the far end of the computational domain, an opening boundary condition is used in order to account for any amount of fluid that might reenter the domain. The turbulence intensity is set to 5% at both the inlet and the opening. The walls of the shock tube are considered to be smooth and adiabatic, and no-slip conditions apply. The front and back surfaces of the wedge are treated as symmetry planes (axisymmetric configuration). The computational domain is initialized with pure air at a given temperature between 1200 K to 1400 K and at a static pressure of 30 bar. The boundary and initial conditions are shown in Figure 4.4.

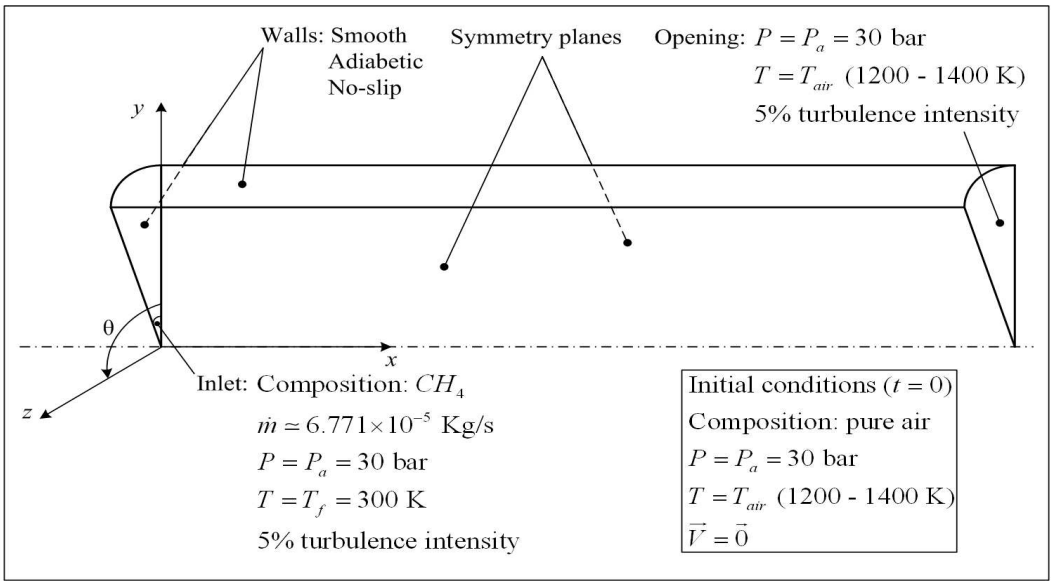

Figure 4.4: Boundary and initial conditions.

As in the experiments [113], the injection duration of methane is 1.5 ms. At high

temperatures, ignition occurs during the injection period. However, at relatively lower temperatures, ignition might take place after injection is terminated. In such a situation, the inlet boundary condition is replaced by a wall in order to simulate the shut-off of the injector. The simulation is then restarted and the working fluids are allowed to mix for a desired duration that is long enough to insure the ignition of the mixture. Shortly after the shut-off, the methane jet becomes detached from its source. The effect of advection decreases gradually and diffusion starts to dominate.

The k-ε model is used to perform the turbulent flow field calculations (see Eqs.(2.25) and (2.27)). An external subroutine is implemented and added to ANSYS CFX in order to solve the mixture fraction variance equation (Eq.(2.47)). The second-order high resolution scheme is used for the discretization of the advection terms. The transient terms are discretized using the second-order backward Euler scheme (implicit). Convergence is achieved based on a maximum residual criterion. In all simulations, the maximum residual target is set to 10^{-4}. An adaptive time step is employed with a minimum of 10^{-10} s and a maximum of 10^{-6} s. Adaption is based on the Courant number.

4.4 Validation of the Flow Field Calculations

4.4.1 Penetration Length Correlation

In the absence of experimental data, the predicted transient jet penetration length is compared with a correlation developed by Hill et al. [44]. The formulation of this correlation is based on the entrainment measurements performed by Ricou et al. [103] and the vortex quasi-steady jet model proposed by Turner [120]. Ricou et al. [103] measured the entrainment by a gas injected into a reservoir containing another stagnant gas, e.g. a gaseous fuel injected into a combustion chamber filled with air. They correlated the mass flow rate, the jet momentum, the axial distance (from the origin of the axisymmetric jet) and air density, regardless of the density of the injected gas. Turner [120] suggested that a transient jet consists of a steady-state region headed by spherical vortex that merges gradually with the jet behind it. This configuration is shown in Figure 4.5. If the flow at the exit of the nozzle is steady, the vortex is supplied with mass an momentum by the jet on a continuous

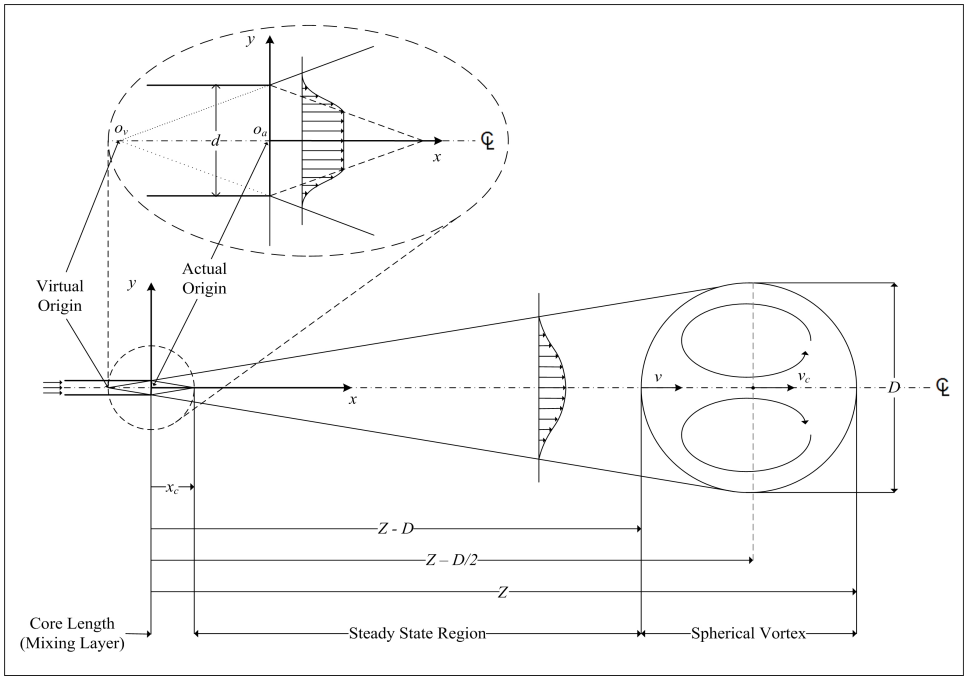

Figure 4.5: Turner quasi-steady jet model (partially reproduced from references [86, 120]).

basis [44]. Based on the above formulations and observations, Hill et al. [44] derived the following correlation for self-similar transient jet:

$$\frac{Z}{d\sqrt{\rho_n/\rho_c}} = \Gamma \left(\frac{\pi}{4}\right)^{1/4} \left(\frac{U_n t}{d\sqrt{\rho_n/\rho_c}}\right)^{1/2}, \tag{4.1}$$

where Z is the penetration length defined as the distance from the origin to the tip of the vortex (see Figure 4.5), d is the nozzle diameter, $\Gamma = 3.0 \pm 0.1$, U_n is the velocity of the jet at the nozzle, t is the time measured from the beginning of injection, and ρ_n and ρ_c are the densities at the nozzle and inside the chamber, respectively.

4.4.2 Penetration Criteria

Computationally, several criteria can be used in order to determine the penetration length. For instance, the penetration of the jet can be defined as the distance along the jet centerline extending from the origin to the point where either the mixture fraction or the velocity

of the jet becomes zero. Both criteria were tested and the differences were shown to be negligible. The mixture fraction criterion is used in this study.

4.4.3 Modification of the k-ε Model

It was previously mentioned in Section 2.4.1 that the standard k-ε model overpredicts the spreading rate when applied to a round jet [99]. A direct consequence is the underprediction of the jet penetration length. The temporal variation of the penetration length is shown in Figure 4.6 (solid red line with square markers) along with Z from Eq.(4.1) (solid black line) for $T_a = 1300$ K. The corresponding relative error is displayed in Figure 4.7. The maximum relative error in this case is around 18%. One possible way to decrease the magnitude of the errors is to modify the model constants. Table 4.2 summarizes some of the suggested $C_{\varepsilon 1}$ and $C_{\varepsilon 2}$ values that have been previously used for round jets. It can be seen that it is a common practice to change the value of $C_{\varepsilon 1}$, while leaving $C_{\varepsilon 2}$ unchanged. This procedure was followed in this study. The $C_{\varepsilon 1}$ values suggested by Pope [95] and Ouellette et al. [86] along with other values were tested. Figure 4.6 shows the time variation of the penetration length using the different $C_{\varepsilon 1}$ values (with $T_a = 1300$ K). The corresponding relative error variation is plotted in Figure 4.7. Best agreement with the penetration correlation (within $\pm 7\%$) is obtained when $C_{\varepsilon 1} = 1.535$. Lower values such as 1.52 perform better at early simulations times, but show a poor performance at later times. Higher values such as 1.55 and 1.56 show an opposite trend. Overall, $C_{\varepsilon 1} = 1.535$ yields an intermediate behavior in terms of error magnitude at all simulation times, and thus it is used throughout all the simulations.

Table 4.2: $C_{\varepsilon 1}$ and $C_{\varepsilon 2}$ model constants used for turbulent round jets.

	$C_{\varepsilon 1}$	$C_{\varepsilon 2}$
Jones et al. [51] (standard constants)	1.44	1.92
Pope [95]	1.60	1.92
Gaillard [35]	1.52	1.89
Ouellette et al. [86]	1.50 and 1.52	1.92
This study	1.535	1.92

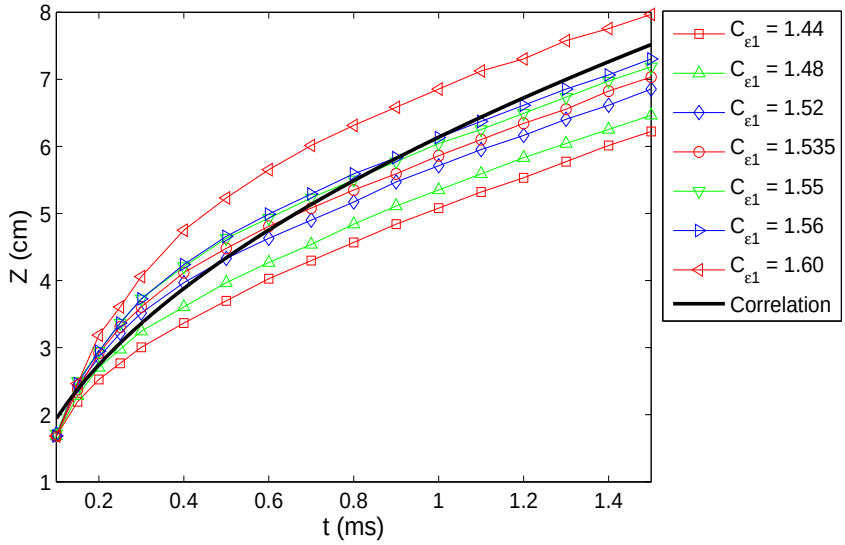

Figure 4.6: Temporal variation of the predicted penetration length when $T_{air} = 1300$ K. Also shown is the penetration length computed from the correlation given by Eq.(4.1)

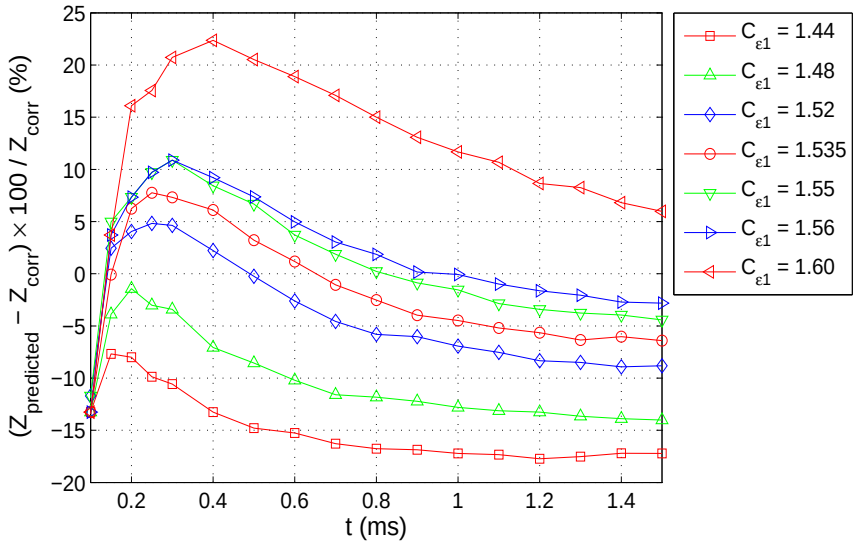

Figure 4.7: Relative error between the predicted penetration length and Eq.(4.1). The relative error is defined as $(Z_{predicted} - Z_{corr}) \times 100/Z_{corr}$ (%)

4.4.4 Frozen Mixing Test Case

For illustration, the test case where $T_a = 1300$ K is considered. Figures 4.8, 4.9, 4.10 and 4.11 display the time variation of the radial distribution of the Favre-averaged mixture fraction ($\tilde{\xi}$), mixture fraction variance ($\widetilde{\xi''^2}$), temperature ($\widetilde{T}$ (K)) and velocity magnitude ($\widetilde{V}$ (m/s)) at various $x-$locations along the jet centerline. Some contours are also shown in Figure 4.12. As a general observation, it can be seen that quasi-steady state is reached close to the inlet ($0\,\text{cm} \leq x \leq 2.0\,\text{cm}$) within 0.30 ms, while downstream profiles require a longer duration to reach this state. The steady state and spherical vortex regions described by Turner [120] (Section 4.4) can be identified by inspecting the mixture fraction in Figures 4.8 and 4.12(a) and the velocity in Figures 4.11 and 4.12(d). The vortex starts to develop shortly after the beginning of injection and it is continuously supplied with mass an momentum by the jet behind it, which in turn keeps increasing in width. After 0.60 ms, the width of the jet becomes almost constant for $x \lesssim 3.0$ cm. Beyond this location, the width and the penetration length of the jet, and the size of the vortex keep on increasing with time. Figures 4.9 and 4.12(b) show that the variance of the mixture fraction is highest in the inlet area ($0\,\text{cm} \leq x \leq 2.0\,\text{cm}$). This can be explained by the presence of sharp mixture fraction gradients. As can be seen in Figures 4.10 and 4.12(c), the temperature decreases gradually from the initial value of $T_{air} = 1300$ K. Since the temperature of methane is much lower than the temperature of air (300 K compared to 1300 K), $\widetilde{T}$ in the jet region is expected to be intermediate between the two. In fact, $\widetilde{T}$ is closer to the methane temperature in the inlet area, and tends towards the air temperature away from it. This can be seen by noting the temperature plateaus in Figure 4.10 where $\widetilde{T}$ assumes the value of the air temperature. The width of the plateaus depends on the width of the jet. Thus, wide plateaus are obtained in the inlet area due to the narrowness of the jet, and an opposite behavior is observed downstream. Finally, the Favre-averaged velocity profiles displayed in Figures 4.11 and 4.12(d) follow the same trends as the the Favre-averaged mixture fraction. The velocity at the inlet is approximately equal to 278 m/s (not shown in Figure 4.11). The Reynolds number based on the inlet diameter is equal to 5.383×10^5.

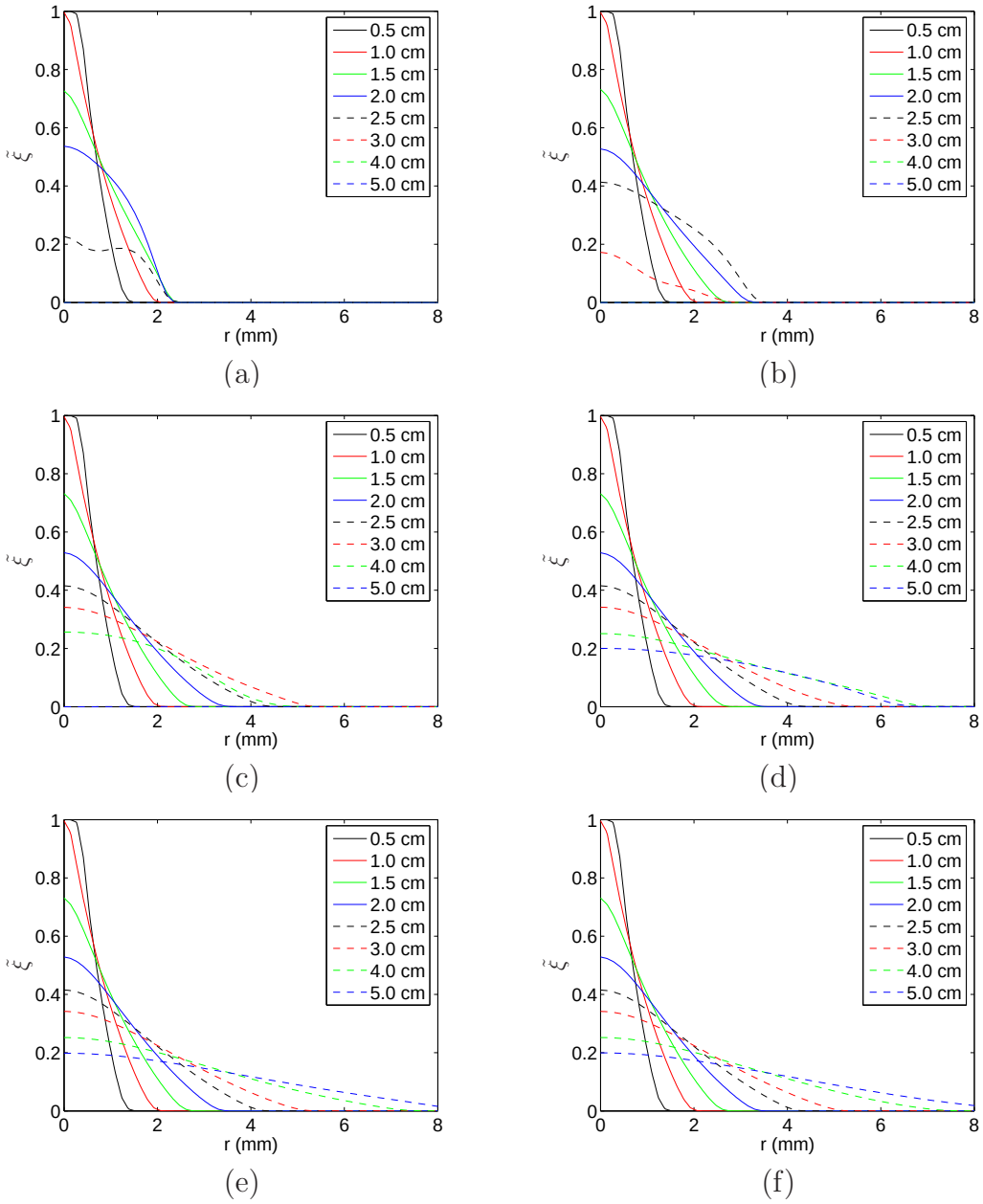

Figure 4.8: Radial variation of the Favre-averaged mixture fraction at different locations along the jet centerline when $T_{air} = 1300$ K: (a) $t = 0.20$ ms, (b) $t = 0.30$ ms,(c) $t = 0.60$ ms, (d) $t = 0.90$ ms, (e) $t = 1.20$ ms, and (f) $t = 1.50$ ms.

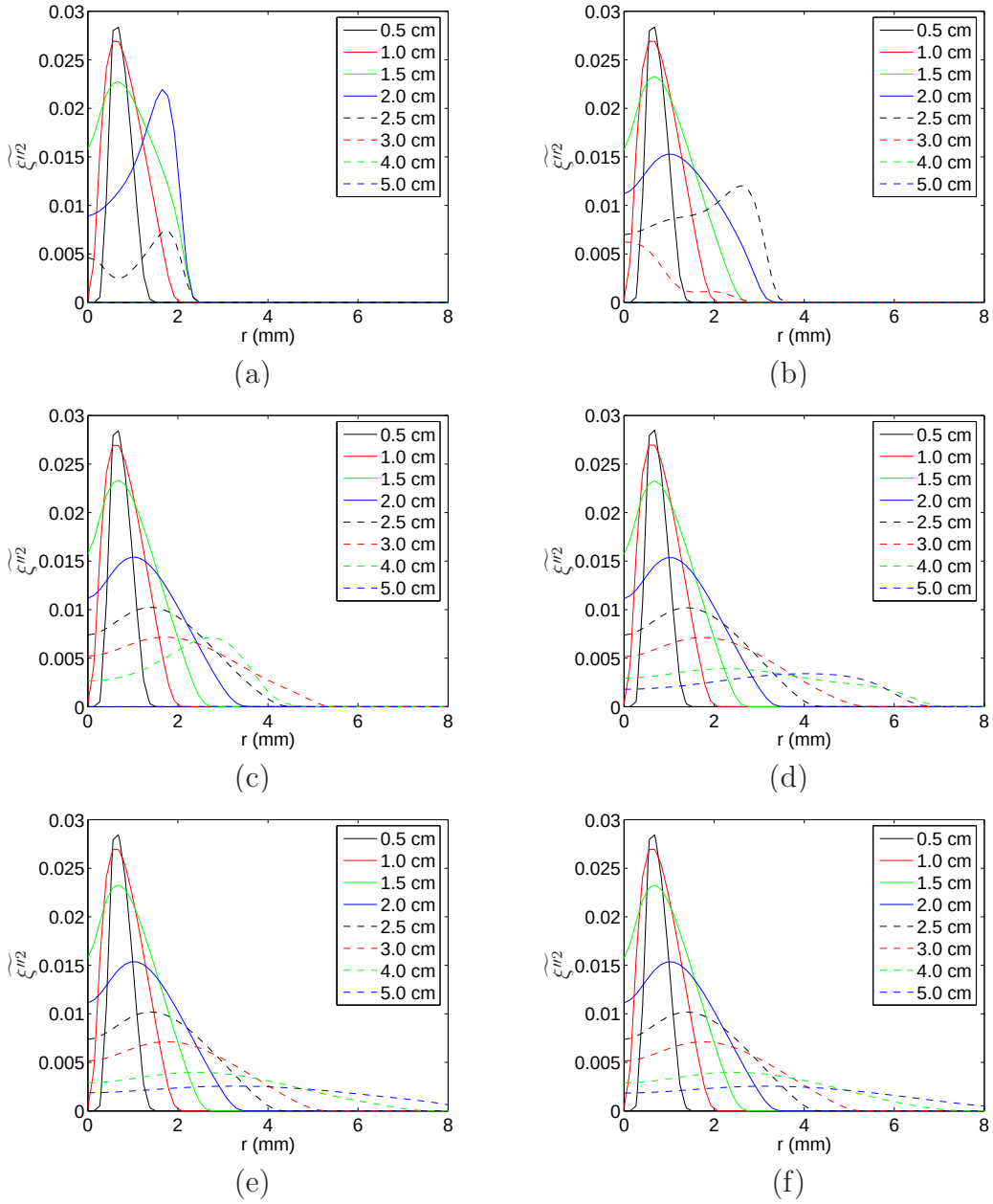

Figure 4.9: Radial variation of the Favre-averaged mixture fraction variance at different locations along the jet centerline when $T_{air} = 1300$ K: a) $t = 0.20$ ms, (b) $t = 0.30$ ms,(c) $t = 0.60$ ms, (d) $t = 0.90$ ms, (e) $t = 1.20$ ms, and (f) $t = 1.50$ ms.

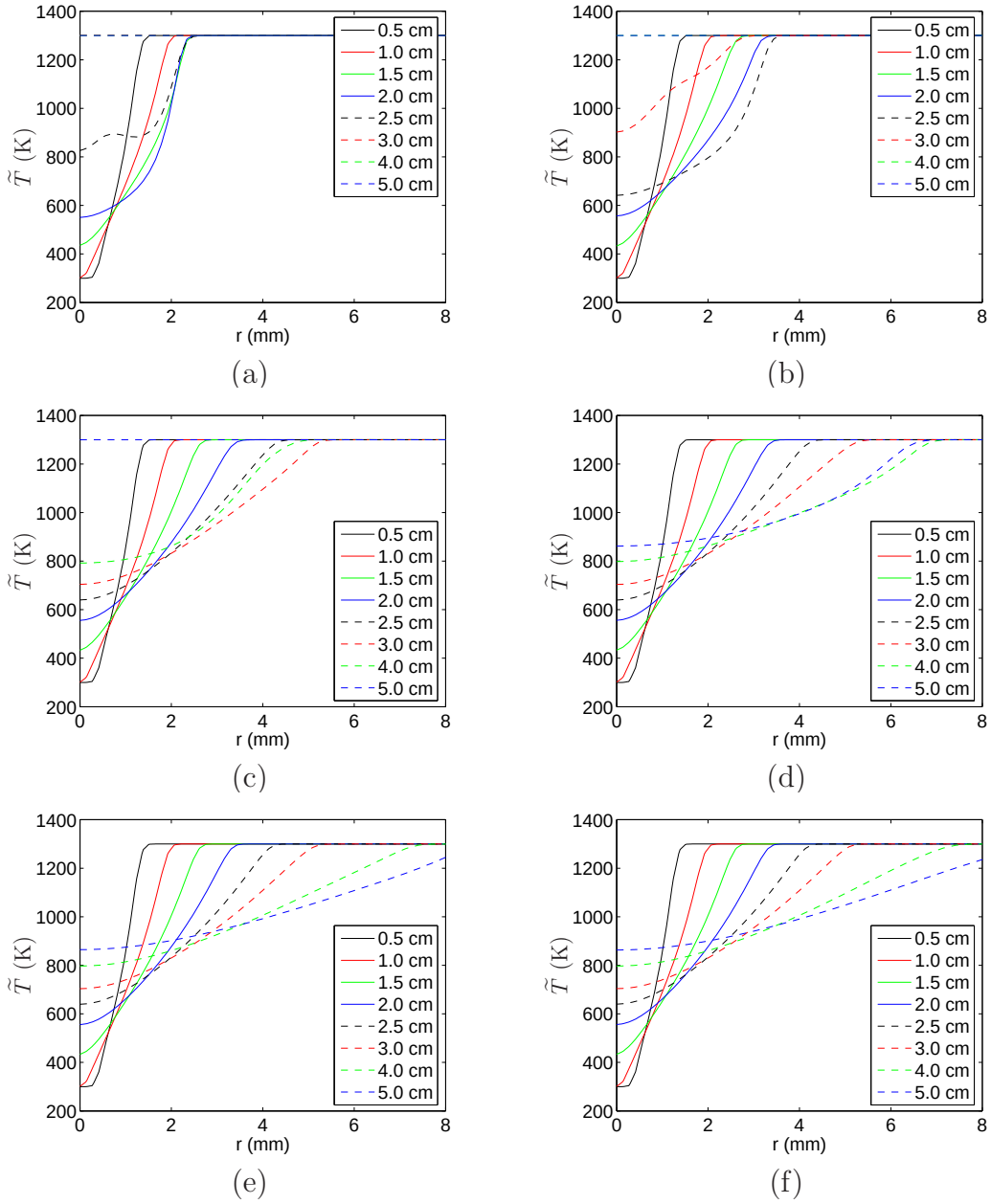

Figure 4.10: Radial variation of the Favre-averaged temperature at different locations along the jet centerline when $T_{air} = 1300$ K: a) $t = 0.20$ ms, (b) $t = 0.30$ ms,(c) $t = 0.60$ ms, (d) $t = 0.90$ ms, (e) $t = 1.20$ ms, and (f) $t = 1.50$ ms.

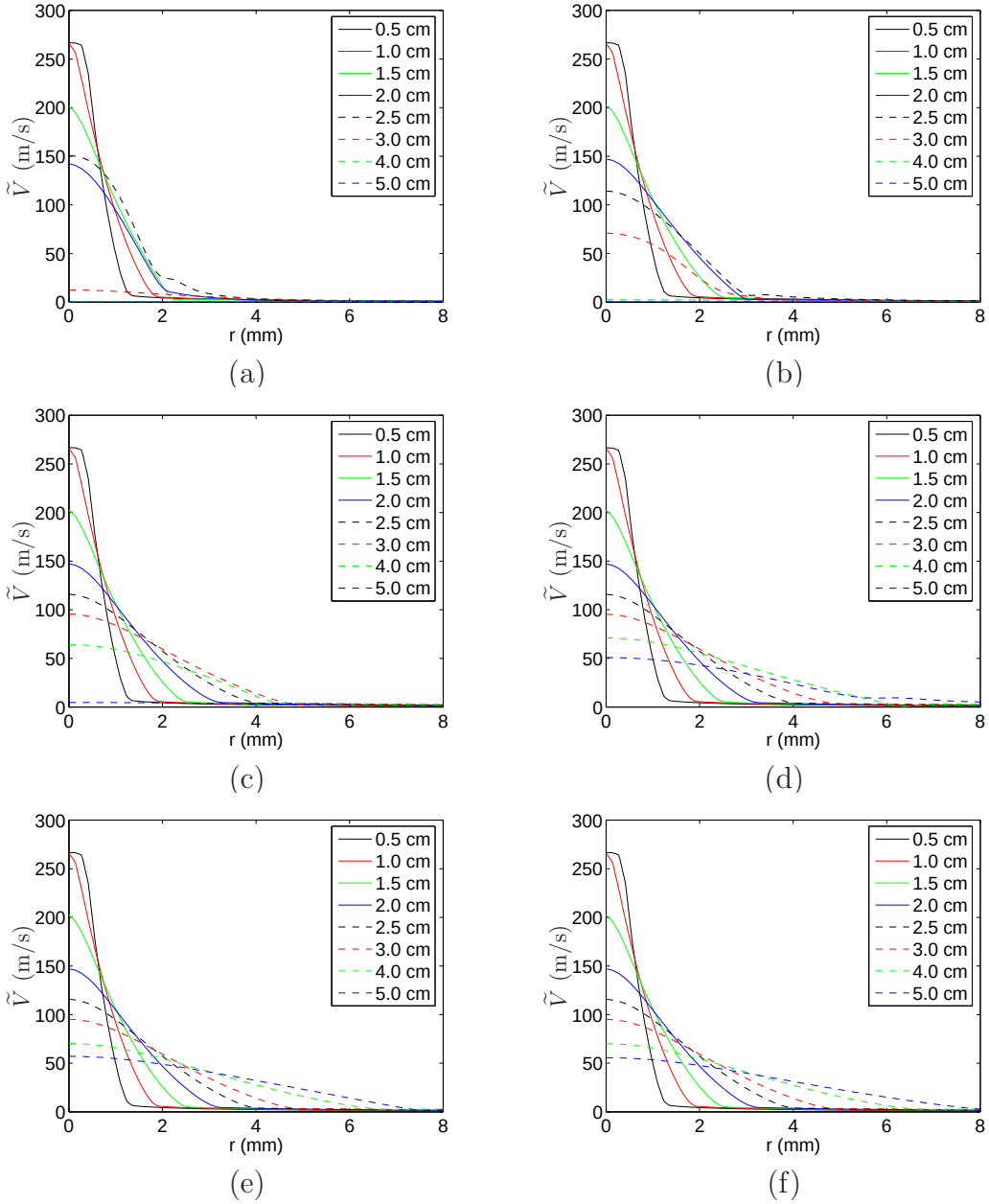

Figure 4.11: Radial variation of the Favre-averaged velocity (magnitude) at different locations along the jet centerline when $T_{air} = 1300$ K: a) $t = 0.20$ ms, (b) $t = 0.30$ ms,(c) $t = 0.60$ ms, (d) $t = 0.90$ ms, (e) $t = 1.20$ ms, and (f) $t = 1.50$ ms.

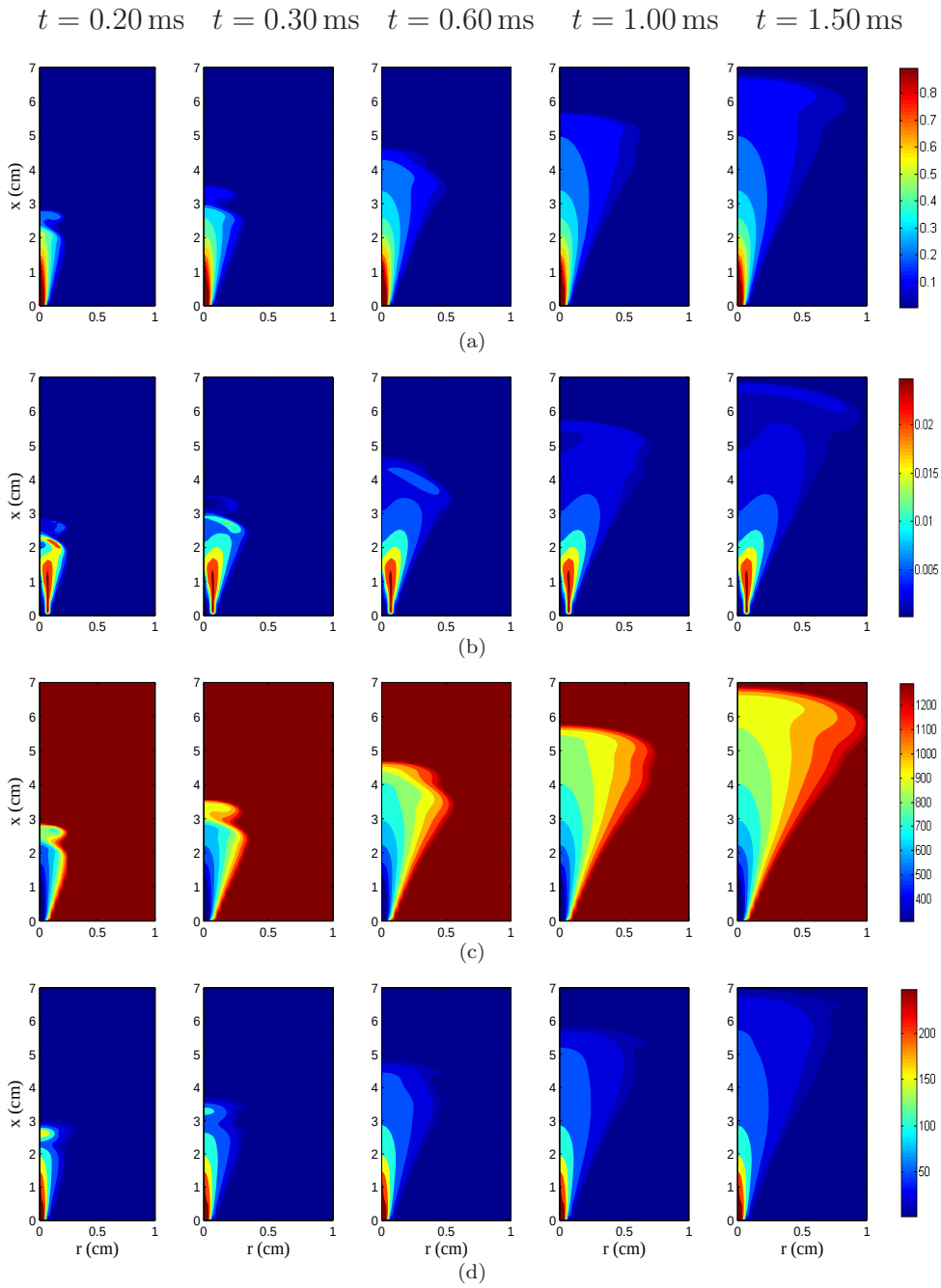

Figure 4.12: Contours of (a) $\tilde{\xi}$, (b) $\widetilde{\xi''^2}$, (c) $\tilde{T}$ and (d) $\tilde{V}$ for $T_{air} = 1300$ K at times $t = 0.20$, 0.30, 0.60, 1.00 and 1.50 ms.

4.5 Conclusions

This chapter presented the computational details used to reproduce the shock tube experiments conducted by Sullivan et al.[113]. The assumptions made in order to perform the frozen mixing calculations were discussed. It was found that changing $C_{\varepsilon 1}$ from the standard value of 1.44 to 1.535 resulted in good agreement (within $\pm 7\%$) with the penetration lenght correlation suggested by Hill et al.[44]. The transient behavior of the injected methane was found to compare well with the the vortex quasi-steady jet model proposed by Turner [120].

The next chapter presents the numerical solution of the CMC equations, and describes the tools used to perform the calculations.

Chapter 5

Numerical Solution of the CMC Equations

The numerical solution of the CMC equations is discussed. First, the shear flow approximation and the cross-stream averaging technique are presented, and the CMC equations are cross-stream averaged across the shear layer. Linear coupling between the enthalpy and the mixture fraction is also discussed. Then, the implementation of the fractional step method (operator splitting) and intermediate time steps is demonstrated. The discretization schemes of the different terms of the CMC equations are provided in detail along with the initial and boundary conditions. The numerical packages used in this study such as stiff and non-stiff ODE solvers and adaptive integrators are presented. Other numerical issues are also addressed. The components and the operation of the chemical kinetics package used in the simulations are briefly described. Finally, an overview on some of the chemical kinetics mechanisms that are relevant to this problem is given.

5.1 Cross-Stream Averaging

In this section, the cross-stream averaging technique in shear flows is introduced. The mathematical definition of the cross-stream average is provided and applied to the axial components of the conditional species and temperature equations.

5.1.1 Radial Dependence of Scalars in Shear Flows

While applying the CMC method to free shear flows, such as the turbulent round jet considered in this work, the radial dependence of the conditional averages of the species concentrations can be neglected. This is known as the shear flow approximation [62]. This assumption is supported by the experimental findings of Bilger [9], Stårner et al. [111] and Swaminathan et al. [115]. Kilmenko [62] also provided a mathematical proof that validates this assumption. Using asymptotic analysis, he showed that the dependence of the conditional expectation on a coordinate across the shear flow is weak. However, Klimenko [61] noted that the PDF is assumed to be a stronger function of the radial coordinate than the conditional mean concentrations. Accordingly, this dependence is accounted for by integrating the PDF-weighted axial component of the CMC equations (Section 5.1.3). This procedure reduces the three-dimensional axisymmetric round jet in hand to a one-dimensional problem.

This technique was successfully implemented by many authors in conjunction with the CMC method. Roomina et al. [104, 105] used this method for the prediction of turbulent methane-air and methanol jet flames while Devaud et al. [21, 23] implemented this technique for lifted turbulent hydrogen-air flames. Markides et al. [76] also employed this technique for the prediction of autoignition of an n-heptane plume in a turbulent flow of heated air.

5.1.2 Definition of the Cross-Stream Average

In cylindrical coordinates, for an axisymmetric flow, the area-weighted average of a scalar quantity $F(x, r, t)$ is defined as

$$\{F\}_R(x,t) = \frac{2}{R^2}\int_0^R F(x,r,t) r dr. \tag{5.1}$$

The cross-stream average of $F(t,x,r)$ is defined as ratio of the area-weighted average of the product $F(t,x,r)\tilde{P}(t,x,r,\eta)$, to the area-weighted average of $\tilde{P}(t,x,r,\eta)$:

$$\{F\}_{R^+}(t,x,\eta) = \frac{\left\{F(t,x,r)\tilde{P}(t,x,r,\eta)\right\}_R}{\left\{\tilde{P}(t,x,r,\eta)\right\}_R} = \frac{\int_0^R F(t,x,r)\tilde{P}(t,x,r,\eta)rdr}{\int_0^R \tilde{P}(t,x,r,\eta)rdr}, \tag{5.2}$$

where R is a large radius determined according to a cutoff imposed on the Favre-averaged mixture fraction in the flow field calculations. A total of 150 radial data points are considered at each axial location. A cutoff value of 10^{-2} is used throughout the calculations. Smaller cutoff values were tested and the differences in the cross-stream averages were shown negligible. Trapezoidal integration is employed in Eq.(5.2) to compute the different cross-stream averaged quantities. The test case considered in Section 4.4.4 (frozen mixing calculations with $T_{air} = 1300$ K) is revisited to demonstrate the usage of Eqs.(5.1) and (5.2). A 501-point mixture fraction grid is used in order to obtain a smooth representation. A coarser grid is employed in the CMC calculations (Section 6.1). Figure 5.1 shows the variation of the area-weighted PDF with axial position at $t = 1$ ms. As described by Eq.(5.2), this quantity is used to normalize the area-weighted average of the scalar-PDF product. For instance, Figures 5.2, 5.3 and 5.4 display the variation of the cross-stream averaged scalar dissipation rate ($\{\langle\chi|\eta\rangle\}_{R^+}$), axial velocity ($\{\langle u_x|\eta\rangle\}$) and turbulent diffusivity ($\{D_t\}_{R^+}$), respectively, at the same time and positions as in Figure 5.1. As expected, the intensity of mixing (conditional scalar dissipation rate) and the magnitude of the conditional velocity are high close to the inlet and decreases gradually downstream. The turbulent diffusivity shows an opposite trend.

5.1.3 Averaging of the CMC Equations

First, the conditional species transport equation (Eq.(3.29)) is considered. Applying the definition of the cross-stream average at a specific x-location along the jet centerline and

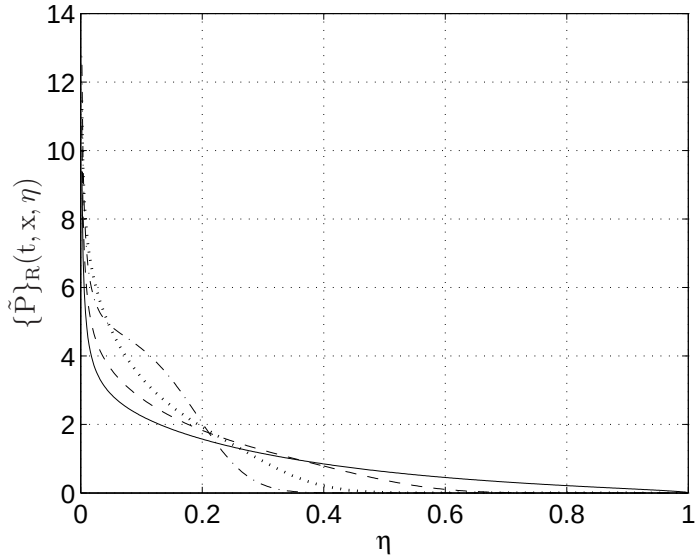

Figure 5.1: Axial variation of the area-weighted PDF at $t = 1$ ms: $x = 1$ cm (———), $x = 2$ cm (- - - - -), $x = 3$ cm ($\cdots\cdots$), and $x = 4$ cm ($-\cdot-\cdot-$).

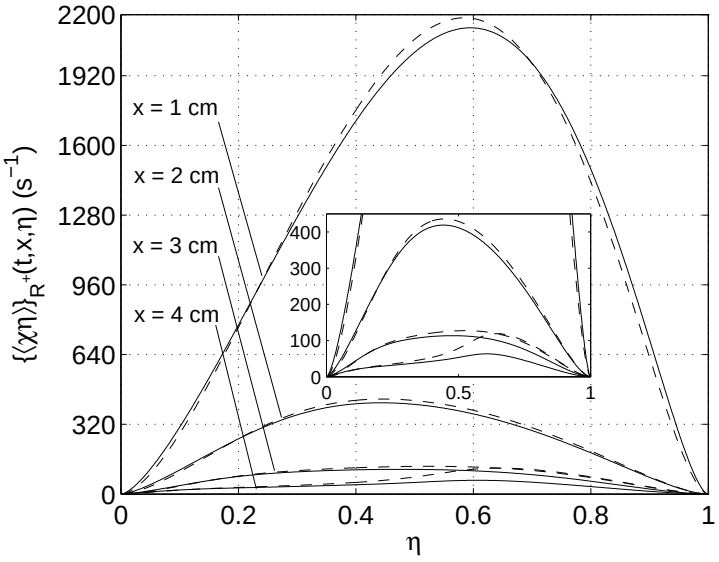

Figure 5.2: Axial variation of the cross-stream averaged conditional scalar dissipation rate at $t = 1$ ms: Girimaji's model-Eq.(3.36) (———) and the AMC model-Eq.(3.41) (- - - - -).

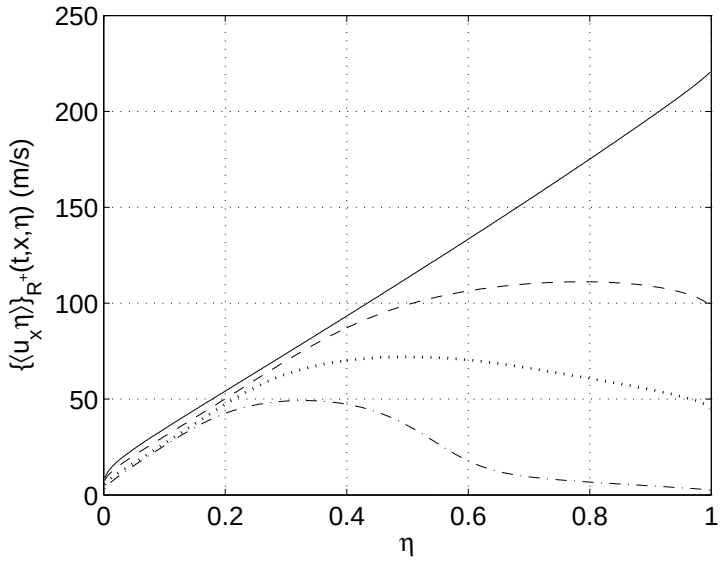

Figure 5.3: Axial variation of the cross-stream averaged axial velocity at $t = 1$ ms: $x = 1$ cm (———), $x = 2$ cm (- - - - -), $x = 3$ cm ($\cdots\cdots$), and $x = 4$ cm ($- \cdot - \cdot -$).

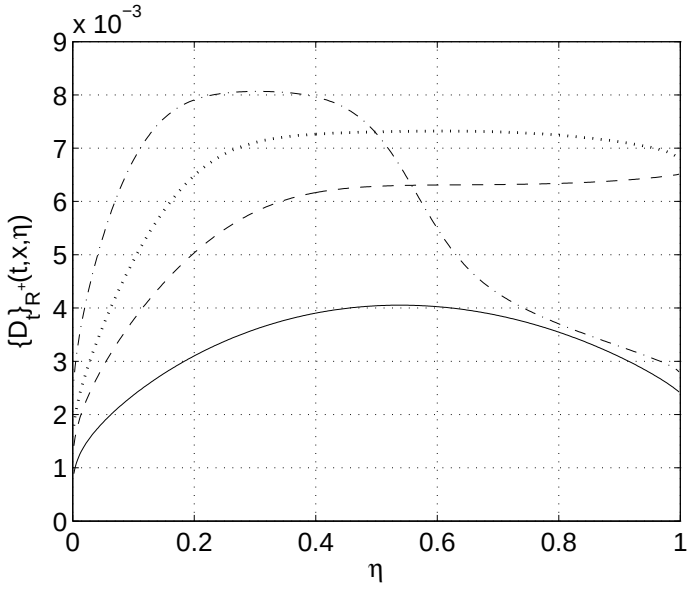

Figure 5.4: Axial variation of the cross-stream averaged turbulent diffusivity at $t = 1$ ms: $x = 1$ cm (———), $x = 2$ cm (- - - - -), $x = 3$ cm ($\cdots\cdots$), and $x = 4$ cm ($- \cdot - \cdot -$).

at a prescribed time t, as described by Eq.(5.2), the following expression is obtained

$$\frac{\int_0^R \frac{\partial Q_\alpha}{\partial t}\tilde{P}rdr}{\int_0^R \tilde{P}rdr} + \frac{\int_0^R \langle u_x|\eta\rangle \frac{\partial Q_\alpha}{\partial x}\tilde{P}rdr}{\int_0^R \tilde{P}rdr} = \frac{\int_0^R \frac{D_t}{\langle\rho\rangle\tilde{P}}\frac{\partial\left(\langle\rho\rangle\tilde{P}\right)}{\partial x}\frac{\partial Q_\alpha}{\partial x}\tilde{P}rdr}{\int_0^R \tilde{P}rdr} +$$
$$\frac{\int_0^R \frac{\partial D_t}{\partial x}\frac{\partial Q_\alpha}{\partial x}\tilde{P}rdr}{\int_0^R \tilde{P}rdr} + \frac{\int_0^R D_t\frac{\partial^2 Q_\alpha}{\partial x^2}\tilde{P}rdr}{\int_0^R \tilde{P}rdr} + \frac{\int_0^R \frac{1}{2}\langle\chi|\eta\rangle\frac{\partial^2 Q_\alpha}{\partial\eta^2}\tilde{P}rdr}{\int_0^R \tilde{P}rdr} + \frac{\int_0^R \frac{\langle\dot{\omega}_\alpha|\eta\rangle}{\langle\rho|\eta\rangle}\tilde{P}rdr}{\int_0^R \tilde{P}rdr}. \tag{5.3}$$

Following the shear flow approximation, since Q_α is not a function of r, its partial derivatives are not either. Hence $\partial Q_\alpha/\partial t$, $\partial Q_\alpha/\partial x$, $\partial^2 Q_\alpha/\partial x^2$ and $\partial^2 Q_\alpha/\partial\eta^2$ can be taken outside the integrals in Eq.(5.3). Using the notation of Eq.(5.2), Eq.(5.3) reduces to

$$\begin{aligned}\frac{\partial Q_\alpha}{\partial t} = &-\left[\{\langle u_x|\eta\rangle\}_{R^+} - \left\{\frac{D_t}{\langle\rho\rangle\tilde{P}}\frac{\partial(\langle\rho\rangle\tilde{P})}{\partial x}\right\}_{R^+} - \left\{\frac{\partial D_t}{\partial x}\right\}_{R^+}\right]\frac{\partial Q_\alpha}{\partial x}\\ &+\{D_t\}_{R^+}\frac{\partial^2 Q_\alpha}{\partial x^2} + \frac{1}{2}\{\langle\chi|\eta\rangle\}_{R^+}\frac{\partial^2 Q_\alpha}{\partial\eta^2} + \frac{\langle\dot{\omega}_\alpha|\eta\rangle}{\langle\rho|\eta\rangle}.\end{aligned} \tag{5.4}$$

The temperature equation (Eq.(3.30)) is cross-stream averaged in a similar fashion. The final result is given by:

$$\begin{aligned}\frac{\partial Q_T}{\partial t} = &-\left[\{\langle u|\eta\rangle\}_{R^+} - \left\{\frac{D_t}{\langle\rho\rangle\tilde{P}}\frac{\partial\left(\langle\rho\rangle\tilde{P}\right)}{\partial x}\right\}_{R^+} - \left\{\frac{\partial D_t}{\partial x}\right\}_{R^+}\right]\frac{\partial Q_T}{\partial x}\\ &+\{D_t\}_{R^+}\frac{\partial^2 Q_T}{\partial x^2} + \frac{1}{2}\{\langle\chi|\eta\rangle\}_{R^+}\left\{\frac{\partial^2 Q_T}{\partial\eta^2} + \frac{1}{\langle c_p|\eta\rangle}\left[\frac{\partial\langle c_p|\eta\rangle}{\partial\eta}\right.\right.\\ &\left.\left.+\sum_{\alpha=1}^{N_s}\left(\langle c_{p,\alpha}|\eta\rangle\frac{\partial Q_\alpha}{\partial\eta}\right)\right]\frac{\partial Q_T}{\partial\eta}\right\} - \frac{\langle\dot{\omega}_h|\eta\rangle}{\langle\rho|\eta\rangle\langle c_p|\eta\rangle}.\end{aligned} \tag{5.5}$$

With the shear flow approximation and the definition of the cross-stream average in mind (Eq.(5.2)), the two-dimensional configuration discussed in Chapter 4 is simplified to a one dimensional problem. Consequently, Eqs.(5.4) and (5.5) can be solved by applying finite differences (Section 5.3).

5.2 Enthalpy-Mixture Fraction Linear Coupling

As discussed in Section 3.2.2, by neglecting the pressure work and the radiation source term, the enthalpy equation reduces to

$$\rho\frac{\partial h}{\partial t}+\rho u_i\frac{\partial h}{\partial x_i}=\frac{\partial}{\partial x_i}\left(\rho D\frac{\partial h}{\partial x_i}\right). \tag{5.6}$$

By inspecting the mixture fraction equation

$$\rho\frac{\partial \xi}{\partial t}+\rho u_i\frac{\partial \xi}{\partial x_i}=\frac{\partial}{\partial x_i}\left(\rho D\frac{\partial \xi}{\partial x_i}\right), \tag{5.7}$$

it can be seen that both Eqs.(5.6) and (5.7) have exactly the same form. Consequently h can be related to ξ by the linear coupling equation [89]:

$$h=h_2+\xi(h_1-h_2), \tag{5.8}$$

where h_1 and h_2 are the enthalpies of fuel and air, respectively. Eq.(5.8) can be conditionally averaged at $\xi=\eta$ giving

$$Q_h=\langle h_2|\eta\rangle+\eta(\langle h_1|\eta\rangle-\langle h_2|\eta\rangle). \tag{5.9}$$

Eq.(5.9) remains invariant when cross-stream averaged since Q_h, $\langle h_1|\eta\rangle$ and $\langle h_2|\eta\rangle$ are independent of the radial coordinate (via the shear flow approximation). The conditional temperature, Q_T, is retrieved from Q_h. However, since Q_T is not a linear function of Q_h, an iterative linear interpolation procedure is used in order to compute Q_T.

This technique is attractive since solving the conditional temperature equation might introduce undesirable discretization errors and minor instabilities during the early stages of the solution. In addition, this procedure slightly decreases the computational cost of the simulations as few function calls and simple iterations would substitute the requirement of solving $N_x \times N_\eta$ ordinary differential equations at each time step, N_x and N_η being the number of grid points in physical and mixture fraction spaces, respectively.

5.3 Fractional Step Method

The fractional step method (or operator splitting) is a coupling approach in which a complicated ODE is split into a set of simpler coupled ODEs [30, 70, 85]. These ODEs are

solved sequentially (in separate steps) over consecutive fractions of the time step [100] and each ODE provides the subsequent one with the required initial conditions [30]. The main advantage of this process is that it allows separate treatment of the individual ODEs, depending on their nature [82]. For instance, some ODEs might be non-stiff and can be solved by simple matrix operations, while others might be stiff and require a stiff ODE solver. It should be noted that this method is valid only if the change in the physical variables from any of the individual processes is not too quick over a given time step [85]. This technique was previously applied to the CMC equations by Kim et al. [57], Devaud et al. [23] and Wright et al. [123]. For demonstration, the ODE

$$\frac{dF}{dt} = P_1 + P_2 + \cdots + P_{m-1} + P_m \tag{5.10}$$

consisting of m terms (P_1, P_1, …, P_{m-1}, and P_m) is considered. If each of the terms of eq.(5.10) is treated individually in a separate ODE as described above, m steps are required to advance the solution in time from t to $t + \Delta t$. One possible way to do this is given by the following sequence:

$$\begin{aligned}
&\underline{\text{Step } 1}: \quad [t, t + \Delta t/m] \\
&\frac{dF^1}{dt} = P_1 \quad \text{with} \quad F^1(0) = F(t) \\
&\underline{\text{Step } 2}: \quad [t + \Delta t/m, t + 2\Delta t/m] \\
&\frac{dF^2}{dt} = P_2 \quad \text{with} \quad F^2(0) = F^1(t + \Delta t/m) \\
&\qquad\qquad\qquad \vdots \\
&\underline{\text{Step } m-1}: \quad [t + (m-2)\Delta t/m, t + (m-1)\Delta t/m] \\
&\frac{dF^{m-1}}{dt} = P_{m-1} \quad \text{with} \quad F^{m-1}(0) = F^{m-2}(t + (m-2)\Delta t/m) \\
&\underline{\text{Step } m}: \quad [t + (m-1)\Delta t/m, t + \Delta t] \\
&\frac{dF^m}{dt} = P_m \quad \text{with} \quad F^m(0) = F^{m-1}(t + (m-1)\Delta t/m)
\end{aligned}$$

In the present work, since a large number of species is considered and detailed chemical kinetics are used (Section 5.7), the fractional step method is employed in order to treat separately the stiff chemical source term in the conditional transport equations. For this purpose, two steps are implemented. First, the solution is advanced in physical space (x-coordinate) over the first half of the time step, then in mixture fraction space (η-coordinate) over the second half. Eq.(5.11) shows the constituent terms of each step.

$$\frac{\partial Q_\alpha}{\partial t} = \boxed{\underbrace{-\left[\{\langle u_x|\eta\rangle\}_{R^+} - \left\{\frac{D_t}{\langle\rho\rangle\tilde{P}}\frac{\partial(\langle\rho\rangle\tilde{P})}{\partial x}\right\}_{R^+} - \left\{\frac{\partial D_t}{\partial x}\right\}_{R^+}\right]\frac{\partial Q_\alpha}{\partial x} + \{D_t\}_{R^+}\frac{\partial^2 Q_\alpha}{\partial x^2}}_{\text{spatial transport}}}^{\text{Step 1}}$$
$$+ \boxed{\underbrace{\frac{1}{2}\{\langle\chi|\eta\rangle\}_{R^+}\frac{\partial^2 Q_\alpha}{\partial\eta^2}}_{\text{micro-mixing}} + \underbrace{\frac{\langle\dot{\omega}_\alpha|\eta\rangle}{\langle\rho|\eta\rangle}}_{\text{chemical source}}}^{\text{Step 2}} \tag{5.11}$$

The first step is non-stiff and can be solved by LU-decomposition, while the second step is stiff and requires a stiff ODE solver. Although micro-mixing does not introduce any stiffness, it is included in the same step with the stiff chemical source, for convenience. In addition, few intermediate time steps are added within the time interval $[t, t+\Delta t]$ (Section 6.1) in order to insure convergence, and the fractional step method discussed above is applied at every intermediate step. Another benefit of introducing intermediate time steps is the increase in the decimal accuracy of ignition delay.

5.3.1 First Step: Non-Stiff ODE System – LU Decomposition

The first step involves solving the equation

$$\frac{\partial Q_\alpha}{\partial t} = -\left[\{\langle u_x|\eta\rangle\}_{R^+} - \left\{\frac{D_t}{\langle\rho\rangle\tilde{P}}\frac{\partial(\langle\rho\rangle\tilde{P})}{\partial x}\right\}_{R^+} - \left\{\frac{\partial D_t}{\partial x}\right\}_{R^+}\right]\frac{\partial Q_\alpha}{\partial x} + \{D_t\}_{R^+}\frac{\partial^2 Q_\alpha}{\partial x^2}. \tag{5.12}$$

For clarity, Ψ and Φ are defined as:

$$\Psi = -\left[\{\langle u_x|\eta\rangle\}_{R^+} - \left\{\frac{D_t}{\tilde{P}}\frac{\partial\tilde{P}}{\partial x}\right\}_{R^+} - \left\{\frac{\partial D_t}{\partial x}\right\}_{R^+}\right], \tag{5.13}$$

and

$$\Phi = \{D_t\}_{R^+}. \tag{5.14}$$

Thus, Eq.(5.12) may be written as

$$\frac{\partial Q_\alpha}{\partial t} = \Psi \frac{\partial Q_\alpha}{\partial x} + \Phi \frac{\partial^2 Q_\alpha}{\partial x^2}. \tag{5.15}$$

Integration of Eq.(5.15) with respect to time yields

$$\int_t^{t+\Delta t} \frac{\partial Q_\alpha}{\partial t} dt = \int_t^{t+\Delta t} \Psi \frac{\partial Q_\alpha}{\partial x} dt + \int_t^{t+\Delta t} \Phi \frac{\partial^2 Q_\alpha}{\partial x^2} dt. \tag{5.16}$$

Using the fully implicit scheme at node i, Eq.(5.16) becomes:

$$Q_\alpha|_i^{t+\Delta t} - Q_\alpha|_i^t = \Psi|_i^{t+\Delta t} \frac{\partial Q_\alpha}{\partial x}\bigg|_i^{t+\Delta t} \Delta t + \Phi|_i^{t+\Delta t} \frac{\partial^2 Q_\alpha}{\partial x^2}\bigg|_i^{t+\Delta t} \Delta t, \tag{5.17}$$

where $1 \leq i \leq N_x$. The solution at the left boundary, i.e. at $i = 1$ ($x = 0$), is not needed since the composition at this location is known at all times. Thus, the numerical solution is only required for $1 < i \leq N_x$. Since the flow direction is from left to right (see Figures 4.1 and 4.3), first order backward differencing is used to discretize the first derivative of Q_α with respect to x:

$$\frac{\partial Q_\alpha}{\partial x} = \frac{Q_\alpha|_i^{t+\Delta t} - Q_\alpha|_{i-1}^{t+\Delta t}}{\Delta x_1} \tag{5.18}$$

where $\Delta x_1 = x_i - x_{i-1}$ and $\Delta x_2 = x_{i+1} - x_i$. As for the second derivative of Q_α with respect to x, second order central differencing is used for $1 < i < N_x$, while first order backward differencing is used when $i = N_x$, as shown in Eqs.(5.19) and (5.20), respectively.

$$\frac{\partial^2 Q_\alpha}{\partial x^2}\bigg|_i^{t+\Delta t} = 2\left[\frac{Q_\alpha|_{i-1}^{t+\Delta t}}{\Delta x_1(\Delta x_1 + \Delta x_2)} - \frac{Q_\alpha|_i^{t+\Delta t}}{\Delta x_1 \Delta x_2} + \frac{Q_\alpha|_{i+1}^{t+\Delta t}}{\Delta x_2(\Delta x_1 + \Delta x_2)}\right] \quad \text{for } 1 < i < N_x, \tag{5.19}$$

where $\Delta x_1 = x_i - x_{i-1}$ and $\Delta x_2 = x_{i+1} - x_i$.

$$\frac{\partial^2 Q_\alpha}{\partial x^2}\bigg|_i^{t+\Delta t} = 2\left[\frac{Q_\alpha|_i^{t+\Delta t}}{\Delta x_1 \Delta x_2} - \frac{Q_\alpha|_{i-1}^{t+\Delta t}}{\Delta x_1(\Delta x_1 - \Delta x_2)} + \frac{Q_\alpha|_{i-2}^{t+\Delta t}}{\Delta x_2(\Delta x_1 - \Delta x_2)}\right] \quad \text{for } i = N_x, \tag{5.20}$$

where $\Delta x_1 = x_i - x_{i-1}$ and $\Delta x_2 = x_i - x_{i-2}$.
Combining Eqs.(5.17), (5.18) and (5.19), the discretized conditional species transport equation for an internal node takes the form

$$\left[-\frac{2\Psi|_i^{t+\Delta t}\Delta t}{\Delta x_1(\Delta x_1+\Delta x_2)}+\frac{\Phi|_i^{t+\Delta t}\Delta t}{\Delta x_1}\right]Q_\alpha|_{i-1}^{t+\Delta t}+\left[1+\frac{2\Psi|_i^{t+\Delta t}\Delta t}{\Delta x_1\Delta x_2}-\frac{\Phi|_i^{t+\Delta t}\Delta t}{\Delta x_1}\right]Q_\alpha|_i^{t+\Delta t} -\left[\frac{2\Psi|_i^{t+\Delta t}\Delta t}{\Delta x_2(\Delta x_1+\Delta x_2)}\right]Q_\alpha|_{i+1}^{t+\Delta t}=Q_\alpha|_i^t, \tag{5.21}$$

where $\Delta x_1 = x_{i+1} - x_i$ and $\Delta x_2 = x_i - x_{i-1}$. On the other hand, by substituting Eqs.(5.18) and (5.20) in Eq.(5.17), the discretized equation at the rightmost boundary node takes the form

$$-\left[\frac{2\Psi|_i^{t+\Delta t}\Delta t}{\Delta x_2(\Delta x_1-\Delta x_2)}\right]Q_\alpha|_{i-2}^{t+\Delta t}+\left[\frac{2\Psi|_i^{t+\Delta t}\Delta t}{\Delta x_1(\Delta x_1-\Delta x_2)}+\frac{\Phi|_i^{t+\Delta t}\Delta t}{\Delta x_1}\right]Q_\alpha|_{i-1}^{t+\Delta t} +\left[1-\frac{2\Psi|_i^{t+\Delta t}\Delta t}{\Delta x_1\Delta x_2}-\frac{\Phi|_i^{t+\Delta t}\Delta t}{\Delta x_1}\right]Q_\alpha|_i^{t+\Delta t}=Q_\alpha|_i^t \tag{5.22}$$

where $\Delta x_1 = x_i - x_{i-1}$ and $\Delta x_2 = x_i - x_{i-2}$. Eqs.(5.21) and (5.22) may be arranged in the following matrix equation

$$\begin{bmatrix} 1 & 0 & 0 & 0 & 0 & 0 & \cdots & 0 & 0 & 0 \\ A_2 & B_2 & C_2 & 0 & 0 & 0 & \cdots & 0 & 0 & 0 \\ 0 & A_3 & B_3 & C_3 & 0 & 0 & \cdots & 0 & 0 & 0 \\ 0 & 0 & A_4 & B_4 & C_4 & 0 & \cdots & 0 & 0 & 0 \\ \vdots & \vdots & \vdots & & & \ddots & & \vdots & \vdots & \vdots \\ 0 & 0 & 0 & 0 & 0 & 0 & A_{N_x-2} & B_{N_x-2} & C_{N_x-2} & 0 \\ 0 & 0 & 0 & 0 & 0 & 0 & 0 & A_{N_x-1} & B_{N_x-1} & C_{N_x-1} \\ 0 & 0 & 0 & 0 & 0 & 0 & 0 & A_b & B_b & C_b \end{bmatrix} \times \begin{bmatrix} Q_\alpha|_1^{t+\Delta t} \\ Q_\alpha|_2^{t+\Delta t} \\ Q_\alpha|_3^{t+\Delta t} \\ Q_\alpha|_4^{t+\Delta t} \\ \vdots \\ Q_\alpha|_{N_x-2}^{t+\Delta t} \\ Q_\alpha|_{N_x-1}^{t+\Delta t} \\ Q_\alpha|_{N_x}^{t+\Delta t} \end{bmatrix} = \begin{bmatrix} Q_\alpha|_1^t \\ Q_\alpha|_2^t \\ Q_\alpha|_3^t \\ Q_\alpha|_4^t \\ \vdots \\ Q_\alpha|_{N_x-2}^t \\ Q_\alpha|_{N_x-1}^t \\ Q_\alpha|_{N_x}^t \end{bmatrix}$$

where A_i, B_i and C_i are the coefficients of $Q_\alpha|_{i-1}^{t+\Delta t}$, $Q_\alpha|_i^{t+\Delta t}$ and $Q_\alpha|_{i+1}^{t+\Delta t}$ in Eq.(5.21), respectively ($1 < i < N_x$). A_b, B_b and C_b are the coefficients of $Q_\alpha|_{i-2}^{t+\Delta t}$, $Q_\alpha|_{i-1}^{t+\Delta t}$ and

$Q_\alpha|_i^{t+\Delta t}$ in Eq.(5.22), respectively ($i = N_x$). This matrix is solved using LU-decomposition. The subroutines LUDCMP and LUBKSB [100] are employed to carry out the calculations. LUDCMP performs the LU-decomposition, while LUBKSB executes the necessary forward and backward substitutions. The algorithms of both subroutines are explained in reference [100]. It should be noted that the entry 1 in the first row of the coefficient matrix (which corresponds to $i = 1$ or $x = 0$, where the composition is know at all times) is included as a requirement for the proper operation of the subroutines.

5.3.2 Second Step: Stiff ODE System – LSODE

Micro-mixing and the stiff chemical source term are teated in this fractional step, i.e.

$$\frac{\partial Q_\alpha}{\partial t} = \frac{1}{2}\{\langle\chi|\eta\rangle\}_{R^+}\frac{\partial^2 Q_\alpha}{\partial \eta^2} + \frac{\langle\dot{\omega}_\alpha|\eta\rangle}{\langle\rho|\eta\rangle}. \tag{5.23}$$

is solved. The solution of the first fractional step is used as the initial conditions for Eq.(5.23). The double precision version of the solver LSODE (Livermore Solver for Ordinary Differential Equations) [45] is used to handle the stiff chemical kinetics. LSODE solves the initial value problem for stiff or non-stiff systems of first-order ODEs of the form [101]:

$$\begin{cases} \dfrac{d\mathbf{Y}}{dt} = \mathbf{f}(t, \mathbf{Y}(t)) \\ \mathbf{Y}(t_0) = \mathbf{Y_0} \ \text{(given)} \end{cases} \tag{5.24}$$

or in component form,

$$\begin{cases} \dfrac{dY_i(t)}{dt} = f_i(t, Y_1(t), Y_2(t), \ldots, Y_{N_e}(t)), \ i = 1, 2, \ldots, N_e \\ Y_i(t_0) = Y_{i,0} \ \text{(given)} \end{cases} \tag{5.25}$$

where N_e is the number of ODEs. LSODE uses Adams methods (predictor-corrector) in the non-stiff case, and Backward Differentiation Formula (BDF) methods (the Gear methods) in the stiff case. If the system is stiff, LSODE treats the Jacobian matrix $\mathbf{J} = d\mathbf{f}/d\mathbf{Y}$ as either a dense (full) or a banded matrix. $\mathbf{J}$ is either supplied by the user or generated internally by difference quotients. The resulting linear systems are solved by direct methods. Further details on the features and options of LSODE can be found in references [45, 101].

In the current work, the solver is configured to use the variable-step implicit BDF integration method and a modified Newton iteration technique with an internally generated banded Jacobian [20]. A maximum of 1500 of internally defined steps are allowed during one call to the solver. The absolute and relative tolerances are set to 10^{-20} and 10^{-5}, respectively. The time step is equal to the time interval used to build the transient libraries from the frozen mixing calculations (Section 4.2). The term $\partial^2 Q/\partial\eta^2$ appearing in the first term on the RHS of Eq.(5.23) is discretized using second order central differencing.

5.4 Initial and Boundary Conditions

5.4.1 Initial Conditions

The initial conditional enthalpy, Q_h, is computed using the linear coupling technique which was introduced in Section 5.2. The initial conditional temperature, Q_T, is calculated from Q_h by iterative linear interpolation. Figure 5.5 shows the initial distributions of Q_h and Q_T in mixture fraction space for the test case where $T_{air} = 1300$ K. It can be seen in Figure 5.5(b) that $Q_T = T_{air} = 1300$ K at $\eta = 0$ (pure air) and $Q_T = T_{fuel} = 300$ K at $\eta = 1$ (pure fuel). It should be noted here that air is assumed to consist of 23.3% O_2 and 76.7% N_2, while the minor species such as H_2O, CO_2 and Ar are neglected. Figure 5.6 shows the initial distribution of the conditional concenration of CH_4, O_2 and N_2. At $\eta = 0$, the mixture consists of pure air (23.3% O_2 + 76.7% N_2), while at $\eta = 1$ it consists of pure CH_4. The concentration of the remaining species included in the chemical reaction mechanism (Section 5.7) are set equal to zero (initially the concentration of the products is equal to zero due to the absence of chemical reactions and the mixture only consists of the reactants). Every node in physical space is intialized with the temperature and concentration profiles shown in Figures 5.5(b) and (5.6).

5.4.2 Boundary Conditions

Boundary conditions need to be set only at $x = 0$. In the previous section it was shown how Q_T and Q_α are initialized at every node in physical space. Since Q_T and Q_α are known at $x = 0$ for any given time, Dirichlet boundary conditions are used at this location by

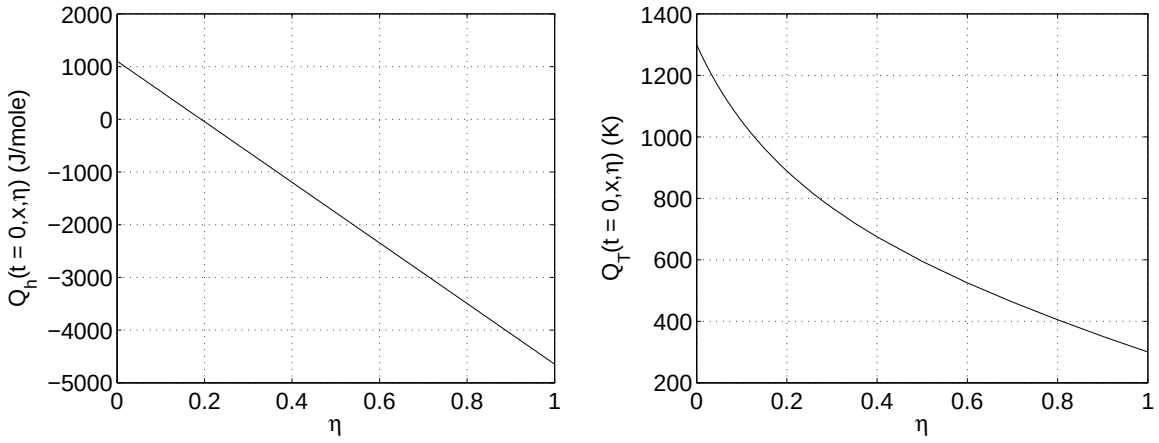

(a) (b)

Figure 5.5: Initial conditional (a) enthalpy and (b) temperature for $T_{air} = 1300$ K

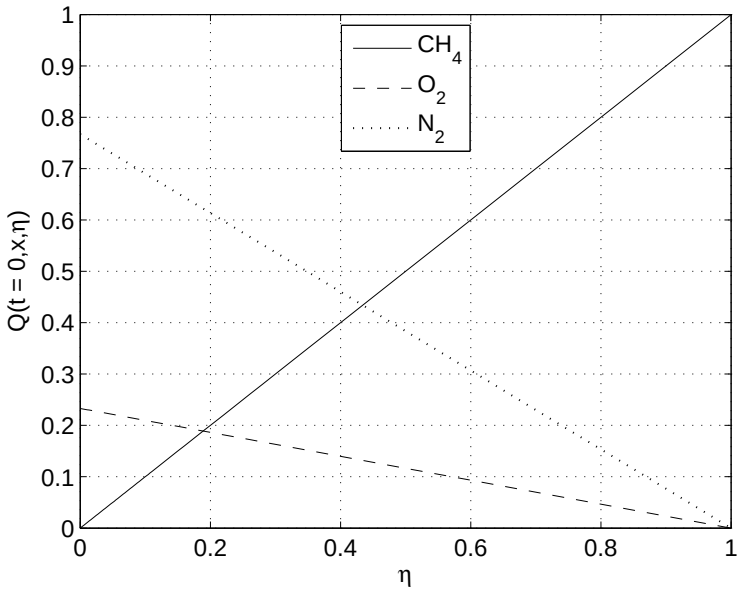

Figure 5.6: Initial conditional concentrations of CH_4, O_2 and N_2.

setting Q_T and Q_α equal to their initial values.

5.5 Integration Singularities and Strategies

As mentioned in Chapter 3, singularities are encountered in some of the CMC submodels like the β-PDF (Section 3.3.2) and the conditional scalar dissipation rate models (Section 3.3.3). This section addresses those issues, in addition to the special treatment of the integral $I(\eta)$ (Eqs.(3.36) and (3.38)).

5.5.1 QUADPACK

QUADPACK [92] is an open source FORTRAN package for the numerical computation of one-dimensional integrals. It consists of a collection of routines for adaptive and non-adaptive integration. It is capable of computing integrals over infinite and semi-infinite ranges, singular (including logarithmic singularities) and oscillatory integrals, etc [41]. These routines are automatic, i.e. they perform the integration to within the prescribed relative or absolute accuracy, and they return an error estimate at the end of the integration. The package also includes some non-adaptive and non-automatic routines.

Three singular integrals were discussed in Chapter 3. The first two are I_1 and I_2 used in the modeling of the conditional scalar dissipation rate by Girimaji's model [38]. These integrals are given by:

$$I_1 = \int_0^1 \ln\eta \, d\eta, \tag{5.26}$$

and

$$I_2 = \int_0^1 \ln(1-\eta) \, d\eta. \tag{5.27}$$

I_1 is singular at $\eta = 0$, while I_2 is singular at $\eta = 1$. The third integral appears in the denominator of $\langle\chi|0.5\rangle$, which is used in the modeling of the conditional scalar dissipation rate by the AMC model [84]. This integral is given by:

$$\int_0^1 G(\eta)\tilde{P}(\eta)d\eta \tag{5.28}$$

The singularities in Eq.(5.28) originate only from the β-PDF, since $G(\eta)$ cancels its own singularities, as discussed in Section 3.3.3. The singularities in this case might occur at $\eta = 0$ or $\eta = 1$, depending on the values of the parameters β_1 and β_2 in Eq.(3.31). The routine DQAGS is used to compute the integrals in Eqs.(5.26), (5.27) and (5.28). DQAGS is a double precision adaptive integration (quadrature) routine that integrates general functions with singularities over a finite range. If an integrable singularity exists, this routine increases the number of subintervals in its neighborhood. This process is called adaptive bisection. In addition, DQAGS uses the Epsilon algorithm to speed up the calculations [41]. As the size of the subintervals decrease, the consecutive approximations to the integral converge gradually. A relative accuracy of 10^{-8} is used at all times.

5.5.2 Integration of $I(\eta)$ in Gitimaji's Model

The integration of

$$I(\eta) = \int_0^{\eta} \underbrace{\left\{\tilde{\xi}(\ln\eta' - I_1) + (1-\tilde{\xi})\left[\ln(1-\eta') - I_2\right]\right\}\tilde{P}(\eta')(\eta-\eta')}_{F(\eta')}\, d\eta' \tag{5.29}$$

is carried out using the strategy adopted by Devaud [20]. Eq.(5.29) is integrated over the range $[0, \eta]$ or $[\eta, 1]$ based on the value of the mixture fraction $\tilde{\xi}$ as follows:

$$I(\eta) = \begin{cases} \displaystyle\int_0^{\eta} F(\eta')d\eta' & \text{if } \eta \leq \tilde{\xi} \\ \displaystyle\int_1^{\eta} F(\eta')d\eta' & \text{if } \eta > \tilde{\xi} \end{cases} \tag{5.30}$$

Further details can be found in reference [20].

5.6 CHEMKIN II

CHEMKIN II version 2.0 [52] is a FORTRAN chemical kinetics package for the analysis of gas-phase chemical kinetics. It computes the reaction rates, the species concentrations, and the different thermodynamic quantities such as the pressure, the enthalpy, the density, the specific heats, etc. The package consists of five components:

1. Interpreter: FORTRAN code,
2. Chemical Kinetics Mechanism: file written in CHEMKIN format (user supplied),
3. Thermodynamic Database: file written in CHEMKIN format (user supplied),
4. Linking File: internally generated file,
5. Gas-Phase Subroutine Library: FORTRAN code.

The Interpreter reads the Chemical Kinetics Mechanism and extracts the appropriate thermodynamic information for the species included in the mechanism from the Thermodynamic Database. Both the Chemical Kinetics Mechanism and the Thermodynamic Database are written in a special format that is recognizable by the interpreter (CHEMKIN format). Afterwards, the Interpreter generates an output file called the Linking File. This file contains all the required information on the elements, species, and chemical reactions involved in the Chemical Kinetics Mechanism. This file should be also used by the user to generate three arrays of differ

5.7 Chemical Kinetics Mechanisms

In this section the different chemical kinetics mechanisms used throughout this study are briefly described. Three mechanisms are considered: GRI-Mech 1.2 [32, 33], GRI-Mech 3.0 [107] and UBC-Mech 1.0 [49]. Only the last two are used in the calculations. The first mechanism is an older version of GRI-Mech 3.0 and represents the building block UBC-Mech 1.0.

5.7.1 GRI-Mech 1.2

GRI-Mech 1.2 [32, 33] is the second version of the GRI (Gas Research Institute) mechanism (after 1.1). This mechanism is designed to model the combustion of natural gas. It consists of 5 elements (O, H, C, N, Ar), 32 species, and 177 chemical reactions. However, it does not include the NO_x formation reactions. Numerical simulations show that the calculated low-temperature high-pressure oxidation rates of methane are faster than experiment by

about 20-30% [33]. As a direct consequence, the predicted ignition delays are shorter than the experimental delays. Thus, GRI-Mech 1.2 is not suitable for such conditions. However, it yields better predictions at higher temperatures and lower pressures [33].

5.7.2 GRI-Mech 3.0

GRI-Mech 3.0 [107] is the fourth version of the GRI mechanism (after 1.1, 1.2 ans 2.11). It is an optimized version of the previous versions (see reference [107] for changes from earlier versions). It consists of 5 elements, 53 species and 325 chemical reactions. The optimal operating conditions of this mechanism range from 1000 to 2500 K for temperature, from 10 Torr to 10 atm for pressure, and from 0.1 to 5 for equivalence ratio of premixed systems [107]. Since the NO_x chemistry has negligible effect on the temperature [43], all the species and chemical reactions related to NO_x formation were removed from the mechanism for computational efficiency as in Kim [57]. However, N_2 and its reactions (two) were kept. At the end, the mechanism was reduced to 36 species and 227 chemical reactions (including duplicate reactions). Numerical simulations show that GRI-Mech 3.0 generally performs better than the older versions [107]. Furthermore, simulations of methane ignition at intermediate and high temperatures and low pressures yield good predictions compared to experiments [107].

5.7.3 UBC Mech 1.0

UBC-Mech 1.0 [49] is based on GRI-Mech 1.2 [32, 33]. It consists of 5 elements, 38 species and 192 chemical reactions. This mechanism is optimized for the combustion of natural gas for initial pressures above 16 atm, temperatures below 1400 K, and equivalence ratios ranging from 0.7 to 1.3. The following adjustments were made to GRI-Mech 1.2 [49]:

1. Species that are important in the oxidation of CH_4 at low temperatures such as CH_3O_2, CH_3O_2H, C_2H_5O, $C_2H_5O_2$, $C_2H_5O_2H$, and CH_3CO were included, following Petersen et al. [91]. Correspondingly, 13 reactions are added to the mechanism. These reactions are given in Table 5.1 along with the frequency factor (A), the reaction exponent (b), and the activation energy (E_a). To be noted that the value of

A in the second reaction in Table 5.1 (reaction 179 in the mechanism) was modified from 8.52×10^{58} to 2.13×10^{58} mole.cm.s.K, as suggested by Tsang et al. [119]

2. Reaction 157 in GRI-Mech 1.2 was replaced by it reverse reaction.

$$HO_2 + CH_4 \rightleftarrows CH_3 + H_2O_2$$

with A changed from 2.450×10^4 to 4.480×10^{13} mole.cm.s.K, b from 2.470 to 0.0, and E_a from 5180.00 to 24629.00 cal/mole.

4. Two reactions involving CH_3O_2 were added. These reactions are given in Table 5.2 along with the corresponding A, b and E_a values.

Further details on this mechanism can be found in reference [49]. The performance of this mechanism compared to GRI-Mech 3.0 is discussed in the next chapter.

5.8 Conclusions

This chapter discussed the numerical solution of the CMC equations. The equations were cross-stream averaged across the jet based on the shear flow approximation. Linear coupling between the enthalpy and the mixture fraction was also discussed as an alternative strategy for solving the conditional temperature equation. The fractional step method was applied to the CMC equations in order to treat separately the stiff chemical source term. Two fractional steps were used: in the first spatial transport is solved using LU-decomposition, while in the second the micro-mixing and chemical source terms are solved using the stiff ODE solver LSODE [45]. The used discretization schemes and initial and boundary conditions were also discussed. The adaptive integrator QUADPACK [92] and the chemical kinetics package CHEMKIN II [52] were briefly described and their usage was demonstrated. Finally, some of the relevant chemical kinetics mechanisms were presented.

The next chapter presents the CMC autoignition results of low-temperature methane in high-pressure air over a wide range of initial air temperatures.

Table 5.1: Additional chemical reaction involving the species CH_3O_2, CH_3O_2H, C_2H_5O, $C_2H_5O_2$, $C_2H_5O_2H$, and CH_3CO.

Reaction	A (mole.cm.s.K)	b	E_a (cal/mole)
$CH_3 + OH \rightleftarrows CH_2O + H_2$	8.00×10^{12}	0.0	0.0
$CH_3 + O_2 \rightleftarrows CH_3O_2$	2.13×10^{58}	-15.0	17018.0
$C_2H_5O \rightleftarrows CH_2O + CH_3$	1.00×10^{15}	0.0	21606.0
$CH_3O + HO_2 \rightleftarrows CH_2O + H_2O_2$	1.20×10^{13}	0.0	0.0
$CH_3O + CH_3 \rightleftarrows CH_2O + CH_4$	2.41×10^{13}	0.0	0.0
$CH_3O_2H \rightleftarrows CH_3O + OH$	6.46×10^{14}	0.0	42996.0
$CH_3O_2 + CH_3 \rightleftarrows CH_3O + CH_3O$	3.00×10^{13}	0.0	-1200.0
$CH_3O_2 + H2O_2 \rightleftarrows CH_3O_2H + HO_2$	2.40×10^{12}	0.0	9942.0
$CH_3O_2 + CH_2O \rightleftarrows CH_3O_2H + HCO$	2.00×10^{12}	0.0	11663.0
$CH_3O_2 + CH_4 \rightleftarrows CH_3O_2H + CH_3$	1.80×10^{11}	0.0	18475.0
$C_2H_5 + O_2 \rightleftarrows C_2H5O_2$	1.00×10^{12}	0.0	0.0
$C_2H_5O_2 + CH_2O \rightleftarrows C_2H5O_2H + HCO$	2.00×10^{12}	0.0	11663.0
$C_2H_5O_2H \rightleftarrows C_2H_5O + OH$	1.00×10^{16}	0.0	42977.0

Table 5.2: Extended CH_3O_2 reactions.

Reaction	A (mole.cm.s.K)	b	E_a (cal/mole)
$CH_3O_2 + HO_2 \rightleftarrows CH_3O_2H + O_2$	4.60×10^{10}	0.0	-2600.0
$CH_3O_2 + CH_3O_2 + O_2 \rightleftarrows CH_3O + CH_3O$	3.70×10^{11}	0.0	2200.0

Chapter 6

Ignition of Non-Premixed Methane-Air Mixtures

Ignition delay of low-temperature methane in high-pressure diesel-like environments is investigated using CMC. The cross-stream averaged homogeneous and inhomogeneous CMC equations are solved for a wide range of initial air temperatures. Both scalar dissipation models discussed earlier in Section 3.3.3 are implemented to determine the conditional mean scalar dissipation rate. Unless indicated differently, the chemical kinetics mechanism UBC-Mech 1.0 [49] is used and the ignition criterion is based on a 75 K increase in the temperature, anywhere in physical or mixture fraction spaces [42]. This ignition criterion was found to be well correlated with the optical criteria used in the shock tube experiments discussed in Section 4.1 [42]. The results are compared to the shock tube experimental data of Sullivan et al. [113]. Perfectly homogeneous reactor calculations are also performed and the critical value of the scalar dissipation rate for ignition is determined. Several ignition criteria used in the literature are also investigated. The widely used chemical kinetics mechanisms GRI-Mech 3.0 [107] is also tested. Finally, the results are compared with other experiments and numerical simulations. Some results of this chapter were published in the proceedings the International Colloquium on the Dynamics of Explosions and Reactive Systems [25] and in the proceedings the Canadian Section of the Combustion Institute [26].

6.1 Sensitivity Analysis

Before performing any calculations, it is essential to examine the sensitivity of the grids in both physical and mixture fraction spaces and the effect of the time step on the solution. For this purpose, several grids and time steps are tested. In all cases, the cross-stream averaged species transport equation (Eq.(5.4)) is solved and the conditional temperature in obtained from the conserved conditional enthalpy by iterative linear interpolation. The AMC model is used to calculate the conditional scalar dissipation rate. In addition, the second conditional temperature solution strategy described in Section 5.2 is also visited.

6.1.1 Physical Space: x-Grid

Two grids were tested in physical space:

1. 21-point uniform grid with $\Delta x = 0.50$ cm
2. 29-point nonuniform grid with $\Delta x = \begin{cases} 0.25 \text{ cm if } 0 \leq x \leq 4 \text{ cm} \\ 0.50 \text{ cm if } 4 \text{ cm} < x \leq 10 \text{ cm} \end{cases}$

A 63-point mixture fraction grid refined around the stoichiometry ($\eta_{st} = 0.055$) and a 0.05 ms global time step with 10 intermediate time steps were used in the calculations. Air temperatures ranging from 1250 K to 1400 K were considered. The results showed that only the ignition locations in physical space were affected (by one grid point at most). As a conclusion, refinement of the x-grid gives a better idea about the axial ignition location without affecting the value of the ignition delay and mixture fraction values. The 29-point nonuniform grid is chosen to perform the subsequent CMC calculations.

6.1.2 Mixture Fraction Space: η-Grid

Three nonuniform mixture fraction grids were tested: 43-point (coarse), 63-point (intermediate) and 125-point (fine). All three grids were refined around $\eta_{st} = 0.055$. The test case where the air temperature is equal to 1350 K was investigated using the 29-point nonuniform x-grid and a 0.05 ms global time step with 10 intermediate time steps. Table 6.1 lists the values of the ignition location in physical space (x_{ign}), the ignition mixture

fraction (η_{ign}) and the ignition delay (t_d). The three grids predict the same x_{ign} value and comparable η_{ign} values ($\eta_{ign} = 0.015125$ is one index away from $\eta = 0.016500$ on the 125-point grid). However, the 43-point grid yields a slightly longer ignition delay while the 63 and 125-point grids predict the same value. Still, it is difficult to decide which grid is the most suitable based on the data of Table 6.1. Figure 6.1 displays the change in conditional temperature ($\Delta Q_T(t, x, \eta) = Q_T(t, x, \eta) - Q_T(0, x, \eta)$) using the three grids. Figures 6.1(a) and 6.1(b) correspond to an early time ($t = 0.25$ ms and $x = 1.50$ cm) and a late time ($t = 0.95$ ms and $x = 3.00$ cm) during the simulation, respectively. In both cases, the 43-point grid underpredicts ΔQ_T while the 63 and 125-point grids yield very close profiles. Thus, grid independence is achieved with the 63-point grid.

Table 6.1: Values of x_{ign} (cm), η_{ign} and t_d (ms) using the 43, 63 and 125-point mixture fraction grids.

Grid	x_{ign}	η_{ign}	t_d
43	3.25	0.016500	9.800
63	3.25	0.016500	9.650
125	3.25	0.015125	9.650

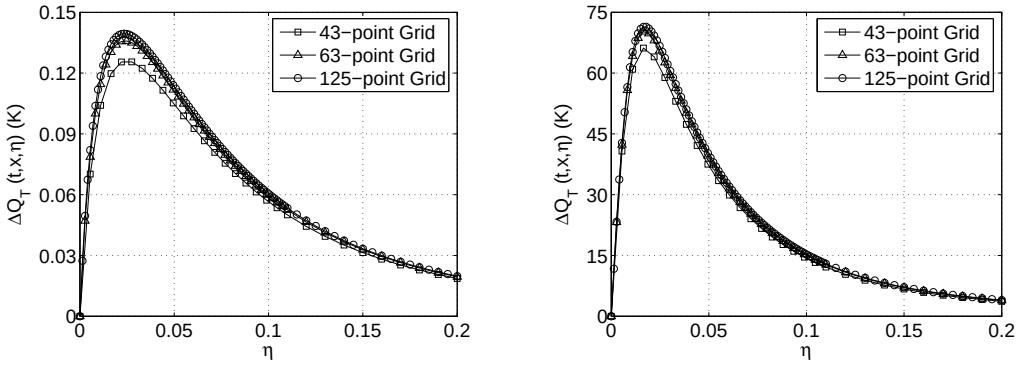

(a) (b)

Figure 6.1: Change in the conditional temperature using the 43, 63 and 125-point mixture fraction grids: (a) $t = 0.25$ ms and $x = 1.50$ cm (b) $t = 0.95$ ms and $x = 3.00$ cm.

6.1.3 Time Step: Δt

Two time steps were considered: 0.02 ms and 0.05 ms. The test case where the air temperature is equal to 1350 K was investigated using the 29-point nonuniform x-grid, the 63-point η-grid, and 10 intermediate time steps. Table 6.2 shows the values of x_{ign}, η_{ign} and t_d obtained using the two time steps. In both cases, x_{ign} and η_{ign} are identical. Still, a slightly higher ignition delay is obtained with $\Delta t = 0.02$ ms. This is explained by the fact that using a smaller time step, the solution is updated more frequently, which yields more accurate results. However, due to the dramatic increase in computational cost (the total simulation time is 8,910 min when $\Delta t = 0.02$ ms compared to 4,173 min when $\Delta t = 0.05$ ms) and in light of the satisfactory results shown in Table 6.2, the 0.05 ms time step is selected. In addition, various numbers of intermediate time steps were tested with $\Delta t = 0.05$ ms, namely 5, 10 and 20 intermediate steps. The values of x_{ign} and η_{ign} remained the same while only the decimal precision of t_d was affected, depending on the number of intermediate time steps.

Table 6.2: Values of x_{ign} (cm), η_{ign} and t_d (ms) obtained using the 0.02 and 0.05 ms time steps.

Δt	x_{ign}	η_{ign}	t_d
0.02	3.25	0.016500	0.980
0.05	3.25	0.016500	0.965

6.1.4 The Temperature Equation versus the Enthalpy-Mixture Fraction Linear Coupling Technique

Section 5.2 discussed two possible techniques for computing the conditional temperature. The first is to solve the cross-stream averaged conditional temperature equation (Eq.(5.5)). The second is to linearly couple the conserved conditional enthalpy with the mixture fraction, and then recover the conditional temperature from the conditional enthalpy by itera-

Table 6.3: Values of x_{ign} (cm), η_{ign} and t_d (ms) obtained by solving Eq.(5.5) and by the enthalpy-mixture fraction linear coupling technique.

T_{air} (K)	x_{ign}	η_{ign}	t_d
1200	5.00	0.02200	3.110
1250	4.50	0.02200	2.130
1300	4.00	0.01925	1.420
1350	3.25	0.01650	0.965
1400	2.75	0.01375	0.660

tion. As mentioned earlier, this technique is attractive because it prevents the occurrence the errors that might be introduced by the discretization of Eq.(5.5) and due to the fact that it reduces the computational cost. It is of great importance to show that both of them yield the same results. Air temperatures ranging from 1200 K to 1400 K are considered. The 29-point nonuniform x-grid, the 63-point η-grid and the 0.05 ms time step (with 10 intermediate time steps) are used in the simulations. For all air temperatures, the values of x_{ign}, η_{ign} and t_d are identical (Table 6.3). Figure 6.2 shows the variation of the difference $Q_{T,LC}(t,x,\eta) - Q_{T,TE}(t,x,\eta)$ with axial position at $t = 1.4$ ms for an air temperature of 1300 K, $Q_{T,LC}$ and $Q_{T,TE}$ being the values of the conditional temperature computed by linear coupling (LC) and by solving the temperature equation (TE), respectively. It can be seen that the difference in the predicted conditional temperature is negligible. In all the subsequent CMC calculations the linear coupling technique is used.

6.2 Homogeneous CMC Calculations

As a first step, homogeneous CMC calculations are performed, i.e. spatial dependence is not accounted for while solving the CMC equations. However, the turbulent velocity and mixing fields computations do account for inhomogeneities in the flow. The objective is to investigate the role of spatial transport in the ignition mechanism. A detailed discussion will be presented in Section 6.3. Here, the spatial transport terms are not included in the

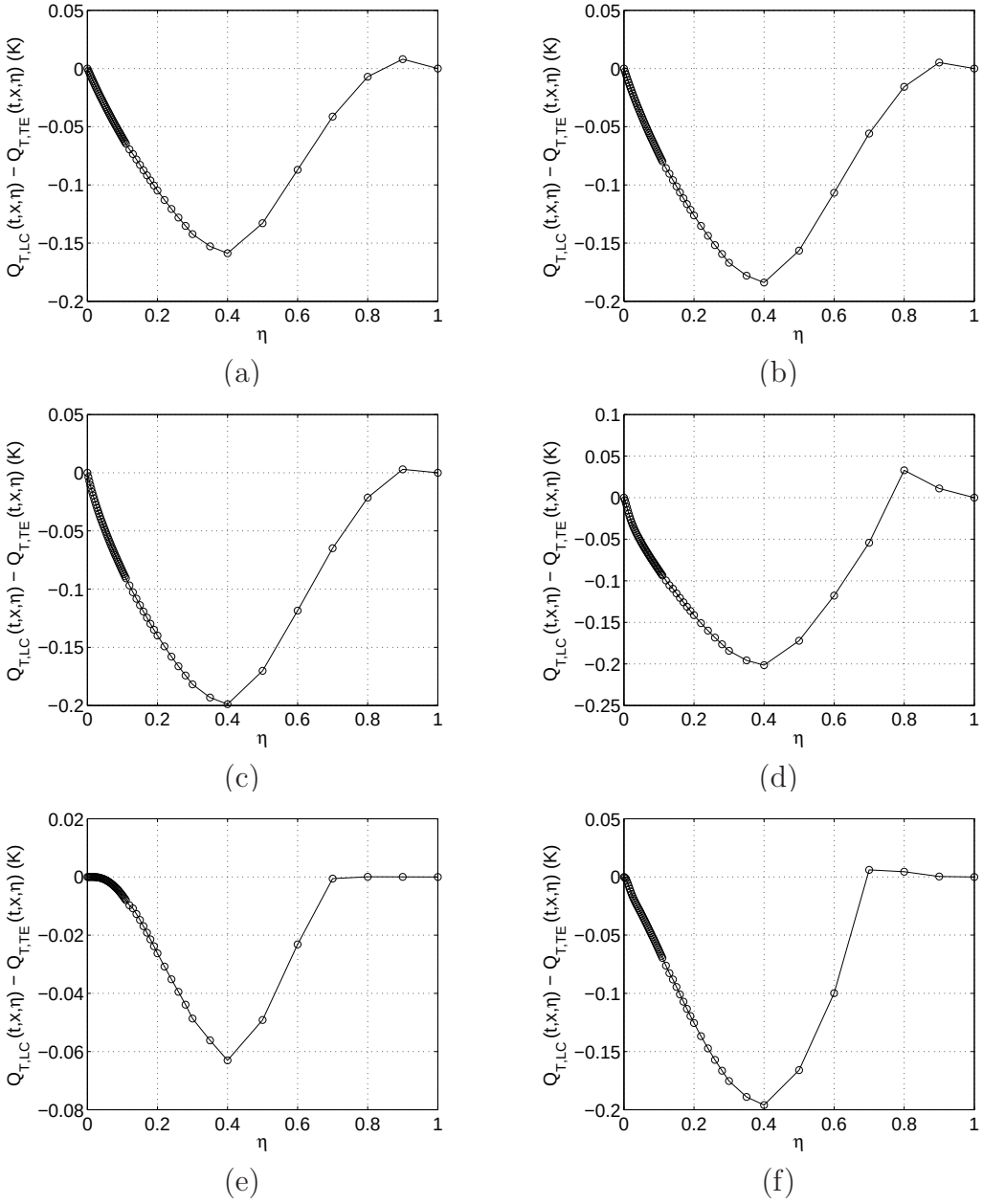

Figure 6.2: Variation of the difference $Q_{T,LC}(t,x,\eta) - Q_{T,TE}(t,x,\eta)$ with axial position at $t = 1.4$ ms for an air temperature of 1300 K: (a) $x = 0.50$ cm, (b) $x = 1.00$ cm, (c) $x = 2.00$ cm, (d) $x = 3.00$ cm, (e) $x = 4.00$ cm, and (f) $x = 5.00$ cm.

CMC equations while the transient term, micro-mixing and the chemical source are kept. Accordingly, the cross-stream averaged species transport equation reduces to:

$$\underbrace{\frac{\partial Q_\alpha}{\partial t}}_{\text{transient term}} = \underbrace{\frac{1}{2}\{\langle\chi|\eta\rangle\}_{R^+}\frac{\partial^2 Q_\alpha}{\partial \eta^2}}_{\text{micro-mixing term}} + \underbrace{\frac{\langle\dot{\omega}_\alpha|\eta\rangle}{\langle\rho|\eta\rangle}}_{\text{chemical source}} \tag{6.1}$$

Hereafter, this set of calculations is referred to as Series I. Both scalar dissipation models discussed in Section 3.3.3 (the AMC model and Girimaji's model) are separately implemented to determine $\langle\chi|\eta\rangle$. The predicted ignition delays are compared with the experimental data of Sullivan et al. [113] in Figure 6.3. The results show very good agreement with the experimental data and the trend of increasing ignition delay for decreasing air temperature is well reproduced. Both scalar dissipation models yield comparable ignition delays, with the AMC model predicting ignition slightly earlier. Table 6.4 provides further details on x_{ign}, η_{ign}, t_d and the value of the cross-stream averaged scalar dissipation rate at the ignition point, $\{\langle\chi|\eta\rangle\}_{R^+,ign}$. It can be seen that x_{ign} increases with decreasing air temperature and remains above 25 (nozzle) diameters away from the fuel inlet. In contrast, $\{\langle\chi|\eta\rangle\}_{R^+,ign}$ decreases with decreasing air temperature. This is explained by the fact that chemical activity is larger at higher temperatures and can compete with more intense turbulent mixing, thus ignition occurs earlier. Generally, for a given air temperature, $\{\langle\chi|\eta\rangle\}_{R^+,ign}$ predicted using Girimaji's model is slightly higher than the value obtained using the AMC model. In all cases, ignition always occurs at low scalar dissipation rates and in fuel-lean mixtures in mixture fraction space (around 0.02).

6.3 Inhomogeneous CMC Calculations

The previous section presented the ignition delay results using the homogeneous form of the CMC equations. In this section, the spatial transport terms are included, i.e. Eq.(6.2)

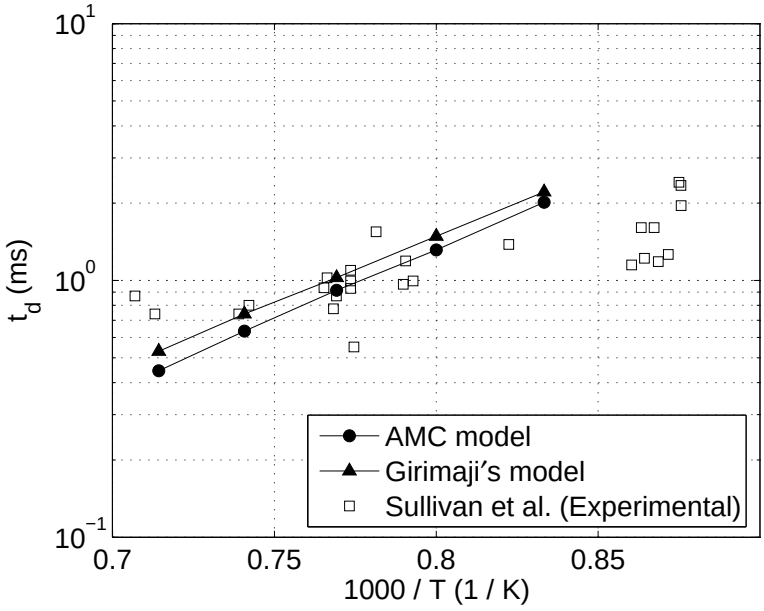

Figure 6.3: Comparison of the ignition delay results using the homogeneous CMC equations (Eq.(6.1)) with the experimental data of Sullivan et al. [113].

Table 6.4: Values of x_{ign} (cm), η_{ign}, t_d (ms) and $\{\langle\chi|\eta_{ign}\rangle\}_{R^+}$ (s^{-1}) obtained using Eq.(6.1).

	AMC Model				Girimaji's Model			
T_{air} (K)	x_{ign}	η_{ign}	t_d	$\{\langle\chi\|\eta_{ign}\rangle\}_{R^+}$	x_{ign}	η_{ign}	t_d	$\{\langle\chi\|\eta_{ign}\rangle\}_{R^+}$
1200	4.00	0.02475	2.015	1.894	4.50	0.02750	2.210	1.769
1250	3.75	0.02475	1.315	2.733	3.75	0.03025	1.485	5.001
1300	3.50	0.02200	0.915	2.830	3.50	0.02475	1.025	5.293
1350	2.75	0.01650	0.635	3.449	3.00	0.01925	0.740	5.115
1400	2.25	0.01650	0.445	6.032	2.75	0.01650	0.530	5.744

$$\underbrace{\frac{\partial Q_\alpha}{\partial t}}_{\text{transient term}} = \underbrace{\frac{1}{2}\{\langle\chi|\eta\rangle\}_{R^+}\frac{\partial^2 Q_\alpha}{\partial \eta^2}}_{\text{micro-mixing term}} + \underbrace{\frac{\langle\dot{\omega}_\alpha|\eta\rangle}{\langle\rho|\eta\rangle}}_{\text{chemical source}}$$
$$\underbrace{-\left[\{\langle u_x|\eta\rangle\}_{R^+} - \left\{\frac{D_t}{\langle\rho\rangle\tilde{P}(\eta)}\frac{\partial(\langle\rho\rangle\tilde{P}(\eta))}{\partial x}\right\}_{R^+} - \left\{\frac{\partial D_t}{\partial x}\right\}_{R^+}\right]\frac{\partial Q_\alpha}{\partial x} + \{D_t\}_{R^+}\frac{\partial^2 Q_\alpha}{\partial x^2}}_{\text{spatial transport}} \tag{6.2}$$

is solved. This set of calculations shall be referred to as Series II. Similar to Section 6.2, the AMC model and Girimaji's model are both tested. The predicted ignition delays are displayed in Figure 6.4 along with the results of Series I and the experimental data of Sullivan et al. [113]. The results show good agreement with the experimental data for high air temperatures, however an overprediction is obtained at lower temperatures. Figure 6.5 shows the variation of the ignition location from Series I and II with air temperature using the AMC model. The results of both series fall successfully within the experimental scatter. The values of x_{ign}, η_{ign}, t_d and $\{\langle\chi|\eta_{ign}\rangle\}_{R^+}$ are included in Table 6.5. The trends observed in the homogeneous calculations are again obtained here. t_d and x_{ign} decrease with increasing air temperature while $\{\langle\chi|\eta_{ign}\rangle\}_{R^+}$ shows an opposite trend. In all cases, Girimaji's model results in higher $\{\langle\chi|\eta_{ign}\rangle\}_{R^+}$ and slightly longer ignition delays than the AMC model and ignition occurs in fuel-lean mixtures in mixture fraction space (around 0.02).

Comparison of Series I and II clearly indicates that spatial transport increases ignition delay. This observation can be explained by the fact that in the absence of spatial transport, the species are not convected and their concentrations build up locally with time at a faster rate via micro-mixing and chemical reactions. Since the temperature is a function of the species concentrations, a larger temperature increase is expected to occur locally in a shorter period of time. This behavior can be also seen by inspecting the ignition locations in Figure 6.5: for all temperatures, ignition occurs further downstream when spatial transport is included. Wright et al. [123] also noted the significant role of spatial transport in their calculations but observed an opposite effect on ignition delay. This difference may originate from the fact that different operating and boundary conditions were used in their simulations.

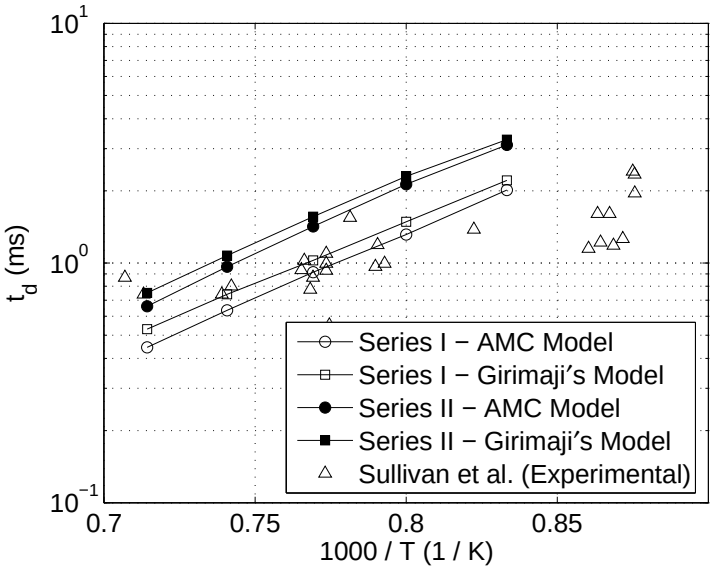

Figure 6.4: Comparison of the ignition delay of Series II with the results of Series I and the experimental data of Sullivan et al. [113].

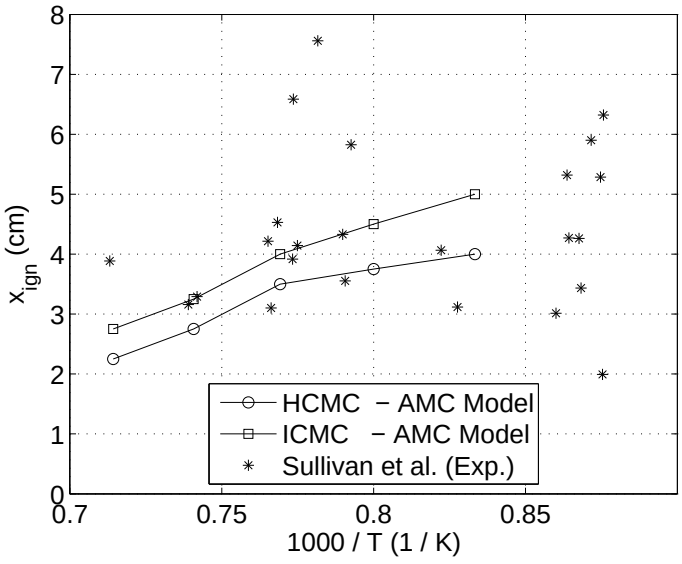

Figure 6.5: Comparison of the ignition location with the experimental data of Sullivan et al. [113].

Table 6.5: x_{ign} (cm), η_{ign}, t_d (ms) and $\{\langle\chi|\eta_{ign}\rangle\}_{R^+}$ (s^{-1}) obtained using Eq.(6.2).

	AMC Model				Girimaji's Model			
T_{air} (K)	x_{ign}	η_{ign}	t_d	$\{\langle\chi\|\eta_{ign}\rangle\}_{R^+}$	x_{ign}	η_{ign}	t_d	$\{\langle\chi\|\eta_{ign}\rangle\}_{R^+}$
1200	5.00	0.02200	3.110	0.259	5.00	0.02200	3.270	0.258
1250	4.50	0.02200	2.130	1.112	4.50	0.02200	2.300	1.131
1300	4.00	0.01925	1.420	1.555	4.00	0.02200	1.560	2.692
1350	3.25	0.01650	0.965	2.152	3.50	0.01650	1.075	2.575
1400	2.75	0.01375	0.660	2.594	3.00	0.01650	0.750	4.183

Figure 6.6 displays the temporal variation of the change in the cross-stream averaged conditional temperature, $\Delta Q_T(t,x,\eta) = Q_T(t,x,\eta) - Q_T(0,x,\eta)$, at various axial locations. For illustration, the test case from Series II where the AMC model is used and $T_{air} = 1300$ K is considered. For this specific case, ignition occurs at $t = 1.42$ ms and $x = 4.00$ cm (about 36 nozzle diameters from the inlet). Figure 6.6(a) ($t = 0.25$ ms) shows that the temperature starts to increase in the inlet area (up to $x = 2.5$ cm) while the downstream locations do not experience any changes. This is due to the fact that at this early time, these locations have not been reached by the methane jet (refer to the mixture fraction radial profiles in Figure 4.8(a)). The temperature starts to increase at such locations at later times as can be seen in Figure 6.6(b) ($t = 0.50$ ms). The increase becomes more apparent starting $t = 0.75$ ms (Figure 6.6(c)) where a maximum change of 4.5 K is reached at $x = 3.00$ cm. As time elapses, the temperature build-up becomes much more significant, especially around the ignition location. This can be clearly seen in Figures 6.6(d), (e) and (f) ($t = 1.00, 1.25$ and 1.42 ms, respectively). When $\Delta\{\langle T(t,x,\eta)\rangle\}_{R^+} = 75$ K is reached ignition is declared. In the current test case, this occurs at $x = 4.00$ cm in Figure 6.6(f).

The concentrations of the major species at the ignition location are shown in Figure 6.7. As expected, the conditional concentrations of methane (CH_4) and dioxygen (O_2) have decreased while water (H_2O), carbon monoxide (CO), carbon dioxide (CO_2), formaldehyde (CH_2O), ethene (C_2H_4) and ethane (C_2H_6) concentrations have increased. The emergence of CH_2O occurs early during the simulation as a result of oxidization of methyl (CH_3) radi-

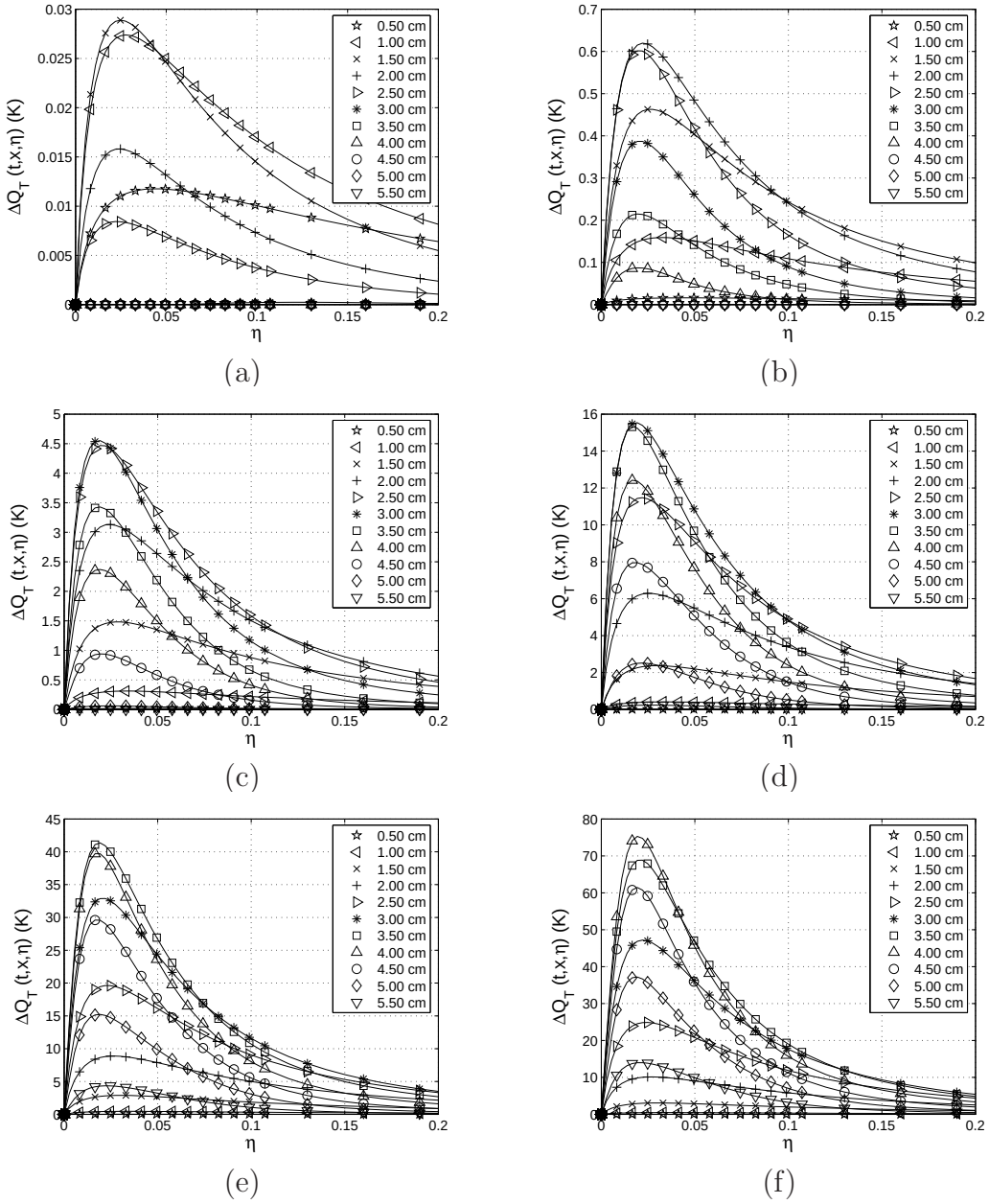

Figure 6.6: Temporal variation of the cross-stream averaged conditional temperature at various axial locations for $T_{air} = 1300$ K (Series II): (a) $t = 0.25$ ms, (b) $t = 0.50$ ms, (c) $t = 0.75$ ms, (d) $t = 1.00$ ms, (e) $t = 1.25$ ms, and (f) $t = 1.42$ ms (ignition time).

cals (Figure 6.7(a)). CH_3 is produced via different initiation and decomposition reactions involving CH_4 and from the abstraction of hydrogen (H) from CH_4 itself. The rise in the concentrations of C_2H_6 and C_2H_4 takes place at a later stage (Figure 6.7b) through a set of CH_3 recombination reactions. C_2H_4 is also produced by by the oxidation of ethyl (C_2H_5) radicals, which are in turn produced during the oxidation of C_2H_6. This explains why the emergence of C_2H_4 does not occur as early as C_2H_6. CO_2 production occurs through the oxidation of CO by O, O_2, OH and HO_2 through the chemical reactions

$$CO + O + M \rightleftarrows CO_2 + M \tag{6.3a}$$

$$CO + O_2 \rightleftarrows CO_2 + O \tag{6.3b}$$

$$CO + OH \rightleftarrows CO_2 + H \tag{6.3c}$$

$$CO + HO_2 \rightleftarrows CO_2 + OH \tag{6.3d}$$

where M is a catalyst. The rate of formation of *CO* via reactions (6.3a) and (6.3b) is small compared to reactions (6.3c) and (6.3d) [66]. Furthermore, in the presence of hydrogen atoms, the oxidation of CO radicals becomes strongly coupled with that of hydrogen peroxide (H_2O_2) [14], making reactions (6.3c) and (6.3d) more competitive. However, the low CO_2 concentration compared to the relatively higher CO radical concentration is explained by the fact that the reactions above are inhibited by the presence of CH_4. Furthermore, the complete oxidization of CO requires a substantial rise in temperature. At the ignition time (Figure 6.7(e)), the temperature rise is equal to 75 K at most which is insufficient for complete oxidization. Figure 6.7(e) shows that at $t = 1.775$ ms, the CO_2 concentration becomes more significant. The maximum temperature rise at this time is around 400 K (not shown).

6.3.1 Balance in the CMC Equation

As shown in Eq.(6.2), the CMC equation can be expressed as a balance between the transient term and the micro-mixing, chemical, and spatial transport terms. By separately plotting the RHS terms of Eq.(6.2), it is possible to measure the contribution of each term to the balance of the CMC equation. The test case where the air temperature is equal to 1300 K and the AMC model is used for the conditional scalar dissipation rate

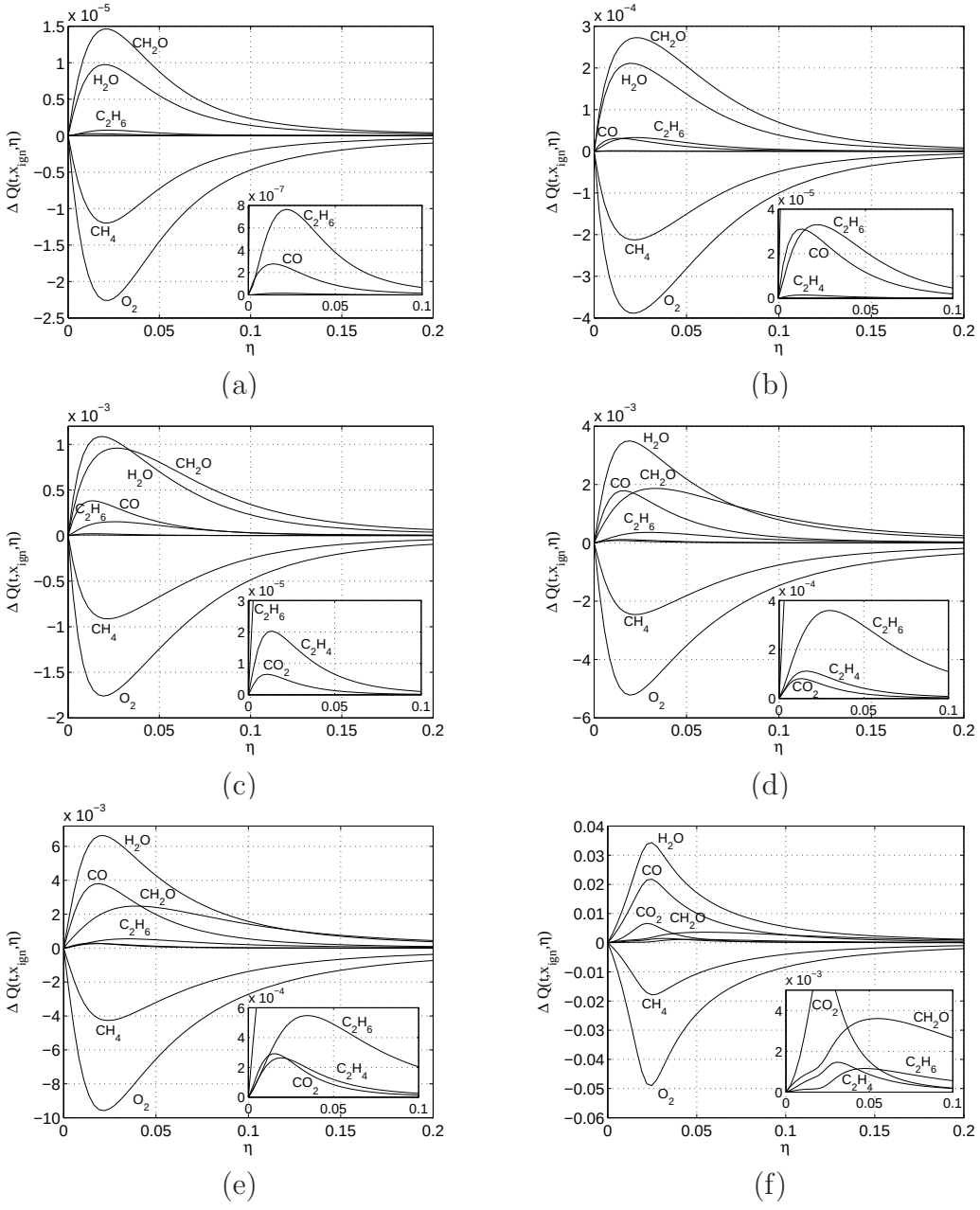

Figure 6.7: Concentration of the major species for $T_{air} = 1300$ K: (a) $t = 0.50$ ms, (b) $t = 0.75$ ms, (c) $t = 1.00$ ms, (d) $t = 1.25$ ms, (e) $t = 1.42$ ms (ignition time), and (f) $t = 1.775$ ms.

is considered, and CH_4 is chosen since it is one of the major species in the mixture. The contributions of the micro-mixing, chemical source and spatial transport terms are plotted in Figure 6.8 at $x = x_{ign} = 4.00$ cm for different simulation times. As a first observation, the contribution of the chemical source term is the largest at all times. At early times, the contribution of the spatial transport term is considerable compared to micro-mixing as shown for example in Figure 6.8(a) ($t = 0.50$ ms). Inspection of Figures 6.8(b) to 6.8(f) shows that micro-mixing dominates at later times. However, the role of spatial transport remains important. Figure 6.9 displays the axial variation of the RHS terms of Eq.(6.2) at $t = t_{ign} = 1.42$ ms. As expected, the effect of physical transport is significant close to the inlet over a wide range of the mixture fraction space. This is due to the strong effect of convection in the inlet area. Further, the contributions of the micro-mixing and the chemical source terms are comparable. These trends are shown in Figures 6.9(a)-6.9(d). Further downstream, the contribution of spatial transport diminishes (due to the weaker effect of convection) while the roles of the micro-mixing and the chemical source terms become much more significant. However, the contributions of the last two terms are not comparable in magnitude. It can be clearly seen that chemistry dominates over micro-mixing (Figures 6.9(e) and 6.9(f)). This can be explained by the fact that self-heating via chemical reactions takes place downstream, which accelerates the rates of reactions. Overall, Figures 6.8 and 6.9 suggest that all the RHS terms of Eq.(6.2) are significant with variable importance, depending on time and location in physical space.

6.3.2 UBC-Mech 1.0 and GRI-Mech 3.0

Section 5.7 presented some of the chemical kinetics mechanism developed earlier for the combustion of methane and natural gas. So far, UBC-Mech 1.0 [49] has been used in all of the previous sections. In this section, another set of calculations is performed using GRI-Mech 3.0 [107]. All the terms in the CMC equations are accounted for, i.e. Eq.(6.2) is solved. Air temperatures ranging between 1250 K and 1400 K are considered and both scalar dissipation models are implemented to compute the conditional scalar dissipation rate. Figure 6.10 and Table 6.6 present the predicted ignition delays using the two different chemical mechanisms. The results of GRI-Mech 3.0 are very close to those of the UBC-Mech 1.0 for air temperatures greater than 1350K (within 5%). At lower air temperatures,

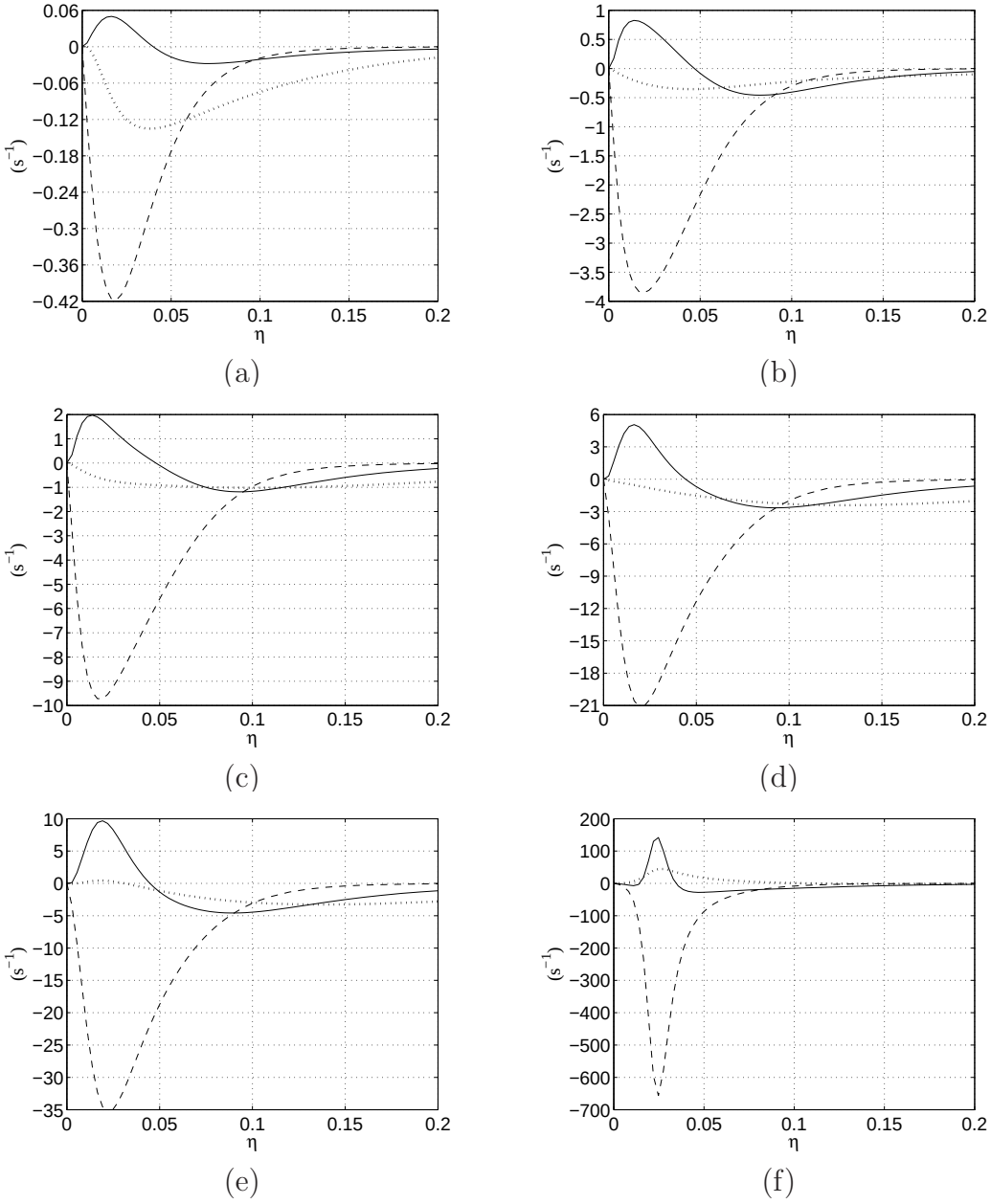

Figure 6.8: Balance of Eq.(6.2) for $T_{air} = 1300$ K at $x = x_{ign} = 4.00$ cm: $\cdots$ spatial transport, - - - chemistry, and —— micro-mixing. (a) $t = 0.50$ ms, (b) $t = 0.75$ ms,(c) $t = 1.00$ ms, (d) $t = 1.25$ ms, (e) $t = 1.42$ ms (ignition time), and (f) $t = 1.775$ ms.

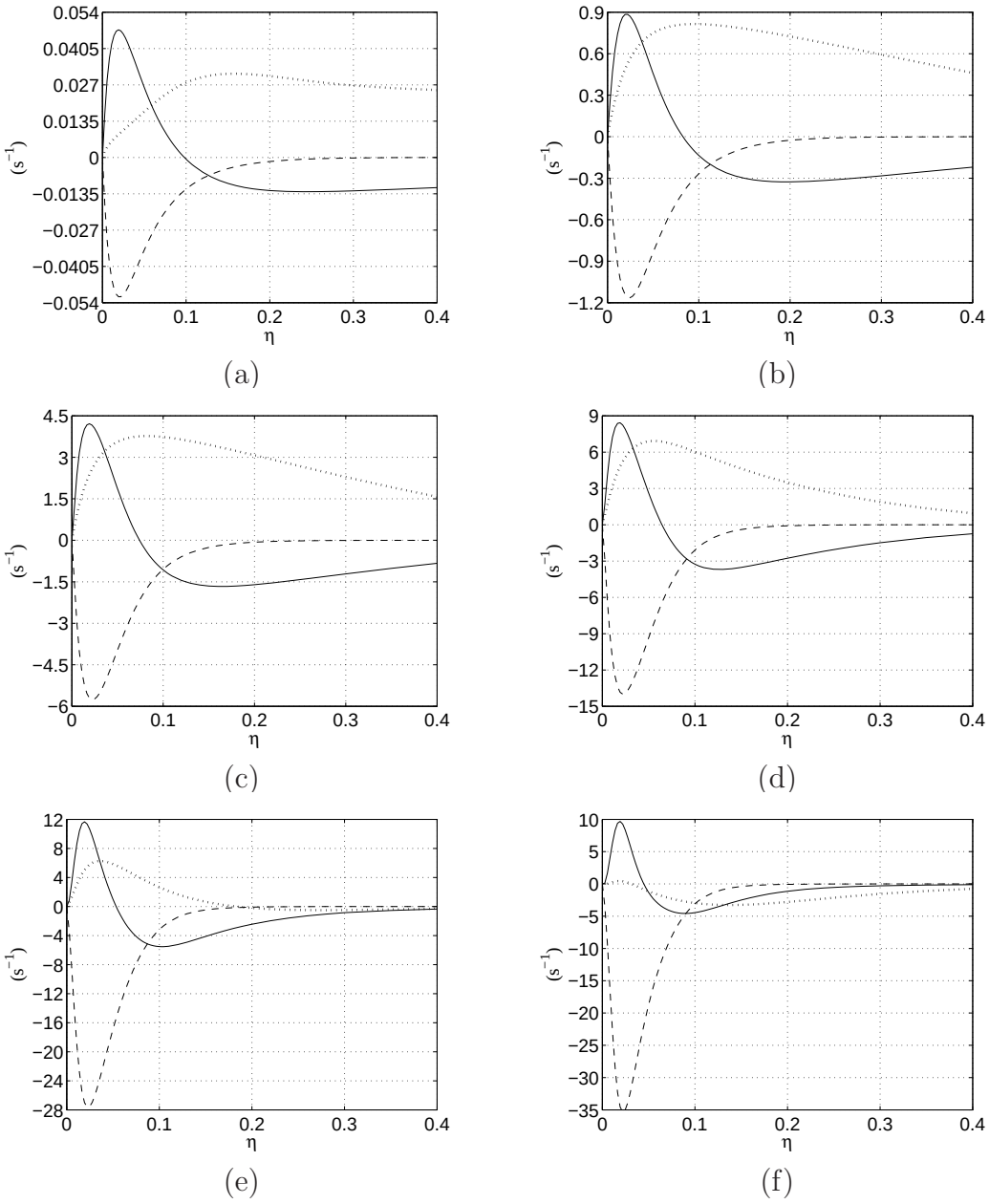

Figure 6.9: Balance of Eq.(6.2) for $T_{air} = 1300$ K at $t = t_d = 1.42$ ms: $\cdots$ physical transport, - - - chemistry, and —— micro-mixing. (a) $x = 0.25$ cm, (b) $x = 1.00$ cm,(c) $x = 1.75$ cm, (d) $x = 2.50$ cm, (e) $x = 3.25$ cm, and (f) $x = 4.00$ cm (ignition Location).

Table 6.6: Comparison of t_d (ms) using UBC-Mech 1.0 [49] and GRI-Mech 3.0 [107].

	AMC Model		Girimaji's Model	
T_{air} (K)	UBC-Mech 1.0	GRI-Mech 3.0	UBC-Mech 1.0	GRI-Mech 3.0
1250	2.130	2.745	2.300	3.200
1300	1.420	1.635	1.560	1.875
1350	0.965	1.015	1.075	1.155
1400	0.660	0.655	0.750	0.750

some differences appear. For example, for an air temperature of 1300 K, GRI-Mech 3.0 overpredicts the UBC-Mech 1.0 ignition delay by 15% when the AMC model is used and by 20% when Girimaji's model is used. Both mechanisms include a large number of species and steps. However, UBCMech has been optimized for low air temperatures and high pressures [49]. Thus, it is expected to perform better in the present autoignition conditions.

6.3.3 Other Ignition Criteria

At this stage, it is important to investigate other ignition criteria used in the literature. One commonly used criterion to determine ignition is to define t_d as the time required to reach a temperature of 2000 K anywhere in the computational domain. This criterion was previously used by Bi et al. [5], Kim et al. [57] and Frisque et al. [34]. Huang et al. [48] used another criterion based on the maximum rate of change of the maximum temperature. t_d is determined by plotting the maximum mean temperature as a function of time, then by extrapolating the maximum slope of the temperature history back to the level at the beginning of injection. Physically, this criterion represents the maximum rate of heat release that signals the ignition of the mixture. Other criteria involve a certain increase in the mean pressure or the consumption of a specific mass of the fuel as in Agarwal et al. [1], Naber et al. [83] and Huang et al. [48]. The first two criteria described above are tested for three air temperatures, namely 1300, 1350 and 1400 K. In all cases the AMC model is used.

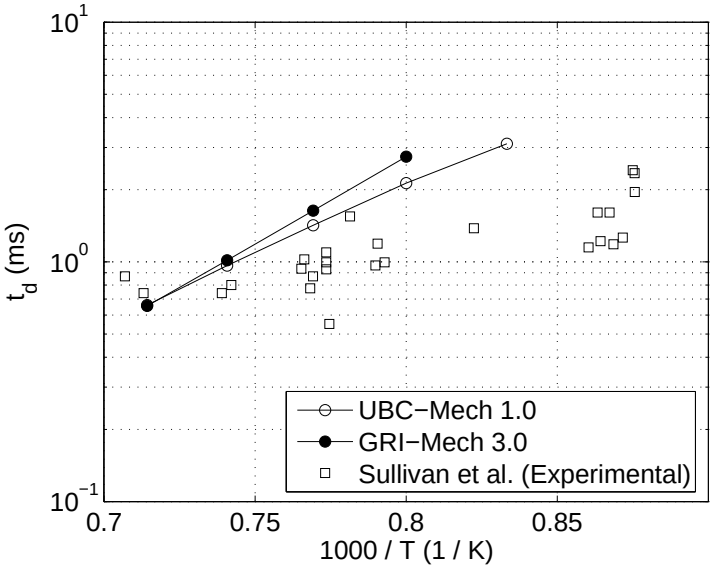

(a)

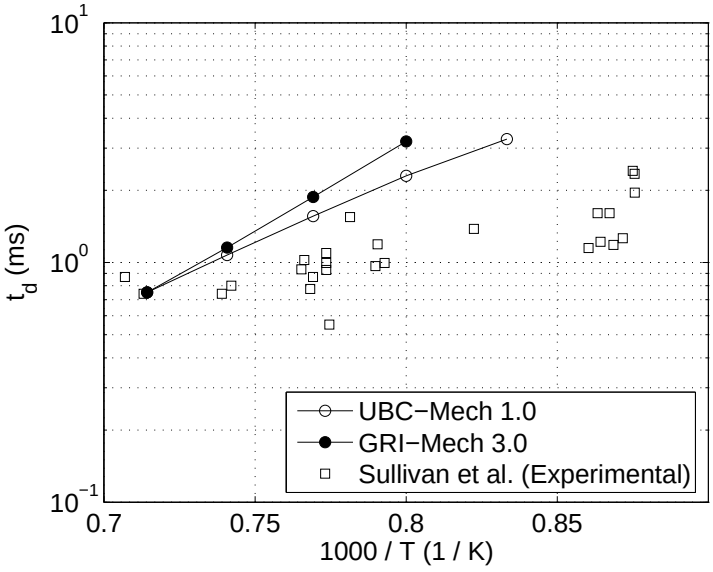

(b)

Figure 6.10: Ignition delay using GRI-Mech 3.0 [107]: (a) AMC model and (b) Girimaji's model.

Figure 6.11 shows the time variation of conditional temperature at the ignition location ($Q_T(t, x_{ign}, \eta)$). In the simulations, ignition is declared whenever $Q_T(t, x, \eta)$ reaches 2000 K anywhere in physical or mixture fraction spaces. Inspection of the curves corresponding to the global time steps just before and after ignition (solid lines) shows a substantial temperature rise accompanied by a clear shift toward the stoichiometric mixture fraction value $\eta_{st} = 0.055$. This corresponds to the sudden heat release that follows the ignition of the mixture.

Figure 6.12 displays the variation of the maximum conditional temperature with time ($Q_{T,max}(t, x, \eta)$). First, the rate of change of $Q_{T,max}$, $dQ_{T,max}/dt$, is determined at each time step (global and intermediate) using 4^{th} order central differencing. Afterward, the maximum slope is extrapolated back to the level of the initial air temperature at the onset of injection ($T = T_{air}$). Ignition delay is determined by projecting the intersection point of the line $Q_{T,max} = T_{air}$ with the extrapolated slope on the time axis.

Table 6.7 lists the values of t_d, η_{ign}, x_{ign} and $\{\langle\chi|\eta_{ign}\rangle\}_{R^+}$ for the different ignition criteria implemented so far. For clarity, the criteria $\Delta Q_T(t, x, \eta) = 75$ K , $Q_T(t, x, \eta) = 2000$ K, and $[dQ_{T,max}(t, x, \eta)/dt]_{max}$ are designated by C1, C2 and C3, respectively. It can be seen from Table 6.7(a) that for all air temperatures, criteria C2 and C3 yield comparable ignition delays. However, t_d obtained using criterion C1 remains smaller in all cases. This is an expected result since criteria C2 and C3 require higher temperatures in order to be met, which in turn requires a longer duration to be achieved. As a consequence, the values of η_{ign} and $\{\langle\chi|\eta_{ign}\rangle\}_{R^+}$ are higher, as shown in Tables 6.7(b) and 6.7(d), respectively. On the other hand, Table 6.7(c) shows that the different criteria result in comparable x_{ign} values.

Finally, it is interesting to revisit criterion C1 but this time restrict the 75 K temperature increase to physical spaces. Although the CMC equations are cross-stream averaged and solved in one dimension, it is possible to obtain the Favre-averaged temperatures in two dimensions (x, r) using

$$\widetilde{T}(t, x, r) = \int_0^1 Q_T(t, x, \eta)\tilde{P}(t, x, r, \eta)\ d\eta, \tag{6.4}$$

where the Favre-averaged temperature, $\widetilde{T}$, is calculated by integrating the product of the conditional temperature and PDF over the mixture fraction space. The test case where

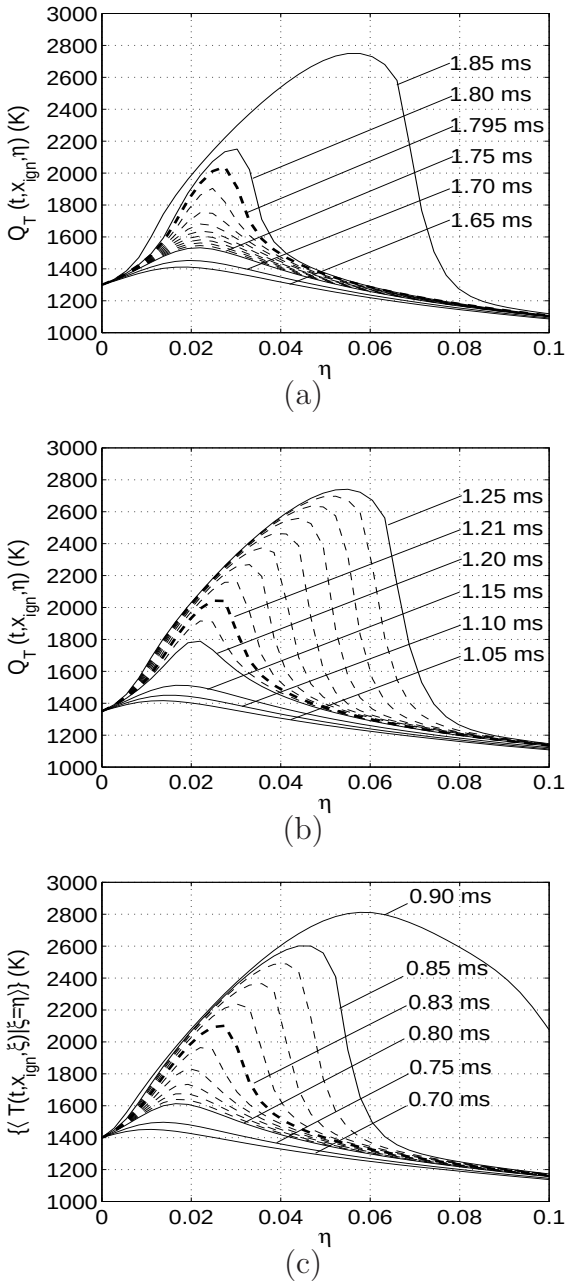

Figure 6.11: Ignition delay using the 2000 K criterion: —— global time step, - - - intermediate time step, and **- - -** ignition time. (a) $T_{air} = 1300$ K, (b) $T_{air} = 1350$ K, and (c) $T_{air} = 1400$ K.

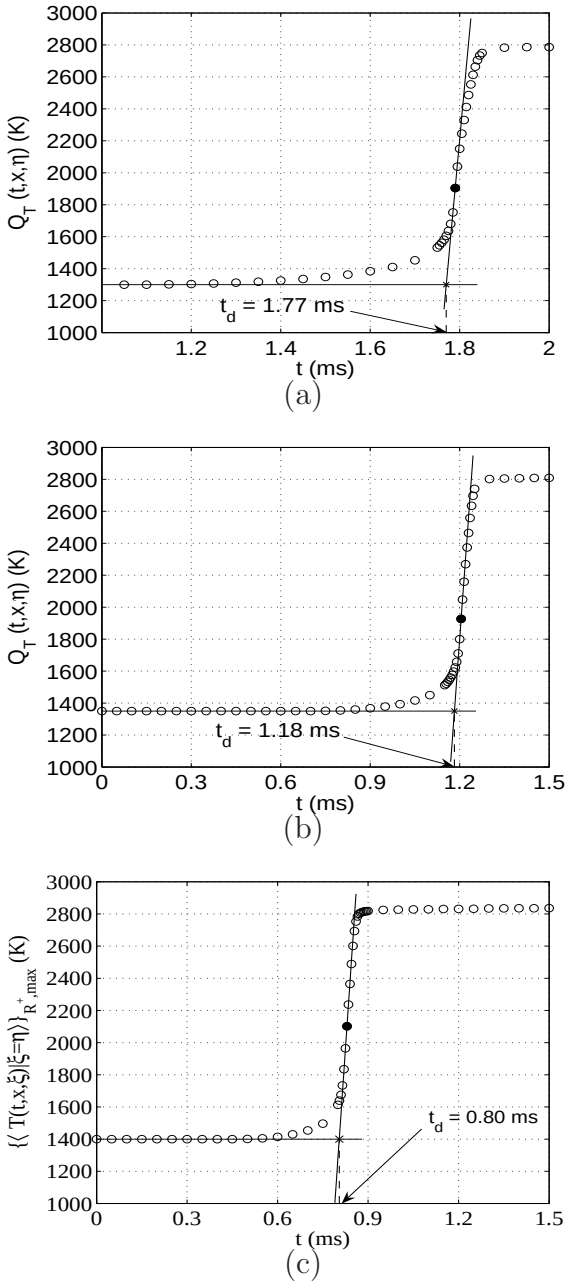

Figure 6.12: Ignition delay using the maximum slope criterion: (○) instantaneous maximum conditional temperature, (●) maximum conditional temperature having maximum slope. (a) $T_{air} = 1300$ K, (b) $T_{air} = 1350$ K, and (c) $T_{air} = 1400$ K.

Table 6.7: Comparison of the ignition results using different ignition criteria. The AMC model is used. Criteria: C1: $\Delta\{\langle T(t,x,\xi)|\xi=\eta\rangle\}_{R^+} = 75$ K (Series II), C2: $\{\langle T(t,x,\xi)|\xi=\eta\rangle\}_{R^+} = 2000$ K, and C3 :$[d\{\langle T(t,x,\xi)|\xi=\eta\rangle\}_{R^+,max}/dt]_{max}$.

(a) t_d (ms)

T(K)	C1	C2	C3
1300	1.420	1.795	1.770
1350	0.965	1.210	1.180
1400	0.660	0.800	0.800

(b) η_{ign}

T(K)	C1	C2	C3
1300	0.01925	0.02475	0.02475
1350	0.01650	0.02475	0.02200
1400	0.01375	0.02200	0.02750

(c) x_{ign} (cm)

T(K)	C1	C2	C3
1300	4.00	3.50	4.00
1350	3.25	3.50	3.75
1400	2.75	3.00	3.00

(d) $\{\langle\chi|\eta_{ign}\rangle\}_{R^+}$ (s^{-1})

T(K)	C1	C2	C3
1300	1.555	3.398	2.423
1350	2.152	3.521	2.372
1400	2.594	4.508	10.07

the air temperature is equal to 1300 K is considered. The inhomogeneous CMC equation (Eq.(6.2)) is solved and $\langle\chi|\eta\rangle$ is modeled using the AMC model. The temporal variation of the Favre-averaged temperatures relative the initial temperatures in the spatial domain at $x = 3.75$ cm is shown in Figure 6.13(a). As expected, the Favre-averaged temperatures rise with time and the peaks of the temperature profiles move gradually to larger radial distances, following the position of the jet shear layer. According to the new criterion, the ignition point in this figure is located at an axial distance equal to 3.75 cm and a radial distance of approximately 0.51 cm. The new ignition delay based on the Favre-averaged temperatures is found to be 1.44 ms compared to 1.42 ms based on the conditional temperatures (see Table 6.5). Thus, the ignition criterion based on conditional or Favre-averaged temperatures provides comparable values of ignition delay. Figure 6.13(b) presents the mixture fraction contours at $t = 1.44$ ms. It can be seen that the ignition point is situated in the shear layer of the jet close to the stoichiometric mixture fraction value (0.055).

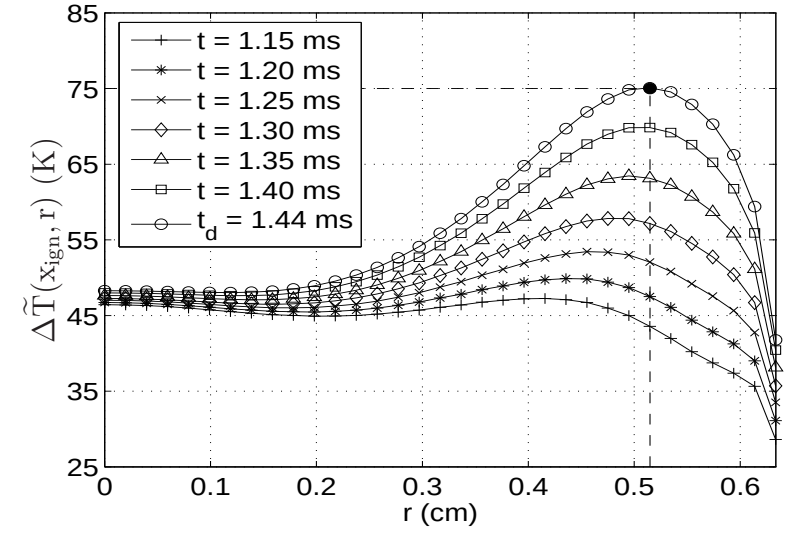

(a)

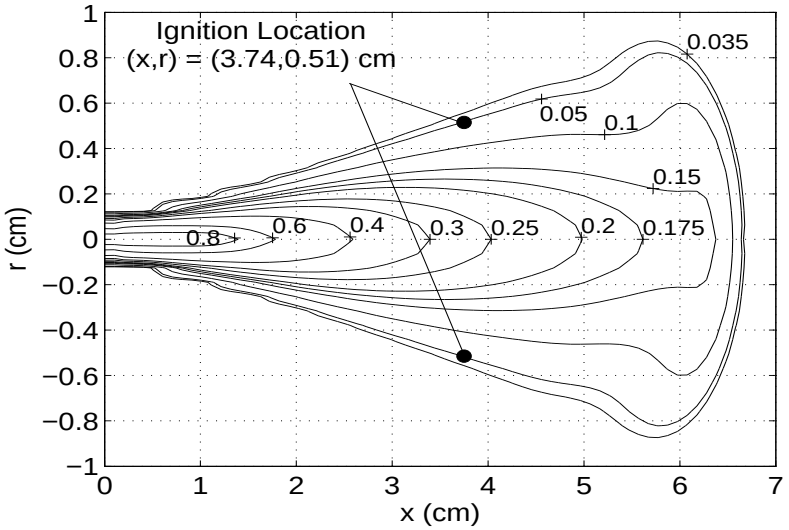

(b)

Figure 6.13: Ignition delay in physical space using the $\Delta\widetilde{T}(t,x,r) = 75$ K criterion for $T_{\text{air}} = 1300$ K (the AMC model is used). (a) $\Delta\widetilde{T}(t,x_{ign},r)$ (b) Mixture fraction contours at $t = t_{ign} = 1.44$ ms

6.4 Ignition Limit

The ignition limit is investigated in terms of the critical scalar dissipation rate above which ignition cannot occur. For this purpose, the AMC model discussed in Section 3.3.3 is invoked. The conditional scalar dissipation rate expression is given by

$$\langle \chi | \, \eta \rangle = \langle \chi | \xi = 0.5 \rangle G(\eta), \tag{6.5}$$

where $G(\eta) = \exp\{-2[\mathrm{erf}^{-1}(2\eta - 1)]^2\}$ and erf^{-1} is the inverse error function. It was previously demonstrated in Section 3.3.3 how the constant $\langle \chi | \xi = 0.5 \rangle$ is computed by weighting Eq.(6.5) with $\tilde{P}(\eta)$ and integrating the resulting expression over the mixture fraction space. However, in order to control the mixing rate, this technique is not followed, but rather a fixed value χ_o is assigned to $\langle \chi | \xi = 0.5 \rangle$, such that

$$\langle \chi | \, \eta \rangle = \chi_o G(\eta). \tag{6.6}$$

The objective is to monitor the trend of ignition delay with increasing χ_o. To do so, a series of calculations is performed for each air temperature. In each simulation, χ_o is specified and Eq.(6.1) (homogeneous CMC with the $\Delta\{\langle T(t, x, \xi) | \xi = \eta \rangle\}_{R^+} = 75$ K criterion) is solved in order to obtain the corresponding ignition delay value. The only parameter that changes from one simulation to another is the value of χ_o. This procedure is repeated for all air temperatures. The results are shown in Figure 6.14. In all cases, ignition delay increases gradually with χ_o. Furthermore, each of the curves shows an asymptotic behavior about a certain value of χ_o, meaning that ignition becomes harder to achieve. This value of χ_o is chosen to be the limiting scalar dissipation rate. However, this choice is arbitrary. One way to determine the limiting value at a given air temperature is to locate the ignition delay value from Series I (homogeneous CMC with the AMC model) on Figure 6.14, such that the corresponding χ_o value is chosen to be the limiting one ($\chi_{o,lim}$). The corresponding mixture fraction value, $\eta_{ign,lim}$, is determined in a similar fashion (not shown). Table 6.8 shows the values of $\eta_{ign,lim}$, $\chi_{o,lim}$, the limiting scalar dissipation rate computed from Eq.(6.6) at the limiting ignition mixture fraction value, $\langle \chi | \eta \rangle_{lim} = \chi_{o,lim} G(\eta_{ign,lim})$, along with with $\{\langle \chi | \eta_{ign} \rangle\}_{R^+}$ from Series I and II (both using the AMC model). Figure 6.15 shows that $\langle \chi | \eta \rangle_{lim}$ increases with air temperature. This means that mixtures with high initial air temperatures have a relatively higher chance to ignite than mixtures with lower

temperatures. Furthermore, $\{\langle\chi|\eta_{ign}\rangle\}_{R^+}$ from Series I and II is much smaller than $\langle\chi|\eta\rangle_{lim}$ for all air temperatures.

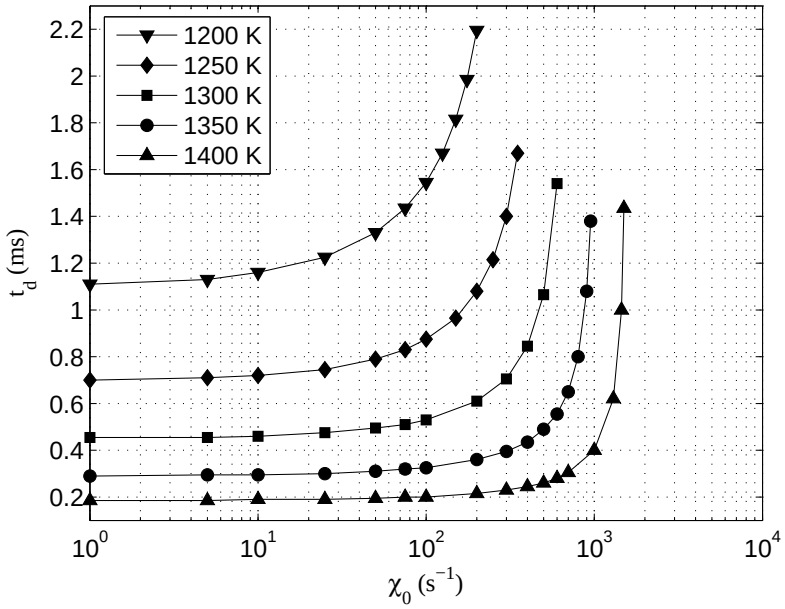

Figure 6.14: Variation of ignition delay with $\chi_o(\mathrm{s}^{-1})$.

Table 6.8: Values of $\eta_{ign,lim}$, $\chi_{o,lim}\,(\mathrm{s}^{-1})$, $\langle\chi|\eta\rangle_{lim}\,(\mathrm{s}^{-1})$, and $\{\langle\chi|\eta_{ign}\rangle\}_{R^+}\,(\mathrm{s}^{-1})$ from Series I and II.

				$\{\langle\chi\|\eta_{ign}\rangle\}_{R^+}\,(\mathrm{s}^{-1})$	
T_{air} (K)	$\chi_{o,lim}\,(\mathrm{s}^{-1})$	η_{ign}	$\langle\chi\|\eta\rangle_{lim}\,(\mathrm{s}^{-1})$	Series I	Series II
1200	178.26	0.03300	6.070	0.258	1.894
1250	280.75	0.03575	10.866	1.112	2.733
1300	443.74	0.03850	19.455	1.555	2.830
1350	687.93	0.03300	23.427	2.152	3.449
1400	1116.48	0.03025	32.928	2.594	6.032

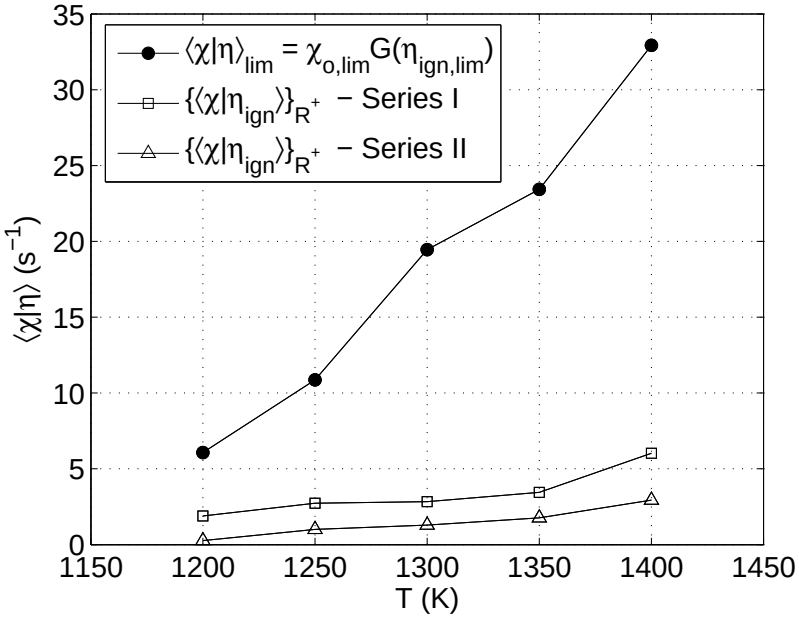

Figure 6.15: Comparison of the ignition scalar dissipation rates from Series I and II with the limiting value.

6.5 Perfectly Homogeneous Reactor

The Perfectly Homogeneous Reactor (PHR) equations are obtained by removing the micro-mixing and the spatial transport terms from the CMC equation (Eq.(6.2)), i.e. only the chemical source term is kept. The resulting equation is conditioned at a specific mixture fraction value. Here it is chosen to be η_{ign} obtained in series II when the AMC model is used. Thus, the PHR equation to be solved takes the form

$$\underbrace{\frac{\partial Q_\alpha}{\partial t}}_{\text{transient term}} = \underbrace{\frac{\langle \dot{\omega}_\alpha | \eta_{ign} \rangle}{\langle \rho | \eta_{ign} \rangle}}_{\text{chemical source}} . \tag{6.7}$$

Simulations over the temperature range 1200 K-1400 K are performed using the UBC-Mech 1.0 [49] chemical kinetics mechanism. Figure 6.16 displays the PHR results along with the homogeneous CMC results from Series I (Section 6.2), the inhomogeneous CMC results

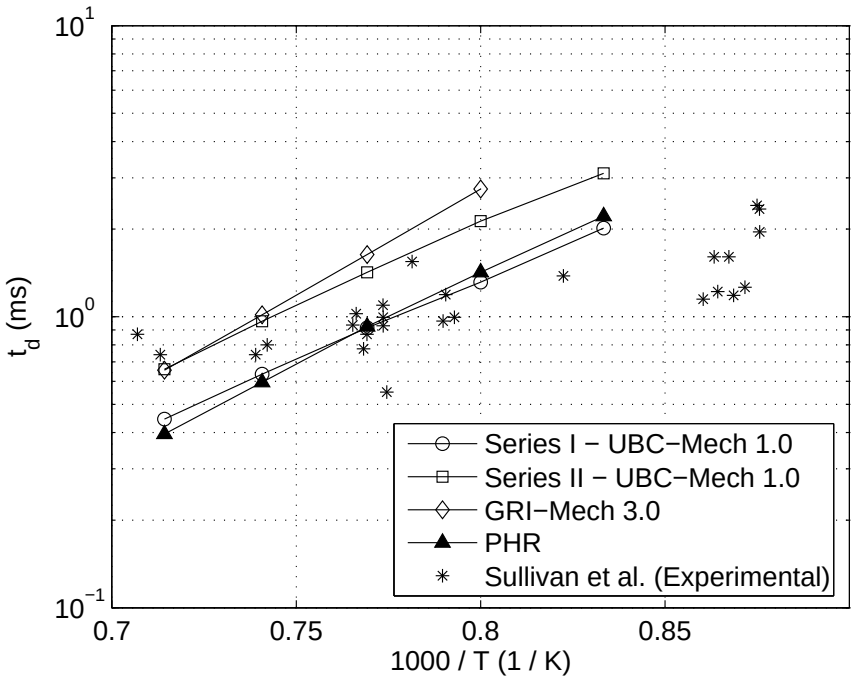

Figure 6.16: Ignition delay of a perfectly homogeneous reactor.

from Series II (Section 6.3), in addition to the GRI-Mech 3.0 [107] delays (Section 6.3.2) and the experimental data of sullivan et al. [113].
As shown, the PHR ignition delay values are in very good agreement with the experimental data. Furthermore, the results are lower than those predicted by the inhomogeneous CMC calculations, but very close to the homogeneous calculations. This is an expected behavior since both sets do not account for spatial transport.

6.6 Comparison with other Experiments and Numerical Simulations

In order to compare this study with previously published work, the current results are compared with the experimental data of Fraser et al. [102] and the numerical simulations

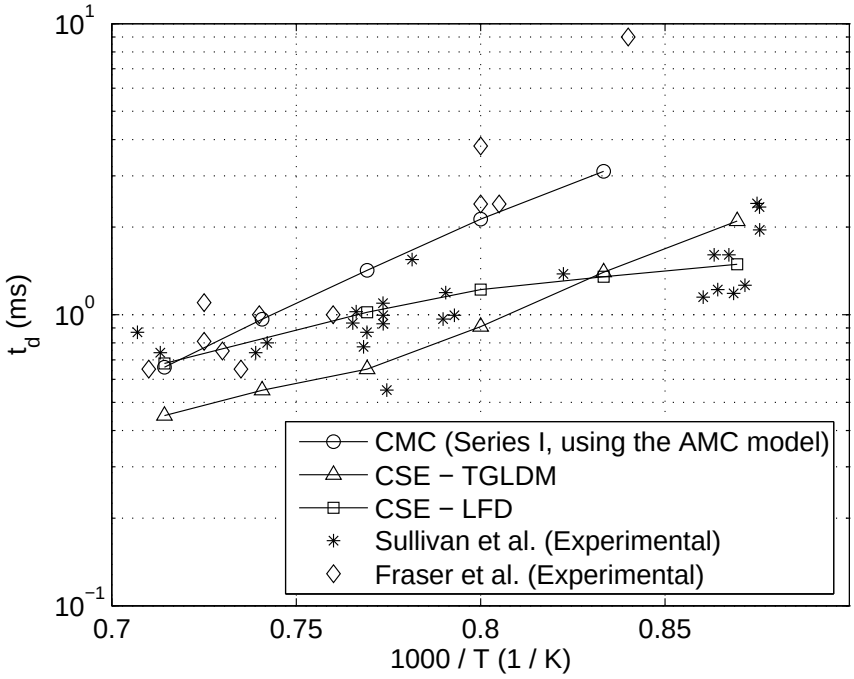

Figure 6.17: Comparison of the current result with other experiments and numerical simulations.

of Huang et al. [48] and Grout et al. [42] in Figure 6.17. Fraser et al. injected pure methane at a temperature of 444 K and a mass flow rate of 4.286×10^{-3} Kg/s into a constant-volume vessel filled with hot air. The initial air temperature was varied between 900 K and 1700 K, and the initial pressures of 25 and 40 atm were investigated. Although the experimental conditions are different from those of the shock tube (see Section 4.1), it is interesting to see how the results compare to the situation in hand. The ignition delay values shown in Figure 6.17 are obtained by interpolating the results of Fraser et al. to the pressure of 29.61 atm (30 bar). The resulting delays are in good agreement with the results of Sullivan et al. [113] for high air temperatures, but larger in magnitude at lower temperatures. Overall, the CMC results agree well with Fraser's experiments. Two sets of numerical simulations are considered. Both simulations use the Conditional Source Estimation (CSE) method, a CMC-based method suggested by Bushe et al. [15]. Grout et al. [42] used CSE with

the Laminar Flamelet Decomposition (LFD) approach as proposed by Bushe et al. [16], while Huang et al. [48] employed CSE in conjunction with the Trajectory Generated Low-dimensional Manifold (TGLDM) technique suggested by Pope et al. [94]. In short, LFD provides a basis function for the CSE computations, and TGLDM aims at reducing the chemical kinetics, thus reducing the computational cost of the simulations. Grout et al. and Huang et al. considered the same shock tube experiments and used the same chemical kinetics mechanism (UBC-Mech 1.0 [49]) in their calculations. Grout et al. used the 75 K temperature rise criterion which is utilized in this study. On the other hand, Huang et al. employed the maximum slope criterion and applied it to various scalars such as the temperature and the concentrations of OH and C_2H_2. Only the results corresponding to the temperature-based criterion are plotted in Figure 6.17. Comparison of the three numerical simulations shows that CSE-LFD agrees the most with the experimental data of Sullivan et al. [113]. Furthermore, CMC and CSE-LFD are in good agreement for air temperatures greater than 1300 K. As for CSE-TGLDM, it underpredicts the experiments at high air temperatures (greater than 1350 K). However, it achieves a better agreement at lower temperatures.

6.7 Conclusions

The ignition delay of non-premixed methane-air mixtures was investigated at high pressure for a wide range of air temperatures. Different forms of the CMC equations were considered, and several chemical kinetics mechanisms and ignition criteria were tested. The ignition criterion based on a 75 K increase in the conditional temperature was mainly used throughout this study. The homogeneous CMC calculations are in very good agreement with the experimental data, while the inhomogeneous calculations show good agreement at high air temperature, with an overprediction at lower temperatures. However, the experiments show a considerable scatter. The trends of decreasing ignition delay and ignition location in physical space with increasing air temperature are well reproduced. An opposite trend is observed in the scalar dissipation rate. Both scalar dissipation rate models result in comparable ignition delays, with the AMC model predicting ignition slightly earlier than Girimaji's model. In both cases, ignition always occurs at low scalar dissipation rate

values and in fuel-lean mixtures in mixture fraction space. It was also shown that spatial transport delays autoignition and affects the ignition location in physical. Furthermore, it was demonstrated that all the terms of the CMC equations are relevant to autoignition problems, with variable contributions. As for the chemistry, UBC-Mech 1.0 and GRI-Mech 3.0 predict very close ignition delays for high air temperatures. However, the GRI-Mech 3.0 delays are longer for lower temperatures and substantially overpredict the experimental data. Regarding ignition criteria, the 2000 K and maximum slope ignition criteria yield comparable results, while the 75 K conditional temperature rise results in shorter delays. Furthermore, the ignition delays obtained using the 75 K temperature rise criterion in physical and in conditional spaces are very close. The investigation of the ignition limit showed that the limiting scalar dissipation rate increases with increasing temperature, and that the ignition scalar dissipation rates from the homogeneous and inhomogeneous calculations are much smaller than the limiting values for all initial air temperatures. The perfectly homogeneous reactor calculations were shown to be in very good agreement with the experimental data and very close to the homogeneous CMC calculations. Finally, the results compared well to other experimental data and numerical simulations from the literature.

Chapter 7

Conclusions

The applicability of the first-order Conditional Moment Closure method to non-premixed autoignition problems was investigated using detailed chemistry. Specifically, conditions relevant to direct-injection engine applications were considered. Autoignition resulting from the direct injection of a low-temperature (300 K) turbulent methane jet into high-pressure (30 bar) stagnant air was studied for various initial air temperatures ranging from 1200 K to 1400 K. The first part of this thesis dealt with the derivations of the first-order CMC equations and the primary closure hypothesis. Submodels for the unclosed terms such as the conditional turbulent fluxes, scalar dissipation rate, velocity, and chemical source, in addition to the probability density function were validated against DNS and experimental data. The second part focused on the turbulent velocity and mixing flow fields calculations. For simplicity, the turbulent flow field and CMC calculations were decoupled based on the frozen mixing assumption [76]. The k-ε turbulence model was employed, and two-dimensional transient libraries containing the flow field variables of interest were built. These libraries were used as inputs to the CMC calculations. The third part described the numerical methods and the computational tools used in the calculations. The cross-stream averaging and the enthalpy-mixture fraction linear coupling techniques were discussed. The discretization of the CMC equations and the implementation of the fractional step method were demonstrated. A description of the packages LSODE [45], QUADPACK [92], and CHEMKIN II [52] was given. The chemical kinetics mechanisms UBC-Mech 1.0 [49] and GRI-Mech 3.0 [107] were also introduced. Finally, the last part presented the simulation

results. An assessment is given in the next section. Suggestions for future work are also proposed.

7.1 Assessment of the Current Results

The homogeneous and inhomogeneous CMC equations were solved for various initial air temperatures, and using two scalar dissipation rate models. The homogeneous ignition delays are in very good agreement with the experimental data, while the inhomogeneous delays show good agreement at high air temperature, with an overprediction at lower temperatures. In both cases, the trend of decreasing ignition delay with increasing air temperature observed in the experiments is well reproduced, and ignition always occurs in fuel-lean mixtures in mixture fraction space. In the homogeneous case, two chemical kinetics mechanism and several ignition criteria were tested. Furthermore, the ignition limit was investigated and perfectly homogeneous reactor calculations were performed.

Effect of Spatial Transport

The homogeneous and inhomogeneous CMC calculations performed in this study suggest that spatial transport affects autoignition in two ways:

1. it yields longer ignition delays, and

2. it results in further ignition kernel locations along the jet centerline.

Consequently, spatial transport is important in autoignition problems, and therefore should not be neglected. In both series of calculations, the trend of decreasing ignition kernel location with increasing initial air temperature is in very good agreement with the experiments.

Effect of the Conditional Scalar dissipation Rate Models

Girimaji's model and the AMC model were used to compute the conditional scalar dissipation rate in both the homogeneous and the inhomogeneous CMC calculations. Both models result in comparable ignition delays and ignition kernel locations, with the AMC model predicting ignition slightly earlier. Furthermore, the conditional scalar dissipation

at the ignition point increases with decreasing air temperature, and ignition always occurs at low scalar dissipation values.

Accuracy of the Chemical Kinetics

The chemical kinetics mechanisms UBC-Mech 1.0 and GRI-Mech 3.0 predict similar ignition delays for high air temperatures, but the GRI-Mech 3.0 delays are longer for lower temperatures. Overall, GRI-Mech 3.0 is in better agreement with the experimental data, thus demonstrating the feasibility of the chemical kinetics optimization.

Sensitivity to Autoignition Criteria

The autoignition criterion plays a key role in determining the ignition delay values. As general observations, higher temperature requirements result in longer ignition delays, and yield higher ignition mixture fraction values. The effect on the ignition kernel location is negligible and ignition occurs at low scalar dissipation rate values.

Ignition Limit

The ignition limit was investigated in terms of the critical scalar dissipation rate value beyond which ignition cannot occur. Two observations can be made:

1. the limiting scalar dissipation rate increases with increasing air temperature, and
2. the ignition scalar dissipation rates from the homogeneous and inhomogeneous calculations are much smaller than the limiting values for all initial air temperatures.

7.2 Future Work

Several assumptions were made in this work. Some are associated with the combustion model and others are specific to this study. First, the conditional fluctuations of the density, the temperature, and the species concentrations are neglected in the first-order closure of the conditional chemical source term [63]. If the magnitude of these fluctuations is small enough, this closure is adequate. However, in situations where the fluctuations

are significant such as in autoignition, reignition and extinction problems, it may not be suitable. Other simplifications were made in this study in order to reduce the complexity of the problem in hand. The first simplification is related to the interface between the turbulent flow field and the turbulent combustion calculations. The decoupling technique is suitable for autoignition problems since the density and temperature variations in the pre-ignition phase are usually small. One drawback of this technique is that the heat released by the exothermic chemical reactions is neglected in the turbulent flow field calculations. Consequently, decoupling is not applicable in the presence of a flame, which is an important phenomenon in the post-ignition phase. The second assumption is related to the cross-stream averaging technique. Although it was proven to be valid both mathematically [62] and experimentally [9, 111, 115], the application of this technique requires the flow to be self-similar. In this study, the jet is not-self similar at the early stages of injection, which might have introduced some inaccuracies. By all means, it is always more accurate to perform the CMC calculations in two-dimensional physical space. The third assumption is associated with neglecting the radiation heat transfer source term. This can be justified by the negligible soot concentration and low temperature in the pre-ignition phase. Finally, Girimaji's model and the AMC model are derived assuming homogeneous turbulence, which is not the case here. Still, the AMC model was found to be capable of capturing the inhomogeneity of the flow better than Girimaji's model. This observation was also reported by Swaminathan et al. [116].

The deficiencies introduced by the decoupling and the cross-stream averaging techniques can be remedied by performing two-dimensional coupled calculations. Radiation can be included if a computationally inexpensive radiation model is incorporated. As for micro-mixing, Devaud et al. [22] proposed a scalar dissipation model for inhomogeneous turbulent flows. A more realistic representation of the mixing field can be obtained if this model is implemented. Furthermore, it is possible to include the conditional fluctuations in the closure of the conditional chemical source term. Mastorakos et al. [79] proposed the second-order CMC method, where a second-order closure accounting for temperature fluctuations is applied to the chemical source. Other improvements include the Doubly-Conditioned Moment Closure (DCMC) method, in which another conditioning variable besides the mixture fraction, is introduced. Kronenburg et al. [65] selected the sensible enthalpy to

be the second conditioning variable, while Cha et al [17] chose the scalar dissipation rate. If DCMC is used, it is recommended to reduce the chemical kinetics due to the increased computational cost. Various techniques are available such as ILDM [74] or TGLDM [94].

Appendix A

Derivation of the CMC Equations

A.1 Species Transport Equation

Considering the species transport equation

$$\rho \underbrace{\frac{\partial Y_\alpha}{\partial t}}_{\text{I}} + \rho u_i \underbrace{\frac{\partial Y_\alpha}{\partial x_i}}_{\text{II}} = \underbrace{\frac{\partial}{\partial x_i}\left(\rho D_\alpha \frac{\partial Y_\alpha}{\partial x_i}\right)}_{\text{III}} + \dot{\omega}_\alpha, \tag{A.1}$$

the objective is to introduce $Y_\alpha(x_i,t) = Q_\alpha(\xi(x_i,t),x_i,t) + y''_\alpha(x_i,t)$ in Eq.(A.1), and then take the conditional average of the resulting expression. Special attention is required while performing this substitution since $Q_\alpha = Q_\alpha(\xi,x_i,t)$, $y''_\alpha = y''_\alpha(x_i,t)$ and $\xi = \xi(x_i,t)$. To simplify the process, the terms involving Y_α are labeled as shown Eq.(A.1) and each is treated aside.

Term I:

$$\begin{aligned}\frac{\partial}{\partial t}Y_\alpha(x_i,t) &= \frac{\partial}{\partial t}Q_\alpha(\xi(x_i,t),x_i,t) + \frac{\partial}{\partial t}y''_\alpha(x_i,t) \\ &= \frac{\partial Q_\alpha}{\partial \xi}\frac{\partial \xi}{\partial t} + \frac{\partial Q_\alpha}{\partial t} + \frac{\partial y''_\alpha}{\partial t}.\end{aligned} \tag{A.2}$$

Term II:

$$\begin{aligned}\frac{\partial}{\partial x_i}Y_\alpha(x_i,t) &= \frac{\partial}{\partial x_i}\left[Q_\alpha(\xi,x_i,t) + y''_\alpha(x_i,t)\right] \\ &= \frac{\partial Q_\alpha}{\partial \xi}\frac{\partial \xi}{\partial x_i} + \frac{\partial Q_\alpha}{\partial x_i} + \frac{\partial y''_\alpha}{\partial x_i}.\end{aligned} \tag{A.3}$$

Term III:

$$\begin{aligned}\frac{\partial}{\partial x_i}\left(\rho D_\alpha \frac{\partial Y_\alpha}{\partial x_i}\right) &= \frac{\partial}{\partial x_i}\left[\rho D_\alpha\left(\frac{\partial Q_\alpha}{\partial \xi}\frac{\partial \xi}{\partial x_i}+\frac{\partial Q_\alpha}{\partial x_i}+\frac{\partial y''_\alpha}{\partial x_i}\right)\right]\\ &= \frac{\partial}{\partial x_i}\left(\rho D_\alpha \frac{\partial Q_\alpha}{\partial \xi}\frac{\partial \xi}{\partial x_i}\right)+\frac{\partial}{\partial x_i}\left(\rho D_\alpha \frac{\partial Q_\alpha}{\partial x_i}\right)+\frac{\partial}{\partial x_i}\left(\rho D_\alpha \frac{\partial y''_\alpha}{\partial x_i}\right)\\ &= \frac{\partial Q_\alpha}{\partial \xi}\frac{\partial}{\partial x_i}\left(\rho D_\alpha \frac{\partial \xi}{\partial x_i}\right)+\rho D_\alpha\left(\frac{\partial \xi}{\partial x_i}\frac{\partial \xi}{\partial x_i}\right)\frac{\partial^2 Q_\alpha}{\partial \xi^2}\\ &\quad+\rho D_\alpha \frac{\partial \xi}{\partial x_i}\frac{\partial}{\partial \xi}\left(\frac{\partial Q_\alpha}{\partial x_i}\right)+\frac{\partial}{\partial x_i}\left(\rho D_\alpha \frac{\partial Q_\alpha}{\partial x_i}\right)+\frac{\partial}{\partial x_i}\left(\rho D_\alpha \frac{\partial y''_\alpha}{\partial x_i}\right).\end{aligned} \tag{A.4}$$

Substituting Eqs.(A.2), (A.3) and (A.4) in Eq.(A.1) yields:

$$\begin{aligned}&\rho\left(\frac{\partial Q_\alpha}{\partial \xi}\frac{\partial \xi}{\partial t}+\frac{\partial Q_\alpha}{\partial t}+\frac{\partial y''_\alpha}{\partial t}\right)+\rho u_i\left(\frac{\partial Q_\alpha}{\partial \xi}\frac{\partial \xi}{\partial x_i}+\frac{\partial Q_\alpha}{\partial x_i}+\frac{\partial y''_\alpha}{\partial x_i}\right)=\\ &\frac{\partial Q_\alpha}{\partial \xi}\frac{\partial}{\partial x_i}\left(\rho D_\alpha \frac{\partial \xi}{\partial x_i}\right)+\rho D_\alpha\left(\frac{\partial \xi}{\partial x_i}\frac{\partial \xi}{\partial x_i}\right)\frac{\partial^2 Q_\alpha}{\partial \xi^2}+\rho D_\alpha \frac{\partial \xi}{\partial x_i}\frac{\partial}{\partial \xi}\left(\frac{\partial Q_\alpha}{\partial x_i}\right)\\ &+\frac{\partial}{\partial x_i}\left(\rho D_\alpha \frac{\partial Q_\alpha}{\partial x_i}\right)+\frac{\partial}{\partial x_i}\left(\rho D_\alpha \frac{\partial y''_\alpha}{\partial x_i}\right)+\dot{\omega}_\alpha.\end{aligned} \tag{A.5}$$

Grouping the terms having $\partial Q_\alpha/\partial \xi$ in Eq.(A.5) results in:

$$\begin{aligned}&\rho\frac{\partial Q_\alpha}{\partial t}+\rho\frac{\partial y''_\alpha}{\partial t}+\frac{\partial Q_\alpha}{\partial \xi}\left[\rho\frac{\partial \xi}{\partial t}+\rho u_i\frac{\partial \xi}{\partial x_i}-\frac{\partial}{\partial x_i}\left(\rho D_\alpha\frac{\partial \xi}{\partial x_i}\right)\right]+\rho u_i\frac{\partial Q_\alpha}{\partial x_i}\\ &+\rho u_i\frac{\partial y''_\alpha}{\partial x_i}=\rho D_\alpha\left(\frac{\partial \xi}{\partial x_i}\frac{\partial \xi}{\partial x_i}\right)\frac{\partial^2 Q_\alpha}{\partial \xi^2}+\rho D_\alpha\frac{\partial \xi}{\partial x_i}\frac{\partial}{\partial \xi}\left(\frac{\partial Q_\alpha}{\partial x_i}\right)+\frac{\partial}{\partial x_i}\left(\rho D_\alpha\frac{\partial Q_\alpha}{\partial x_i}\right)\\ &+\frac{\partial}{\partial x_i}\left(\rho D_\alpha\frac{\partial y''_\alpha}{\partial x_i}\right)+\dot{\omega}_\alpha.\end{aligned} \tag{A.6}$$

The first two terms inside the brackets in Eq.(A.6) represent the LHS of the mixture fraction equation (Eq.(2.44)):

$$\rho\frac{\partial \xi}{\partial t}+\rho u_i\frac{\partial \xi}{\partial x_i}=\frac{\partial}{\partial x_i}\left(\rho D\frac{\partial \xi}{\partial x_i}\right). \tag{A.7}$$

Subtracting $\dfrac{\partial}{\partial x_i}\left(\rho D_\alpha\dfrac{\partial \xi}{\partial x_i}\right)$ from both sides of Eq.(A.7) gives:

$$\rho\frac{\partial \xi}{\partial t}+\rho u_i\frac{\partial \xi}{\partial x_i}-\frac{\partial}{\partial x_i}\left(\rho D_\alpha\frac{\partial \xi}{\partial x_i}\right)=\frac{\partial}{\partial x_i}\left[\rho\left(D-D_\alpha\right)\frac{\partial \xi}{\partial x_i}\right]. \tag{A.8}$$

Finally, the substitution of Eq.(A.8) in Eq.(A.6) yields:

$$\begin{aligned}\rho\frac{\partial Q_\alpha}{\partial t}+\rho\frac{\partial y''_\alpha}{\partial t}+\frac{\partial Q_\alpha}{\partial \xi}\frac{\partial}{\partial x_i}\left[\rho(D-D_\alpha)\frac{\partial \xi}{\partial x_i}\right]+\rho u_i\frac{\partial Q_\alpha}{\partial x_i}+\rho u_i\frac{\partial y''_\alpha}{\partial x_i}=\\ \rho D_\alpha\left(\frac{\partial \xi}{\partial x_i}\frac{\partial \xi}{\partial x_i}\right)\frac{\partial^2 Q_\alpha}{\partial \xi^2}+\rho D_\alpha\frac{\partial \xi}{\partial x_i}\frac{\partial}{\partial \xi}\left(\frac{\partial Q_\alpha}{\partial x_i}\right)+\frac{\partial}{\partial x_i}\left(\rho D_\alpha\frac{\partial Q_\alpha}{\partial x_i}\right)\\ +\frac{\partial}{\partial x_i}\left(\rho D_\alpha\frac{\partial y''_\alpha}{\partial x_i}\right)+\dot{\omega}_\alpha.\end{aligned} \tag{A.9}$$

The next step is to conditionally average Eq.(A.9) at $\xi(x_i,t)=\eta$. This results in:

$$\begin{aligned}\left\langle\rho\frac{\partial Q_\alpha}{\partial t}\middle|\,\eta\right\rangle+\left\langle\rho\frac{\partial y''_\alpha}{\partial t}\middle|\,\eta\right\rangle+\left\langle\frac{\partial Q_\alpha}{\partial \xi}\frac{\partial}{\partial x_i}\left[\rho\left(D-D_\alpha\right)\frac{\partial \xi}{\partial x_i}\right]\middle|\,\eta\right\rangle+\left\langle\rho u_i\frac{\partial Q_\alpha}{\partial x_i}\middle|\,\eta\right\rangle\\ +\left\langle\rho u_i\frac{\partial y''_\alpha}{\partial x_i}\middle|\,\eta\right\rangle=\left\langle\rho D_\alpha\left(\frac{\partial \xi}{\partial x_i}\frac{\partial \xi}{\partial x_i}\right)\frac{\partial^2 Q_\alpha}{\partial \xi^2}\middle|\,\eta\right\rangle+\left\langle\rho D_\alpha\frac{\partial \xi}{\partial x_i}\frac{\partial}{\partial \xi}\left(\frac{\partial Q_\alpha}{\partial x_i}\right)\middle|\,\eta\right\rangle\\ +\left\langle\frac{\partial}{\partial x_i}\left(\rho D_\alpha\frac{\partial Q_\alpha}{\partial x_i}\right)\middle|\,\eta\right\rangle+\left\langle\frac{\partial}{\partial x_i}\left(\rho D_\alpha\frac{\partial y''_\alpha}{\partial x_i}\right)\middle|\,\eta\right\rangle+\left\langle\dot{\omega}_\alpha\middle|\,\eta\right\rangle,\end{aligned} \tag{A.10}$$

where the notation $\langle\,|\eta\rangle$ is used instead of $\langle\,|\xi(x_i,t)=\eta\rangle$ for simplicity. Next, Eq.(A.10) is rearranged as

$$\begin{aligned}\langle\rho|\,\eta\rangle\frac{\partial Q_\alpha}{\partial t}+\langle\rho|\,\eta\rangle\langle u_i|\,\eta\rangle\frac{\partial Q_\alpha}{\partial x_i}=\langle\rho|\,\eta\rangle\left\langle D_\alpha\left(\frac{\partial \xi}{\partial x_i}\frac{\partial \xi}{\partial x_i}\right)\middle|\,\eta\right\rangle\frac{\partial^2 Q_\alpha}{\partial \eta^2}\\ +\left\langle\left[\frac{\partial}{\partial x_i}\left(\rho D_\alpha\frac{\partial Q_\alpha}{\partial x_i}\right)+\rho D_\alpha\frac{\partial \xi}{\partial x_i}\frac{\partial}{\partial \xi}\left(\frac{\partial Q_\alpha}{\partial x_i}\right)+\frac{\partial Q_\alpha}{\partial \xi}\frac{\partial}{\partial x_i}\left(\rho\left(D_\alpha-D\right)\frac{\partial \xi}{\partial x_i}\right)\right]\middle|\,\eta\right\rangle\\ -\left\langle\left[\rho\frac{\partial y''_\alpha}{\partial t}+\rho u_i\frac{\partial y''_\alpha}{\partial x_i}-\frac{\partial}{\partial x_i}\left(\rho D_\alpha\frac{\partial y''_\alpha}{\partial x_i}\right)\right]\middle|\,\eta\right\rangle+\langle\dot{\omega}_\alpha|\,\eta\rangle\,.\end{aligned} \tag{A.11}$$

Finally, Eq.(A.11) is written as

$$\langle\rho|\eta\rangle\frac{\partial Q_\alpha}{\partial t}+\langle\rho|\eta\rangle\langle u_i|\eta\rangle\frac{\partial Q_\alpha}{\partial x_i}=\langle\rho|\eta\rangle\left\langle D_\alpha\left(\frac{\partial \xi}{\partial x_i}\frac{\partial \xi}{\partial x_i}\right)\middle|\eta\right\rangle\frac{\partial^2 Q_\alpha}{\partial \eta^2}+e_Q+e_y+\langle\dot{\omega}_\alpha|\eta\rangle, \tag{A.12}$$

where

$$e_Q=\left\langle\left[\frac{\partial}{\partial x_i}\left(\rho D_\alpha\frac{\partial Q_\alpha}{\partial x_i}\right)+\rho D_\alpha\frac{\partial \xi}{\partial x_i}\frac{\partial}{\partial \xi}\left(\frac{\partial Q_\alpha}{\partial x_i}\right)+\frac{\partial Q_\alpha}{\partial \xi}\frac{\partial}{\partial x_i}\left(\rho(D_\alpha-D)\frac{\partial \xi}{\partial x_i}\right)\right]\middle|\eta\right\rangle, \tag{A.13}$$

and

$$e_y=-\left\langle\left[\rho\frac{\partial y''_\alpha}{\partial t}+\rho u_i\frac{\partial y''_\alpha}{\partial x_i}-\frac{\partial}{\partial x_i}\left(\rho D_\alpha\frac{\partial y''_\alpha}{\partial x_i}\right)\right]\middle|\eta\right\rangle. \tag{A.14}$$

A.2 Primary Closure Hypothesis

A.2.1 Closure for e_Q

Writing the density-diffusivity products in Eq.(A.13) in terms of the Schmidt number, one obtains

$$\rho D = \frac{\mu}{\mathrm{Sc}} \quad \text{and} \quad \rho D_\alpha = \frac{\mu}{\mathrm{Sc}_\alpha}. \tag{A.15}$$

Given finite Schmidt numbers, these products scale as Re^{-1}, i.e.,

$$\rho D \sim \frac{1}{\mathrm{Re}} \quad \text{and} \quad \rho D_\alpha \sim \frac{1}{\mathrm{Re}}. \tag{A.16}$$

Hence, for high Re applications,

$$\rho D \to 0 \quad \text{and} \quad \rho D_\alpha \to 0. \tag{A.17}$$

Consequently, if finite Schmidt numbers and high Reynolds number govern the flow field, all the terms in Eq.(A.13) are neglected [8, 63, 71].

A.2.2 Closure for e_y

The first two terms in Eq.(A.14) are neglected based on the analysis of Klimenko and Bilger [63]. It was previously established that the conditional average of the conditional fluctuations is null, that is

$$\langle y''_\alpha | \eta \rangle = 0. \tag{A.18}$$

However, Eq.(A.18) does not imply that $\langle \partial y''_\alpha / \partial t | \eta \rangle = 0$ and $\langle \partial y''_\alpha / \partial x_i | \eta \rangle = 0$ because $\langle \partial y''_\alpha / \partial t | \eta \rangle \neq \partial \langle y''_\alpha | \eta \rangle / \partial t$ and $\langle \partial y''_\alpha / \partial x_i | \eta \rangle \neq \partial \langle y''_\alpha | \eta \rangle / \partial x_i$. On the other hand, the unconditional mean of y'', $\langle y'' \rangle$, is related to $\langle y'' | \eta \rangle$ by the integral

$$\langle y''_\alpha \rangle = \int_0^1 \langle y''_\alpha |\, \eta \rangle P(\eta) d\eta. \tag{A.19}$$

Hence,

$$\langle y''_\alpha \rangle = 0. \tag{A.20}$$

Considering the unconditional mean of e_y,

$$\begin{aligned}\int_0^1 e_y P(\eta)d\eta &= -\int_0^1 \left\langle \left[\rho\frac{\partial y''_\alpha}{\partial t} + \rho u_i \frac{\partial y''_\alpha}{\partial x_i} - \frac{\partial}{\partial x_i}\left(\rho D_\alpha \frac{\partial y''_\alpha}{\partial x_i}\right)\right] \middle| \eta \right\rangle P(\eta)d\eta \\ &= -\left\langle \rho\frac{\partial y''_\alpha}{\partial t} + \rho u_i \frac{\partial y''_\alpha}{\partial x_i} - \frac{\partial}{\partial x_i}\left(\rho D \frac{\partial y''_\alpha}{\partial x_i}\right)\right\rangle \\ &= -\left\langle \frac{\partial}{\partial t}\left(\rho y''_\alpha\right)\right\rangle - \left\langle \frac{\partial}{\partial x_i}\left(\rho u_i y''_\alpha\right)\right\rangle + \left\langle \frac{\partial}{\partial x_i}\left(\rho D \frac{\partial y''_\alpha}{\partial x_i}\right)\right\rangle \\ &= -\frac{\partial}{\partial t}\left\langle \rho y''_\alpha\right\rangle - \frac{\partial}{\partial x_i}\left\langle \rho u_i y''_\alpha\right\rangle + \frac{\partial}{\partial x_i}\left\langle \rho D \frac{\partial y''_\alpha}{\partial x_i}\right\rangle,\end{aligned} \tag{A.21}$$

a simplifying assumption is done here by neglecting the conditional fluctuation of ρ and D. Starting with the first term on the RHS of Eq.(A.21), the decomposition of ρ yields:

$$\frac{\partial \left\langle \rho y''_\alpha\right\rangle}{\partial t} = \frac{\partial}{\partial t}\left\langle \left(\left\langle \rho|\eta\right\rangle + \rho''\right) y''_\alpha\right\rangle \approx \frac{\partial}{\partial t}\left\langle \left\langle \rho|\eta\right\rangle y''_\alpha\right\rangle = \frac{\partial}{\partial t}\left(\left\langle \rho|\eta\right\rangle \left\langle y''_\alpha\right\rangle\right) = 0, \tag{A.22}$$

where $\langle y''_\alpha\rangle = 0$ (Eq.(A.20)) is used. A similar procedure is followed regarding the third term on the RHS of Eq.(A.21). Decomposition of ρ and D results in:

$$\begin{aligned}\frac{\partial}{\partial x_i}\left\langle \rho D \frac{\partial y''_\alpha}{\partial x_i}\right\rangle &= \frac{\partial}{\partial x_i}\left\langle \left(\left\langle \rho|\eta\right\rangle + \rho''\right)\left(\left\langle D|\eta\right\rangle + D''\right)\frac{\partial y''_\alpha}{\partial x_i}\right\rangle \\ &\approx \frac{\partial}{\partial x_i}\left\langle \left\langle \rho|\eta\right\rangle \left\langle D|\eta\right\rangle \frac{\partial y''_\alpha}{\partial x_i}\right\rangle = \frac{\partial}{\partial x_i}\left(\left\langle \rho|\eta\right\rangle \left\langle D|\eta\right\rangle \frac{\partial \left\langle y''_\alpha\right\rangle}{\partial x_i}\right) = 0,\end{aligned} \tag{A.23}$$

Using the results of Eqs.(A.22) and (A.23), Eq.(A.21) reduces to

$$\int_0^1 e_y P(\eta)d\eta \approx -\frac{\partial}{\partial x_i}\left\langle \rho u_i y''_\alpha\right\rangle. \tag{A.24}$$

Eq.(A.24) may be simplified further by decomposing the velocity and the density as follows:

$$
\begin{aligned}
\frac{\partial}{\partial x_i}\left\langle \rho u_i y''_\alpha \right\rangle &= \frac{\partial}{\partial x_i}\left\langle \rho\left(\left\langle u_i\right|\eta\right\rangle + u''_i\right) y''_\alpha \right\rangle \\
&= \left\langle \frac{\partial}{\partial x_i}\left(\rho\left\langle u_i|\eta\right\rangle y''_\alpha\right)\right\rangle + \frac{\partial}{\partial x_i}\left\langle \rho u''_i y''_\alpha\right\rangle \\
&= \left\langle u_i\right|\eta\rangle \frac{\partial\left\langle \rho y''_\alpha\right\rangle}{\partial x_i} + \left\langle \rho y''_\alpha\right\rangle \frac{\partial\left\langle u_i\right|\eta\right\rangle}{\partial x_i} + \frac{\partial}{\partial x_i}\left\langle \rho u''_i y''_\alpha\right\rangle \\
&= \frac{\partial}{\partial x_i}\left\langle\left(\left\langle \rho\right|\eta\right\rangle + \rho''\right) u''_i y''_\alpha\right\rangle \\
&\approx -\frac{\partial}{\partial x_i}\left\langle\left\langle \rho\right|\eta\right\rangle u''_i y''_\alpha\right\rangle \\
&= -\frac{\partial}{\partial x_i}\left(\left\langle \rho\right|\eta\right\rangle \left\langle u''_i y''_\alpha\right\rangle\right) \\
&= \frac{\partial}{\partial x_i}\left[\left\langle \rho\right|\eta\right\rangle \int_0^1 \left\langle u''_i y''_\alpha\right|\eta\right\rangle P(\eta) d\eta\Bigg] \\
&= \int_0^1 \frac{\partial}{\partial x_i}\left(\left\langle u''_i y''_\alpha\right|\eta\right\rangle \left\langle \rho\right|\eta\right\rangle P(\eta)\right) d\eta.
\end{aligned}
$$

where the approximation $\langle \rho y''_\alpha\rangle = \langle(\langle\rho|\eta\rangle + \rho'')y''_\alpha\rangle \approx \langle\rho|\eta\rangle\langle y''_\alpha\rangle = 0$ is used. Accordingly, Eq.(A.24) reduces to

$$
\int_0^1 e_y P(\eta) d\eta = -\int_0^1 \frac{\partial}{\partial x_i}\left(\left\langle u''_i y''_\alpha\right|\eta\right\rangle \left\langle \rho\right|\eta\right\rangle P(\eta)\right) d\eta. \tag{A.25}
$$

Differentiating Eq.(A.25) with respect to η and rearranging the resulting expression yields

$$
e_y = -\frac{1}{P(\eta)}\frac{\partial}{\partial x_i}\big(\big\langle u''_j y''_\alpha\big|\eta\big\rangle\langle\rho|\eta\rangle P(\eta)\big). \tag{A.26}
$$

Assuming $D_\alpha = D$ as in [8] and substituting Eq.(A.26) in Eq.(A.12) results in:

$$
\frac{\partial Q_\alpha}{\partial t} + \langle u_i|\eta\rangle\frac{\partial Q_\alpha}{\partial x_i} = -\frac{1}{\langle\rho|\eta\rangle P(\eta)}\frac{\partial}{\partial x_i}\big(\langle\rho|\eta\rangle\big\langle u''_i y''_\alpha\big|\eta\big\rangle P(\eta)\big) + \frac{1}{2}\langle\chi|\eta\rangle\frac{\partial^2 Q_\alpha}{\partial\eta^2} + \frac{\langle\dot\omega_\alpha|\eta\rangle}{\langle\rho|\eta\rangle}, \tag{A.27}
$$

where

$$
\chi = 2D\left(\frac{\partial\xi}{\partial x_i}\frac{\partial\xi}{\partial x_i}\right) \tag{A.28}
$$

is the scalar dissipation rate. Finally, introducing the Favre-averaged PDF, $\tilde{P}(\eta)$, which is related to $P(\eta)$ by

$$\langle\rho\rangle\,\tilde{P}(\eta) = \langle\,\rho|\,\eta\rangle\,P(\eta), \tag{A.29}$$

Eq.(A.27) takes the form

$$\frac{\partial Q_\alpha}{\partial t} + \langle u_i|\eta\rangle\,\frac{\partial Q_\alpha}{\partial x_i} = -\frac{1}{\langle\rho\rangle\tilde{P}(\eta)}\frac{\partial}{\partial x_i}\left(\langle\rho\rangle\,\langle u_i'' y_\alpha''|\eta\rangle\,\tilde{P}(\eta)\right) + \frac{1}{2}\,\langle\chi|\eta\rangle\,\frac{\partial^2 Q_\alpha}{\partial\eta^2} + \frac{\langle\dot{\omega}_\alpha|\eta\rangle}{\langle\rho|\eta\rangle}. \tag{A.30}$$

A.3 Enthalpy and Temperature Equations

The specific enthalpy equation is written given by:

$$\begin{aligned}\rho\frac{\partial h}{\partial t} + \rho u_i\frac{\partial h}{\partial x_i} = \frac{\partial}{\partial x_i}\left(\frac{\lambda}{c_p}\frac{\partial h}{\partial x_i}\right) - \sum_{\alpha=1}^{n}\frac{\partial}{\partial x_i}\left[h_\alpha\left(\frac{\lambda}{c_p} - \rho D_\alpha\right)\frac{\partial Y_\alpha}{\partial x_i}\right] \\ + \frac{\partial p}{\partial t} + u_i\frac{\partial p}{\partial x_i} + \tau_{ij}\frac{\partial u_i}{\partial x_j} + \dot{q}_{rad}.\end{aligned} \tag{A.31}$$

If all Lewis numbers are assumed to be equal to unity, and if the convective pressure term and the dissipation by viscous stress are neglected, Eq.(A.31) reduces to

$$\rho\frac{\partial h}{\partial t} + \rho u_i\frac{\partial h}{\partial x_i} = \frac{\partial}{\partial x_i}\left(\rho D\frac{\partial h}{\partial x_i}\right) + \frac{\partial p}{\partial t} + \dot{q}_{rad}. \tag{A.32}$$

The derivation of the conditional enthalpy equation from Eq.(A.32) requires the same steps and assumptions made to obtain the conditional species continuity equation, Eq.(A.30). The final expression is given by:

$$\begin{aligned}\frac{\partial Q_h}{\partial t} + \langle\,u_i|\,\eta\rangle\,\frac{\partial Q_h}{\partial x_i} = &-\frac{1}{\langle\rho\rangle\,\tilde{P}(\eta)}\frac{\partial}{\partial x_i}\left(\langle\rho\rangle\,\langle\,u_i''h''|\,\eta\rangle\,\tilde{P}(\eta)\right) + \frac{1}{2}\,\langle\,\chi|\,\eta\rangle\,\frac{\partial^2 Q_h}{\partial\eta^2} \\ &+ \frac{1}{\langle\rho|\eta\rangle}\left\langle\frac{\partial p}{\partial t}\middle|\,\eta\right\rangle + \frac{\langle\,\dot{q}_{rad}|\,\eta\rangle}{\langle\rho|\eta\rangle}.\end{aligned} \tag{A.33}$$

The conditional temperature equation is obtained from Eq.(A.33). As a first step, the enthalpy is written as the sum of the species enthalpies:

$$h = \sum_{\alpha=1}^{N_s} h_\alpha Y_\alpha. \tag{A.34}$$

Taking the conditional average of Eq.(A.34),

$$Q_h = \sum_{\alpha=1}^{N_s} \langle h_\alpha|\eta\rangle Q_\alpha, \tag{A.35}$$

where N_s is the total number of species in the mixture. The differentiation of Eq.(A.35) with respect to time is performed as follows:

$$\begin{aligned}
\frac{\partial Q_h}{\partial t} &= \frac{\partial}{\partial t}\left(\sum_{\alpha=1}^{N_s} \langle h_\alpha|\eta\rangle Q_\alpha\right) \\
&= \sum_{\alpha=1}^{N_s} \frac{\partial\langle h_\alpha|\eta\rangle}{\partial t} Q_\alpha + \sum_{\alpha=1}^{N_s} \langle h_\alpha|\eta\rangle \frac{\partial Q_\alpha}{\partial t} \\
&= \left(\sum_{\alpha=1}^{N_s} \langle c_{p,\alpha} Y_\alpha|\eta\rangle\right) \frac{\partial Q_T}{\partial t} + \sum_{\alpha=1}^{N_s} \langle h_\alpha|\eta\rangle \frac{\partial Q_\alpha}{\partial t} \\
&= \left\langle \left(\sum_{\alpha=1}^{N_s} (c_{p,\alpha} Y_\alpha)\right) \middle| \eta \right\rangle \frac{\partial Q_T}{\partial t} + \sum_{\alpha=1}^{N_s} \langle h_\alpha|\eta\rangle \frac{\partial Q_\alpha}{\partial t},
\end{aligned} \tag{A.36}$$

where $\langle h_\alpha|\eta\rangle = \langle c_{p,\alpha}|\eta\rangle Q_T$ is used in the transition from the second step to the third step. The summation inside the first term on the LHS of Eq.(A.36) represents the conditional average of the specific heat of the mixture since

$$c_p = \sum_{\alpha=1}^{N_s} c_{p,\alpha} Y_\alpha. \tag{A.37}$$

Accordingly, Eq.(A.36) reduces to:

$$\frac{\partial Q_h}{\partial t} = \langle c_p|\eta\rangle \frac{\partial Q_T}{\partial t} + \sum_{\alpha=1}^{N_s} \langle h_\alpha|\eta\rangle \frac{\partial Q_\alpha}{\partial t}. \tag{A.38}$$

In a similar fashion, the derivatives with respect to x_i and η are

$$\frac{\partial Q_h}{\partial x_i} = \langle c_p|\,\eta\rangle \frac{\partial Q_T}{\partial x_i} + \sum_{\alpha=1}^{N_s} \langle h_\alpha|\,\eta\rangle \frac{\partial Q_\alpha}{\partial x_i}, \tag{A.39}$$

and

$$\frac{\partial Q_h}{\partial \eta} = \langle c_p|\,\eta\rangle \frac{\partial Q_T}{\partial \eta} + \sum_{\alpha=1}^{N_s} \langle h_\alpha|\,\eta\rangle \frac{\partial Q_\alpha}{\partial \eta}. \tag{A.40}$$

Substituting Eqs.(A.38), (A.39) and (A.40) in Eq.(A.33), and using $Q_h = \langle c_p|\eta\rangle Q_T$ yield:

$$\begin{aligned}\langle c_p|\eta\rangle\frac{\partial Q_T}{\partial t}+\sum_{\alpha=1}^{N_s}\langle h_\alpha|\eta\rangle\frac{\partial Q_\alpha}{\partial t}+\langle u_i|\eta\rangle\left(\langle c_p|\eta\rangle\frac{\partial Q_T}{\partial x_i}+\sum_{\alpha=1}^{N_s}\langle h_\alpha|\eta\rangle\frac{\partial Q_\alpha}{\partial x_i}\right)=\\ -\frac{\langle c_p|\eta\rangle}{\langle\rho\rangle\tilde{P}(\eta)}\frac{\partial}{\partial x_i}\left(\langle\rho\rangle\langle u_i''T''|\eta\rangle\tilde{P}(\eta)\right)+\frac{1}{2}\langle\chi|\eta\rangle\frac{\partial}{\partial\eta}\left(\langle c_p|\eta\rangle\frac{\partial Q_T}{\partial\eta}+\sum_{\alpha=1}^{N_s}\langle h_\alpha|\eta\rangle\frac{\partial Q_\alpha}{\partial\eta}\right)\\ +\frac{1}{\langle\rho|\eta\rangle}\left\langle\frac{\partial p}{\partial t}\middle|\,\eta\right\rangle+\frac{\langle\dot{q}_{rad}|\,\eta\rangle}{\langle\rho|\eta\rangle},\end{aligned}\tag{A.41}$$

where $h'' = c_pT''$ is used in the first term on the RHS of Eq.(A.41). This expression can be rearranged as:

$$\begin{aligned}\langle c_p|\eta\rangle\left(\frac{\partial Q_T}{\partial t}+\langle u_i|\eta\rangle\frac{\partial Q_T}{\partial x_i}\right)+\sum_{\alpha=1}^{N_s}\langle h_\alpha|\eta\rangle\left(\frac{\partial Q_\alpha}{\partial t}+\langle u_i|\eta\rangle\frac{\partial Q_\alpha}{\partial x_i}\right)=\\ -\frac{\langle c_p|\eta\rangle}{\langle\rho\rangle\tilde{P}(\eta)}\frac{\partial}{\partial x_i}\left(\langle\rho\rangle\langle u_i''T''|\eta\rangle\tilde{P}(\eta)\right)+\frac{1}{2}\langle\chi|\eta\rangle\frac{\partial}{\partial\eta}\left(\langle c_p|\eta\rangle\frac{\partial Q_T}{\partial\eta}+\sum_{\alpha=1}^{N_s}\langle h_\alpha|\eta\rangle\frac{\partial Q_\alpha}{\partial\eta}\right)\\ +\frac{1}{\langle\rho|\eta\rangle}\left\langle\frac{\partial p}{\partial t}\middle|\,\eta\right\rangle+\frac{\langle\dot{q}_{rad}|\,\eta\rangle}{\langle\rho|\eta\rangle}.\end{aligned}\tag{A.42}$$

Using Eq.(A.30) in the summation on the LHS of Eq.(A.42) and expanding the third term on the RHS,

$$\begin{aligned}\langle c_p|\eta\rangle\left(\frac{\partial Q_T}{\partial t}+\langle u_i|\eta\rangle\frac{\partial Q_T}{\partial x_i}\right)+\sum_{\alpha=1}^{N_s}\langle h_\alpha|\eta\rangle\left(\frac{1}{2}\langle\chi|\eta\rangle\frac{\partial^2 Q_\alpha}{\partial\eta^2}+\frac{\langle\dot{\omega}_\alpha|\eta\rangle}{\langle\rho|\eta\rangle}\right)=\\ -\frac{\langle c_p|\eta\rangle}{\langle\rho\rangle\tilde{P}(\eta)}\frac{\partial}{\partial x_i}\left(\langle\rho\rangle\langle u_i''T''|\eta\rangle\tilde{P}(\eta)\right)+\frac{1}{2}\langle\chi|\eta\rangle\left[\frac{\partial\langle c_p|\eta\rangle}{\partial\eta}\frac{\partial Q_T}{\partial\eta}+\langle c_p|\eta\rangle\frac{\partial^2 Q_T}{\partial\eta^2}+\right.\\ \left.\sum_{\alpha=1}^{N_s}\left(\langle c_{p,\alpha}|\eta\rangle\frac{\partial Q_\alpha}{\partial\eta}\right)\frac{\partial Q_T}{\partial\eta}+\sum_{\alpha=1}^{N_s}\left(\langle h_\alpha|\eta\rangle\frac{\partial^2 Q_\alpha}{\partial\eta^2}\right)\right]+\frac{1}{\langle\rho|\eta\rangle}\left\langle\frac{\partial p}{\partial t}\middle|\,\eta\right\rangle+\frac{\langle\dot{q}_{rad}|\,\eta\rangle}{\langle\rho|\eta\rangle}.\end{aligned}\tag{A.43}$$

Simplifying the last expression above yields the conditional temperature equation:

$$\frac{\partial Q_T}{\partial t} + \langle u_i|\eta\rangle \frac{\partial Q_T}{\partial x_i} = -\frac{1}{\langle\rho\rangle \tilde{P}(\eta)} \frac{\partial}{\partial x_i} \left(\langle\rho\rangle \langle u_i'' T''|\eta\rangle \tilde{P}(\eta) \right)$$
$$+\frac{1}{2}\langle\chi|\eta\rangle \left\{ \frac{\partial^2 Q_T}{\partial \eta^2} + \frac{1}{\langle c_p|\eta\rangle} \left[\frac{\partial \langle c_p|\eta\rangle}{\partial \eta} + \sum_{\alpha=1}^{N_s} \left(\langle c_{p,\alpha}|\eta\rangle \frac{\partial Q_\alpha}{\partial \eta} \right) \right] \frac{\partial Q_T}{\partial \eta} \right\} \tag{A.44}$$
$$-\frac{\langle\dot{\omega}_h|\eta\rangle}{\langle\rho|\eta\rangle\langle c_p|\eta\rangle} + \frac{1}{\langle\rho|\eta\rangle\langle c_p|\eta\rangle} \left\langle \frac{\partial p}{\partial t} \middle| \eta \right\rangle + \frac{\langle \dot{q}_{rad}|\,\eta\rangle}{\langle\rho|\eta\rangle\langle c_p|\eta\rangle},$$

where

$$\langle\dot{\omega}_h|\eta\rangle = \sum_{\alpha=1}^{N_s} \langle h_\alpha|\eta\rangle\langle\dot{\omega}_\alpha|\eta\rangle, \tag{A.45}$$

Bibliography

[1] A. Agarwal and D. N. Assanis. Multi-dimensional modeling of natural gas ignition under compression ignition conditions using detailed chemistry. *SAE*, Technical Paper No. 980136, 1998.

[2] ANSYS, Inc. ANSYS CFX 10.0, `http://www.ansys.com/products/cfx.asp`, 2006.

[3] ANSYS, Inc. ANSYS ICEM CFD, `http://www.ansys.com/products/icemcfd.asp`, 2006.

[4] M. Baum, T.J. Poinsot, D.C. Haworth, and N. Darabiha. Direct numerical simulation of $H_2/O_2/N_2$ flames with complex chemistry in two-dimensional turbulent flows. *J. Fluid Mech.*, 281:1–32, 1994.

[5] H. Bi and A.K. Agrawal. Study of autoignition of natural gas in diesel environments using computational fluid dynamics with detailed chemical kinetics. *Combust. Flame*, 113(3):289–302, 1998.

[6] R.W. Bilger. The structure of diffusion flames. *Combust. Sci. Technol.*, 13(1-6):155–170, 1976.

[7] R.W. Bilger. The structure of turbulent nonpremixed flames. *Proc. Combust. Inst.*, 22:475–488, 1988.

[8] R.W. Bilger. Conditional moment closure for turbulent reacting flow. *Phys. Fluids A*, 5(2):436–444, 1993.

[9] R.W. Bilger. Conditional moment closure modelling and advanced laser measurements. In T. Takeno, editor, *Turbulence and Molecular Processes in Combustion*, pages 267–285. Elsevier, Amsterdam, 1993.

[10] R.W. Bilger. Future progress in turbulent combustion research. *Prog. Energy Combust.*, 26(4-6):367–380, 2000.

[11] R. Borghi. Turbulent combustion modelling. *Prog. Energy Combust. Sci.*, 14(4):245–292, 1988.

[12] K.N.C. Bray and N. Peters. Laminar flamelets in turbulent flames. In P.a. Libby and F.A. Williams, editors, *Turbulent reacting flows*, pages 63,113. Academic Press, London, U.K., 1994.

[13] G. Brethouwer and F.T.M. Nieuwstadt. Dns of mixing and reaction of two species in a turbulent channel flow: a validation of the conditional moment closure. *Flow. Turbul. Combust.*, 66(3):209–239, 2001.

[14] R.S. Brokaw. Ignition kinetics of the carbon monoxide-oxygen reaction. *Proc. Combust. Inst.*, 11:10631073, 1967.

[15] W. K. Bushe and H. Steiner. Conditional moment closure for large eddy simulation of nonpremixed turbulent reacting flows. *Phys. Fluids*, 11(7):1896–1906, 1999.

[16] W. K. Bushe and H. Steiner. Laminar flamelet decomposition for conditional source-term estimation. *Phys. Fluids*, 15(6):1564–1575, 2003.

[17] C.M. Cha, G. Kosály, and H. Pitsch. Modeling extinction and reignition in turbulent nonpremixed combustion using a doubly-conditional moment closure approach. *Phys. Fluids*, 13(12):3824–3834, 2001.

[18] P. J. Colucci, F. A. Jaberi, , and P. Givi. Filtered density function for large eddy simulation of turbulent reacting flows. *Phys. Fluids*, 10(2):499–515, 1998.

[19] A.W. Cook and J.J. Riley. A subgrid model for equilibrium chemistry in turbulent flows. *Phys. Fluids*, 6(8):2868–2870, 1994.

[20] C.B. Devaud. *Conditional moment closure applied to lifted and attached turbulent jet flames*. PhD thesis, University of Cambridge, Cambridge, UK, 1999.

[21] C.B. Devaud. A second-order conditional moment closure model for the simulation of a lifted turbulent flame. *ANZIAM*, 45:419–434, 2004.

[22] C.B. Devaud, R.W. Bilger, and T. Liu. A new method of modeling the conditional scalar dissipation rate. *Phys. Fluids*, 16(6):2004–2011, 2004.

[23] C.B. Devaud and K.N.C. Bray. Assessment of the applicability of conditional moment closure to a lifted turbulent flame: first order model. *Combust. Flame*, 132(1):102–114, 2003.

[24] C. Dopazo. Recent development in PDF methods. In P.A. Libby and F.A. Williams, editors, *Turbulent reacting flows*, pages 375–474. Academic Press, London, U.K., 1994.

[25] A. El Sayed and C.B. Devaud. Numerical investigation of ignition delay in methane-air mixtures using conditional moment closure. In *the proceedings of the 21st International Colloquium on the Dynamics of Explosions and Reactive Systems (ICDERS)*, Poitiers, France, July 23-27, 2007.

[26] A. El Sayed and C.B. Devaud. Prediction of ignition delay using Conditional Moment Closure (CMC). In *the proceedings of the 30th Combustion Institute/Canadian Section (CICS) Spring Technical Meeting*, Banff, AB, Canada, May 13-16, 2007.

[27] V. Eswaran and S.B. Pope. Direct numerical simulation of the turbulent mixing of a passive scalar. *Phys. Fluids*, 31(3):506–520, 1988.

[28] A. Favre. Statistical equations of turbulent cases. In *Problems of hydrodynamics and continuum mechanics*, pages 231–266. SIAM, Philadelphia, PA, U.S.A., 1969.

[29] J.H. Ferziger and M. Perić. *Computational methods for fluid dynamics*. springer, Berlin, Germany, third edition, 2002.

[30] R.O. Fox. *Computational models for turbulent reactive flows.* Cambridge University Press, Cambridge, U.K., first edition, 2003.

[31] M. Frenklach and D.E. Bornside. Shock-initiated ignition in methane-propane mixtures. *Combust. Flame*, 56(1):1–27, 1984.

[32] M. Frenklach, H. Wang, M. Goldenberg, G.P. Smith, D.M. Golden, C.T. Bowman, R.K. Hanson, W.C. Gardiner, and V. Lissianski. GRI-Mech—An Optimized Detailed Chemical Reaction Mechanism for Methane Combustion. Technical Report Report No. GRI-95/0058, Gas Research Institute, November 1995.

[33] M. Frenklach, H. Wang, C.-L. Yu, M. Goldenberg, C.T. Bowman, R.K. Hanson, D.F. Davidson, E.J. Chang, G.P. Smith, D.M. Golden, W.C. Gardiner, and V. Lissianski. http://www.me.berkeley.edu/gri_mech/, 1995.

[34] A. Frisque, J. Schnakenberg, J. Huang, and W. K. Bushe. Stochastic simulation of variations in the autoignition delay time of premixed methane and air. *Combust. Theory model.*, 10(2):241 – 256, 2006.

[35] P. Gaillard. Multidimensional numerical study of the mixing of an unsteady gaseous fuel jet with air in free and confined situations. *SAE*, Technical Paper No. 840225, 1984.

[36] F. Gao. An analytical solution for the scalar probability density function in homogeneous turbulence. *Phys. Fluids A*, 3(4):511–513, 1991.

[37] S.S. Girimaji. Assumed β-pdf model for turbulent mixing : validation and extension to multiple scalar mixing. *Combust. Sci. Technol*, 78(4-6):177–196, 1991.

[38] S.S. Girimaji. On the modeling of scalar diffusion in isotropic flows. *Phys. Fluids A*, 4(11):2529–2537, 1992.

[39] P. Givi, C.K. Madnia, C.J. Steinberger, and S.H. Frankel. Large eddy simulations and direct numerical simulations of high speed turbulent reacting flows. Technical report, Nasa Langley Research Center, April 1991.

[40] I. Glassman. *Combustion*. Academic Press, San Diego, California, USA, third edition, 1996.

[41] GNU Project. GNU Scientific Library (GSL) reference manual, `http://www.gnu.org/software/gsl/manual/gsl-ref.html`, 2007.

[42] R. Grout, W.K. Bushe, and C. Blair. Predicting the ignition delay of turbulent methane jet using conditional source-term estimation. *Combust. Theory model.*, 2007. (Submitted).

[43] H. Guo, G.J. Smallwood, F. Liu, Y. Ju, and O.L. Gulder. The effect of hydrogen addition on flammability limit and no_x emission in lean counterflow ch_4/air premixed flames. *Proc. Combust. Inst.*, 30:303–311, 2004.

[44] P.G. Hill and P. Ouellette. Transient turbulent gaseous fuel jets for diesel engine. *J. Fluids Eng.*, 121(1):93–101, 1999.

[45] A.C. Hindmarsh. ODEPACK, a systemized collection of ODE solvers. In R.S. Stepleman et al., editor, *Scientific Computing*, pages 55–64. North Holland, Amsterdam, 1983.

[46] J.O. Hinze. *Turbulence*. McGraw-Hill, New York, first edition, 1959.

[47] J. Huang. *Natural gas combustion under engine-relevent conditions*. PhD thesis, University of British Columbia, BC, Canada, 2006.

[48] J. Huang and W.K. Bushe. Simulation of an igniting methane jet using conditional source-term estimation with a trajectory generated low-dimensional manifold. *Combust. Theory model.*, 2007. (In press).

[49] J. Huang, P.G. Hill, W.K. Bushe, and S.R. Munshi. Shock-tube study of methane ignition under engine-relevant conditions: experiments and modeling. *Combust. Flame*, 136(1-2):25–42, 2004.

[50] H.G. Im, J.H. Chen, , and C.K. Law. Ignition of hydrogen-air mixing layer in turbulent flows. *Proc. Combust. Inst.*, 27:1047–1056, 1998.

[51] W.P. Jones and B.E. Launder. The prediction of laminarisation with a two equation turbulence model. *Int. J. Heat Mass Transfer*, 15(2):301–314, 1972.

[52] R.J. Kee, F.M. Rupley, and J.A. Miller. Chemkin-II: A FORTRAN chemical kinetics package for the analysis of gas-phase chemical kinetics. Technical Report SAND89-9009B, Sandia National Laboratories, 1989.

[53] A.R. Kerstein. A linear eddy model of turbulent scalar transport and mixing. *Combust. Sci. Technol.*, 60(4-6):391–421, 1988.

[54] A.R. Kerstein. Linear eddy modelling turbulent transport. part 4. structure of diffusion flames. *Combust. Sci. Technol.*, 81(1-3):75–96, 1992.

[55] A.R. Kerstein. Linear eddy modelling turbulent transport. part 7. finite rate chemistry and multi-stream chemistry. *J. Fluid Mech.*, 240:289–313, 1992.

[56] S.H. Kim, K.Y. Huh, and R.W. Bilger. Second-order conditional moment closure modeling of local extinction and reignition in turbulent non-premixed hydrocarbon flames. *Proc. Combust. Inst.*, 29:21312137, 2002.

[57] S.H. Kim, K.Y. Huh, and R.A. Fraser. Modeling autoignition of a turbulent methane jet by the Conditional Moment Closure model. *Proc. Combust. Inst.*, 28:185–191, 2000.

[58] S.H. Kim, K.Y. Huh, and R.A. Fraser. Numerical prediction of the autoignition delay in a diesel-like environment by the Conditional Moment Closure model. *SAE*, Technical Paper No. 2000-01-0200, 2000.

[59] S.H. Kim, K.Y. Huh, and L. Tao. Application of the elliptic conditional moment closure model to a two-dimensional nonpremixed methanol bluff-body flame. *Combust. Flame*, 120(1-2):75–90, 2000.

[60] W.T. Kim and k.Y. Huh. Numerical simulation of spray autoignition by the first order Conditional Moment Closure model. *Proc. Combust. Inst.*, 29:569576, 2002.

[61] A.Yu. Klimenko. Multicomponent diffusion of various admixtures in turbulent flow. *Fluid Dyn.*, 25(3):327–334, 1990.

[62] A.Yu. Klimenko. Note on the conditional moment closure in turbulent shear flows. *Phys. Fluids*, 7(2):446–448, 1995.

[63] A.Yu. Klimenko and R.W. Bilger. Conditional moment closure for turbulent combustion. *Prog. Energy Combust. Sci.*, 25(6):595–687, 1999.

[64] A.N. Kolmogorov. The equations of turbulent motion in an incompressible flow. *Izvestia. Acad. Sci., USSR; Phys.*, 6:56–58, 1942.

[65] A. Kronenburg and A.E. Papoutsakis. Conditional moment closure modeling of extinction and re-ignition in turbulent non-premixed flames. *Proc. Combust. Inst.*, 30:759766, 2005.

[66] K.K. Kuo. *Principles of Combustion*. John Wiley and Sons, Inc., Hoboken, New Jersey, USA, second edition, 2005.

[67] V.R. Kuznetsov. Effect of turbulence on the formation of large superequilibrium concentration of atoms and free radicals in diffusion flames. *Mehan. Zhidkosti Gasa*, 6:3–9, 1982.

[68] V.R. Kuznetsov and V.A. Sabel'nikov. *Turbulence and combustion*. Hemisphere Publishing, New York, english edition, 1990.

[69] B.E. Launder and D.B. Spalding. *Lectures in mathematical models of turbulence*. Academic Press, London, U.K., 1972.

[70] P.D. Lax. Applied mathematics and computing. *Proceedings of Symposia in Applied Mathematics*, 20:57–66, 1974.

[71] J.D. Li and R.W. Bilger. Measurement and prediction of the conditional variance in a turbulent reactive-scalar mixing layer. *Phys. Fluids A*, 5(12):3255–3264, 1993.

[72] J.D. Li and R.W. Bilger. A simple theory of conditional mean velocity in turbulent scalar-mixing layer. *Phys. Fluids*, 6(2):605–610, 1994.

[73] A. Lifshitz, K. Scheller, A. Burcat, and G.B. Skinner. Shock-tube investigation of ignition in methane-oxygen-argon mixtures. *Combust. Flame*, 16(3):311–321, 1971.

[74] U. Maas and S.B. Pope. Simplifying chemical kinetics: Intrinsic low-dimensional manifolds in composition space. *Combust. Flame*, 88(3-4):239–264, 1992.

[75] B.F. Magnussen and B.H. Hjertager. On mathematical modeling of turbulent combustion with special emphasis on soot formation and combustion. *Proc. Combust. Inst.*, 16:719–729, 1976.

[76] C.N. Markides, G. De Paola, and E. Mastorakos. Measurements and simulations of mixing and autoignition of an n-heptane plume in a turbulent flow of heated air. *Exp. Therm. Fluid Sci.*, 31(5):393–401, 2007.

[77] A.R. Masri, R.W. Dibble, and R.S. Barlow. The structure of turbulent nonpremixed flames of methanol over a range of mixing rates. *Combust. Flame*, 89(2):167–185, 1992.

[78] E. Mastorakos, T.A. Baritaud, and T.J. Poinsot. Numerical simulations of autoignition in turbulent mixing flows. *Combust. Flame*, 109(1-2):198–223, 1997.

[79] E. Mastorakos and R.W. Bilger. Second-order conditional moment closure for the autoignition of turbulent flows. *Phys. Fluids*, 10(6):1246–1248, 1998.

[80] E. Mastorakos, A. Pires da Cruz, T.A. Baritaud, and T.J. Poinsot. A model for the effects of mixing on the autoignition of turbulent flows. *Combust. Sci. Technol.*, 125(1-6):243–282, 1997.

[81] W.E. Mell, V. Nilsen, G. Kosály, and J.J. Riley. Investigation of closure models for nonpremixed turbulent reacting flows. *Phys. Fluids*, 6(3):1331–1356, 1994.

[82] P. Moin. *Fundamentals of engineering numerical analysis*. Cambridge University Press, Cambridge, UK, first edition, 2001.

[83] J.D. Naber, D.L. Siebers, J.A. Caton, C.K. Westbrook, and S.S. Di Julio. Natural gas autoignition under diesel conditions: experiments and chemical kinetic modeling. *SAE*, Technical Paper No. 942034, 1994.

[84] E. O'Brian and T.L. Jiang. The conditional dissipation rate of an initially binary scalar in homogeneous turbulence. *Phys. Fluids A*, 3(12):3121–3123, 1991.

[85] E.S. Oran and J.P. Boris. *Numerical simulation of reactive flow*. Elsevier Science Publishing Co, Inc., 52 Vanderbilt Avenue, New York, New York 10017, first edition, 1987.

[86] P. Ouellette and P.G. Hill. Turbulent transient gas injections. *J. Fluids eng.*, 122(4):743–752, 2000.

[87] N. Peters. Laminar diffusion flamelet models in non-premixed turbulent combustion. *Prog. energy Combust. Sci*, 10(3):319–339, 1984.

[88] N. Peters. Laminar flamelet concepts in turbulent combustion. *Proc. Combust. Inst.*, 21:1231–1250, 1986.

[89] N. Peters. *Turbulent combustion*. Cambridge University Press, Cambridge, UK, first edition, 2000.

[90] N. Peters. Local quenching of diffusion flamelets and non-premixed turbulent combustion. In *Proc. of WSSCI*, Irvine, CA, U.S.A., Paper WSS 80-4, 1980.

[91] E.L. Petersen, D.F. Davidson, and R.K. Hanson. Kinetics modeling of shock-induced ignition in low-dilution ch4/o2 mixtures at high pressures and intermediate temperatures. *Combust. Flame*, 117(1-2):272–290, 1999.

[92] R. Piessens and E. de Doncker-Kapenga andC.W. Ueberhuber. *Quadpack: A Subroutine Package for Automatic Integration*. Springer (Springer Series in Computational Mathematics), Berlin, 1983.

[93] T. Poinsot and D. Veynante. *Theoretical and numerical combustion*. R.T. Edwards, Inc, USA, second edition, 2005.

[94] S. B. Pope and U. Maas. Simplifying chemical kinetics: trajectory generated low-dimensional manifolds. Technical Report FDA 93-11, Cornell University Report, 1993.

[95] S.B. Pope. An explanation of the turbulent round-jet/plane-jet anomaly. *AIAA*, 16(3):279–281, 1978.

[96] S.B. Pope. PDF methods for turbulent reactive flows. *Prog. Energy Combust. Sci.*, 11(2):119–192, 1985.

[97] S.B. Pope. Mapping closures for turbulent mixing and reaction. *Theoretical Comput. Fluid Dyn.*, 2(5-6):255–270, 1991.

[98] S.B. Pope. Lagrangian PDF methods for turbulent flows. *Annu. Rev. Fluid Mech.*, 26:23–63, 1994.

[99] S.B. Pope. *Turbulent Flows*. Cambridge University Press, Cambridge, U.K., first edition, 2000.

[100] W.H. Press and B.P. Flannery S.A. Teukolsky, W.T. Vetterling. *Numerical recipes in Fortran 77, the art of scientific computing*. Cambridge University Press, Cambridge, UK, second edition, 1992.

[101] K. Radhakrishnan and A.C. Hindmarsh. Description and use of LSODE, the Livermore Solver for Ordinary Differential Equations. Technical Report UCRL-ID-113855, Lawrence Livermore National Laboratory, 1993.

[102] R.A.Frazer, D.L. Siebers, and C.F. Edwards. Autoignition of methane and natural gas in a simulated diesel environment. *SAE*, 1991.

[103] F.P. Ricou and D.B. Spalding. Measurement of entrainment by asymmetrical turbulent jets. *J. Fluid Mech.*, 11(1):21–32, 1961.

[104] M.R. Roomina and R.W. Bilger. Conditional moment closure modelling of turbulent methanol jet flames. *Combust. Theory Modelling*, 3(4):689708, 1999.

[105] M.R. Roomina and R.W. Bilger. Conditional moment closure (CMC) predictions of a turbulent methane-air jet flame. *Combust. Flame*, 125(3):1176–1195, 2001.

[106] P.G. Saffman. A model for inhomogeneous turbulent flow. *Proc. Roy. Soc. Lond.*, 317(1530):417–433, 1970.

[107] G.P. Smith, D.M. Golden, M. Frenklach, N.W. Moriarty, B. Eiteneer, M. Goldenberg, C.T. Bowman, R.K. Hanson, S. Song, W.C. Gardiner, Jr., V.V. Lissianski, , and Z. Qin. http://www.me.berkeley.edu/gri_mech/, 1999.

[108] D.B. Spalding. Mixing and chemical reaction is steady confined turbulent flames. *Proc. Combust. Inst.*, 13:649–657, 1971.

[109] C.G. Speziale, R. Abid, and E.C. Anderson. Critical evaluation of two-equation models for near-wall turbulence. *AIAA J.*, 30(2):324–331, 1992.

[110] S. Sreedhara and K.N. Lakshmisha. Direct numerical simulation of autoignition in a non-premixed, turbulent medium. *Proc. Combust. Inst.*, 28:2534, 2000.

[111] S.H. Stårner, R.W. Bilger, K.M. Lyons, J.H. Frank, and M.B. Long. Conserved scalar measurements in turbulent diffusion flames by a raman and rayleigh ribbon imaging method. *Combust. Flame*, 99(2):347–354, 1994.

[112] G.D. Sullivan, J. Huang, W.K. Bushe, and S.N. Rogak. Auto-ignition of transient turbulent gaseous fuel jets at high pressure. *SAE*, Technical Paper No. 2005-01-0917, 2005.

[113] G.D. Sullivan, J. Huang, T.X. Wang, W.K. Bushe, and S.N. Rogak. Emissions variability in gas fuel direct injection compression ignition combustion. *SAE*, Technical Paper No. 2005-01-0917, 2005.

[114] N. Swaminathan and R.W. Bilger. Analyses of conditional moment closure for turbulent premixed flames. *Combust. Theory model.*, 5(2):241–260, 2004.

[115] N. Swaminathan and B.B. Dally. Cross stream dependence of conditional averages in elliptic region of flows behind a bluff-body. *Phys. Fluids*, 9(10):2424–2426, 1998.

[116] N. Swaminathan and S. Mahalingam. Assessment of conditional moment closure for single and multistep chemistry. *Combust. Sci. Technol.*, 112(1):301–326, 1996.

[117] C.F. Taylor. *The internal-combustion engine in theory and practice. Volume II: combustion, fuels, materials, design.* MIT Press, Cambridge, Massachusetts, 1985.

[118] A. Trouvé and T.J. Poinsot. The evolution equation for the flame surface density in turbulent premixed combustion. *J. Fluid Mech.*, 278:1–31, 1994.

[119] W. Tsang and R.F. Hampson. Chemical kinetic data base for combustion chemistry. *J. Phys. Chem. Ref.*, 15(3):1087–1222, 1986.

[120] J.S. Turner. The 'starting plume' in neutral surrounding. *J. Fluid Mech.*, 13(3):356–368, 1962.

[121] D. Veynante and L. Vervisch. Turbulent combustion modeling. *Progress in Energy and Combustion Science*, 28(3):193–266, 2002.

[122] F.A. Williams. Recent advances in theoretical descriptions of turbulent diffusion flames. In S.N.B. Murthy, editor, *Turbulent mixing in nonreactive and reactive flows*, pages 189–208. Plenum Press, New York, U.S.A., 1975.

[123] Y.M. Wright, G. De Paola, K. Boulouchos, and E. Mastorakos. Simulations of spray autoignition and flame establishment with two-dimensional CMC. *Combust. Flame*, 143(4):402–419, 2005.